INNOVATIVE TESSELLATION ALGORITHM FOR GENERATING MORE UNIFORM TEMPERATURE DISTRIBUTION IN THE POWDER-BED FUSION PROCESS

A Thesis

Submitted to the Faculty

of

Purdue University

by

Ehsan Maleki Pour

In Partial Fulfillment of the

Requirements for the Degree

of

Master of Science in Mechanical Engineering

December 2018

Purdue University

Indianapolis, Indiana

THE PURDUE UNIVERSITY GRADUATE SCHOOL
STATEMENT OF COMMITTEE APPROVAL

Dr. Hazim El-Mounayri, Chair

Department of Mechanical and Energy Engineering

Dr. Andres Tovar

Department of Mechanical and Energy Engineering

Dr. Jing Zhang

Department of Mechanical and Energy Engineering

Dr. Mohammad Al Hasan

Department of Computer and Information Science

Approved by:

Dr. Sohel Anwar

Chair of the Graduate Program

This thesis, first and foremost, is dedicated to my Lord, Allah, who is the truth and source of each and every thing that I have. Second, it is dedicated to His Light(s). Third, to my parents, Bahman and Mehri to express my great debt of gratitude. I pray to always bring them honor and health.

ACKNOWLEDGMENTS

I would like to express my most sincere gratitude to my adviser, Dr. Hazim El-Mounayri, for his invaluable guidance and financial support these years. Working under his direction in the Collaborative Additive Manufacturing Research Initiative (CAMRI) center has helped me to grow professionally and personally. He has not been only my supervisor but my role model in personal life and I have received invaluable lessons for my life from him, especially after 7 p.m.! I also want to thank the members of my committee, Dr. Andres Tovar who was the main person who encouraged me to come to USA. My journey started and ended here with his class. Furthermore, Dr. Jing Zhang and Dr. Mohammad Al Hasan for their invaluable suggestions to improve this research project.

I gratefully acknowledge the financial support that I received from our Department. Without their support, I could have never had this life-changing experience.

Finally, I want to thank my friends and laboratory fellows Samuel Attoye, Ebrahim Feyz, Sajjad Raeisi, Suchana Jahan, Roozbeh Gharakhloo, Maxim Kosmakov, Reza Farahani, Homero Guerra, Kai Liu, Joseph Derrick, Mike Golub, Dinesh Vemula, and Shaunak Chandwadkar for their help and support during this project and make a happier atmosphere in our lab! My sincere thanks also to Linda Wright, Deborah Bennet, and Jerry Mooney at Purdue school of engineering and technology. A special thanks to Allison Hedrick, Asma Salek, and Roozbeh Gharakhloo for their honest friendship to continue growing in my personal life.

TABLE OF CONTENTS

Page

LIST OF TABLES

LIST OF FIGURES

Figure Page

Figure Page

ABBREVIATIONS

AM:	Additive Manufacturing
ANN:	Artificial Neural Networking
ASCII:	American Standard Code for Information Interchange
BP:	Back-propagation
BPNN:	Back-propagation Neural Networking
CAMRI:	Collaborative Additive Manufacturing Research Initiative
CCD:	Charge Coupled Device
CMOS:	Complementary Metal-Oxide Semiconductor
CPNN:	Counter Propagation Neural Network
DMLS:	Direct Metal Laser Sintering
FDM:	Fused Deposition Modeling
FE:	Finite Element
FEA:	Finite Element Analysis
GUI:	Graphical User Interface
HAZ:	Heat Affected Zone
HIP:	Hot Isostatic Pressing
IR:	Infrared
MC:	Marangoni Convection
PM:	Powder Metallurgy
RBN:	Radial Basis Network
RNN:	Recurrent Neural Network
SLM:	Selective Laser Melting
SLS:	Selective Laser Sintering
SS:	Stainless Steel

ABSTRACT

Maleki Pour, Ehsan. M.S.M.E., Purdue University, December 2018. Innovative Tessellation Algorithm for Generating More Uniform Temperature Distribution in the Powder-bed Fusion Process. Major Professor: Hazim El-Mounayri.

Powder Bed Fusion Additive Manufacturing enables the fabrication of metal parts with complex geometry and elaborates internal features, the simplification of the assembly process, and the reduction of development time. However, the lack of consistent quality hinders its tremendous potential for widespread application in industry. This limits its ability as a viable manufacturing process particularly in the aerospace and medical industries where high quality and repeatability are critical. A variety of defects, which may be initiated during the powder-bed fusion additive manufacturing process, compromise the repeatability, precision, and resulting mechanical properties of the final part. The literature review shows that a non-uniform temperature distribution throughout fabricated layers is a significant source of the majority of thermal defects. Therefore, the work introduces an online thermography methodology to study temperature distribution, thermal evolution, and thermal specifications of the fabricated layers in powder-bed fusion process or any other thermal inherent AM process. This methodology utilizes infrared technique and segmentation image processing to extract the required data about temperature distribution and HAZs of the layer under fabrication. We conducted some primary experiments in the FDM process to leverage the thermography technique and achieve a certain insight to be able to propose a technique to generate a more uniform temperature distribution. These experiments lead to proposing an innovative chessboard scanning strategy called tessellation algorithm, which can generate more uniform temperature distribution and diminish the layer warpage consequently especially throughout the layers with either

geometry that is more complex or poses relatively longer dimensions. In the next step, this work develops a new technique in ABAQUS to verify the proposed scanning strategy. This technique simulates temperature distribution throughout a layer printed by chessboard printing patterns in powder-bed fusion process in a fraction of the time taken by current methods in the literature. This technique compares the temperature distribution throughout a designed layer printed by three presented chessboard-scanning patterns, namely, rastering pattern, helical pattern, and tessellation pattern. The results confirm that the tessellation pattern generates more uniform temperature distribution compared with the other two patterns. Further research is in progress to leverage the thermography methodology to verify the simulation technique. It is also pursuing a hybrid closed-loop online monitoring (OM) and control methodology, which bases on the introduced tessellation algorithm and online thermography in this work and Artificial Neural Networking (ANN) to generate the most possible uniform temperature distribution within a safe temperature range layer-by-layer.

1. INTRODUCTION

1.1 Background

AM started as a stereolithography method [1] focusing on prototyping aimed at decreasing the development time of production evaluation [2]. However, metal-based AM [1-7] has made possible the production of end-use parts. The powder-bed fusion process is a hands-off process in which 3D printer fabricates the designed part directly from an STL file layer by layer. This process fabricates a part layer by layer with the thickness between 20 µm to 100 µm by applying a laser beam on a layer of powder to sintered selected areas [2, 6, 8]. This process makes possible to fabricate complex geometry and elaborate internal features, however, it is not free of defects. The defects generated during the process reduce the surface quality, repeatability, and microstructure uniformity and weaken mechanical properties, which are critical in some stringent industries such as biomedical or aerospace industries [9-11]. Quality control of AM is currently lacking, leaving the process subject to high scrap rate and significant rework. If not addressed, this will continue to limit the great potential of AM as a transformative technology with numerous advantages and benefits. Due to a large number of process parameters as well as a variety of defects with complex undetermined relationships with the contributing parameters, developing an effective, efficient, and robust online process monitoring and control remains a challenge. The complexity of the nature of process hinders scholars to establish a precise mathematical model to employ for adjusting process parameters and as a result, limits the role of predictive modeling as an immediate alternative to controlling the process. Scholars need to address two fundamental questions to overcome these barriers. (1) What is the dynamic behavior of significant process parameters in the powder-bed fusion process, and how they relate to the inception of anomalies? (What are the most important defects and controlling parameters?) Moreover, (2) what is the cause and effect relationship between the process parameters/variables and defects/part quality, and how we can vary those parameters to achieve the desired quality or optimize the process?

This research works toward creating a thermal process monitoring and deep machine learning as the ultimate approach to handle the complexity and uncertainty of the powder-bed fusion process and allow for real-time process parameters adjustment. For the sake of achieving this goal, the first step is to classify the defects under some significant process signatures or process specifications to facilitate monitoring operation. Furthermore, recognizing the essential controllable parameters makes possible to manipulate the process parameters in an effective way with a limited number of controllable parameters. Thermal aspects of powder-bed fusion process significantly affect the ultimate part quality of fabricated parts, scrap rate, and post-processing operations. This research work develops an innovative monitoring strategy to study thermal evolution during the fabrication process and detect HAZ areas in macro scale layer by layer, instead of common monitoring strategies that track melt pool specifications in microscale. Detection of the HAZs is necessary to modify the scan pattern layer by layer to generate more uniform temperature distribution and control the energy density exerted to each zone. Moreover, the data acquired from online monitoring (OM) will provide insights for controlling the process parameters. Literature shows a uniform temperature distribution is an effective proxy for making a homogenous microstructure and mitigating some prevalent thermal abnormalities such as distortion, shrinkage, etc. [12] Controlling the energy density and temperature range also hinders some major thermal defects such as balling phenomena, poor bonding between layers, etc.

The ultimate objective of the ongoing research is to develop a hybrid control strategy in order to first, modify the scan pattern in situ based on the acquired data from the monitoring system to minimize the thermal abnormalities. To achieve this objective, this work proposes an innovative scanning strategy called tessellation algorithm, which helps to generate more uniform temperature distribution in the layer under fabrication. This work develops a new simulation technique to evaluate the influence of the proposed scanning-pattern algorithm. Second, implement some error handling strategies to eliminate the generated defects. Future research needs to achieve the second goal. This research, if successful, would have a significant impact by enabling the wider adoption of this transformative technology in all thermal inherent AM process. The following schematic abstract (Fig. 1.1) shows different tasks to complete the hybrid control methodology for the powder-bed fusion process. This work includes task number one, two, and a part of task number three (tessellation algorithm).

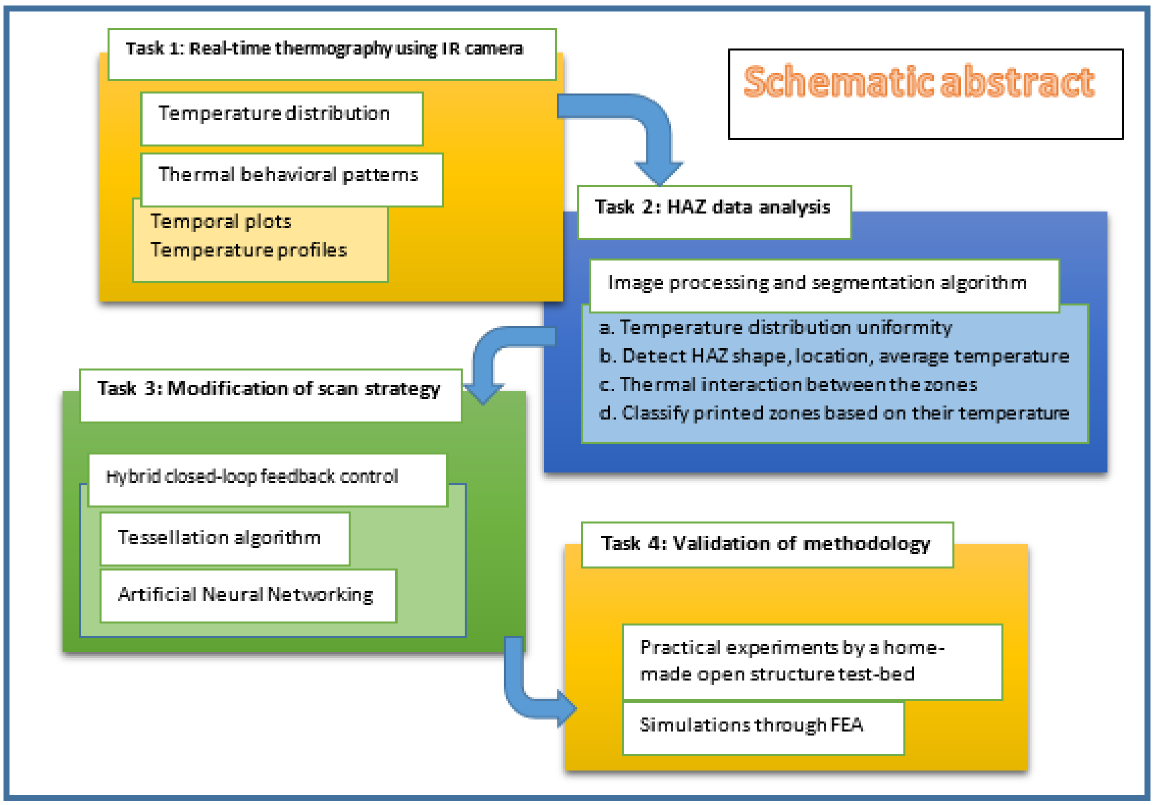

Figure 1.1. Schematic abstract shows the tasks, which needs to complete the hybrid control strategy

1.2 Motivation and problem statement

The Wohlers Report annually publishes a compendium of commercial activity relating to AM. Its latest issue reports that the 2016 AM services market have grown by 17.4% in worldwide revenues in 2016, to reach $6.063 billion AM industry [13]. While recent research has greatly improved the current AM machine tools from early versions, many of the same problems identified by early researchers in the 1980s persist. Thermal anomalies significantly affect the ultimate quality of the fabricated parts and cause a large portion of the generated defects during the sintering process [14]. Such product defects lead to considerable rework and scrap rates, and thus pose significant impediments for sustainability of AM. Controlling of thermal evolution can avoid the onset of these defects or minimize them. Recognition of the defects, their contributing parameters, and the causal linkage between the defects, contributing parameters, and the controllable process parameters can leverage to control the process smartly. This objective is achievable by the employment of online monitoring and in situ closed-loop control algorithm. Online monitoring and process control increases the robustness by checking the quality of the fabricated part in the earliest possible stage. This capability facilitates avoiding the anomalies or removing the generated defects by the implementation of corrective actions during the process [15]. Controlling of temperature field throughout the layer under fabrication is an excellent proxy for the ultimate quality of the fabricated part, since it has a direct impact on the resulting microstructure, density, and mechanical properties [12]. Myriad efforts tried to develop thermal monitoring systems to understand the process better rather than detection of process anomalies and control the machine operation real-time. To date, all predictions in metal-based AM base on FE physics-based simulation that poses a high computational burden to solve in an efficient time or some imperfect mathematical models. This research work pursues an efficient data-driven online monitoring and control system, which is capable of processing large data streams real-time and change significant process parameters subsequently.

1.3 Research objectives (accomplishments)

Lack of practical real-time closed-loop control strategies and limited proposed printing strategies hamper many efforts conducted by scholars/industry to avoid, remove, or minimize the fabrication anomalies in the powder-bed fusion process. Literature review (Chapter 2) shows that generating a homogeneous temperature field within a specific range and controlling the exerted energy density during the fabrication process, will avoid or significantly reduce the fabrication thermal anomalies [16]. This project accomplishes the following objectives to overcome the aforementioned challenges.

- Understating the thermal behavior of the powder-bed fusion process by the study of process thermal defects, their contributing parameters, and the causal effects between the contributing parameters and the controllable process parameters.

- Introducing a macro-scale thermal-based real-time methodology to monitor the entire bed area of the fabrication process, collecting and analyzing data real-time, and is capable to implement in current SLS printing machine.

- Proposing a novel chessboard scanning-pattern called tessellation scanning strategy (or tessellation algorithm) to generate more uniform temperature distribution in part either with geometry that is more complex or with relatively longer dimensions.

- Developing a new simulation technique to study the effect of different process parameters and printing patterns on the temperature distribution of the layer under fabrication.

The ultimate goal of this project is to develop a practical hybrid closed-loop feedback control algorithm as the future phase of the project, which can be implemented rapidly in the current 3D printer machines. This control algorithm will diminish/remove the thermal defects and elevate the ultimate quality of fabricated parts, namely, microstructure, mechanical properties, and surface quality. This phase includes the following items.

- Employment of the monitoring methodology to validate the simulation technique.
- Employment of monitoring information to adjust the objective process parameters real-time.
- Quality certification of the fabricated part layer by layer.
- Combining offline algorithms such as the designed tessellation algorithm and real-time smart decision-making algorithms such as ANN to modify the process parameters.
- Modification of scan strategy real-time to generate the most possible uniform temperature distribution and remove thermal abnormalities, as the ultimate objective of the project.
- Validation of the control strategy with completing our open-source open-structure 3D printer.

1.4 Thesis outline

Chapter 1 presents the essential questions, different tasks, the current gaps in the literature, and finally the motivation and problem statement to accomplish the current and future research objectives of designing an online monitoring and hybrid closed-loop feedback control system in the powder-bed fusion process. In order to support the design and implementation of an effective monitoring and control strategies, chapter 2 first identifies, analyzes, and classifies the common defects and their contributing parameters reported in the literature as well as the relationship between the two. Next, it categorizes both defects and contributing parameters under an umbrella of manufacturing features for monitoring and control purposes. This chapter also presents an alternative approach to control the process indirectly by monitoring signatures instead of actual defects. Our study shows that thermal defects represent the main portion of the manufacturing abnormalities, which significantly reduces repeatability, precision, and ultimate mechanical and surface quality of fabricated parts. A great deal of literature proposes monitoring and control of temperature distribution as the best proxy to minimize or avoid the thermal abnormalities. Chapter 3 carries out some primary experiments and monitor them online with an introduced IR thermography to provide an insight into the effect of scanning strategy and geometry features on temperature distribution. The introduced monitoring methodology employs an image segmentation algorithm in MATLAB to detect the Heat Affected Zone (HAZ), reveals its specifications, and evaluates the thermal evolution of different inherent thermal AM processes layer by layer. These insights help to propose a novel chessboard scanning strategy called tessellation algorithm as the methodology to diminish the thermal defects/abnormalities by generating more uniform temperature distribution. Chapter 4 develops a new technique in ABAQUS to verify the proposed scanning strategy. This technique simulates temperature distribution throughout a layer printed by chessboard printing patterns in powder-bed fusion process in a fraction of the time taken by current methods in the literature. Moreover, this technique evaluates the temperature distribution in three different chessboard-scanning patterns, namely, rastering pattern, helical pattern, and tessellation pattern. The monitoring code in MATLAB also employs here to compare the resulting temperature distribution and HAZ specifications for different simulated scan patterns. Finally, chapter 5 presents the ongoing research on validation of the simulation technique by using the introduced monitoring methodology and explains the reminded works to complete hybrid closed-loop online monitoring and control methodology. This methodology aims to modify scan strategy real-time to generate the most uniform temperature distribution within a safe temperature range layer-by-layer by a combination of the tessellation algorithm, online thermography, and Artificial Neural Networking (ANN).

2. A LITERATURE REVIEW

2.1 Common defects and contributing parameters in powder-bed fusion AM process

2.1.1 Introduction

Despite enormous improvements in the SLS process, a variety of defects limits the process in terms of repeatability, precision and resulting mechanical properties. In this section, we describe all the important defects generated during the SLS process as well as their contributing parameters. In addition, we reveal a correlation between the two. These defects can be categorized into four general areas based on the way they affect the printed part. These areas are 1) Geometry and Dimension; 2) Surface Quality; 3) Microstructure; and 4) Mechanical Properties. Fig. 2.1 depicts the defects considered in each area. It should be noted that the type of generated defects in SLS does not depend on the type of materials; only the range of the parameters and the prevalence of defects vary from one material to the other. [17]

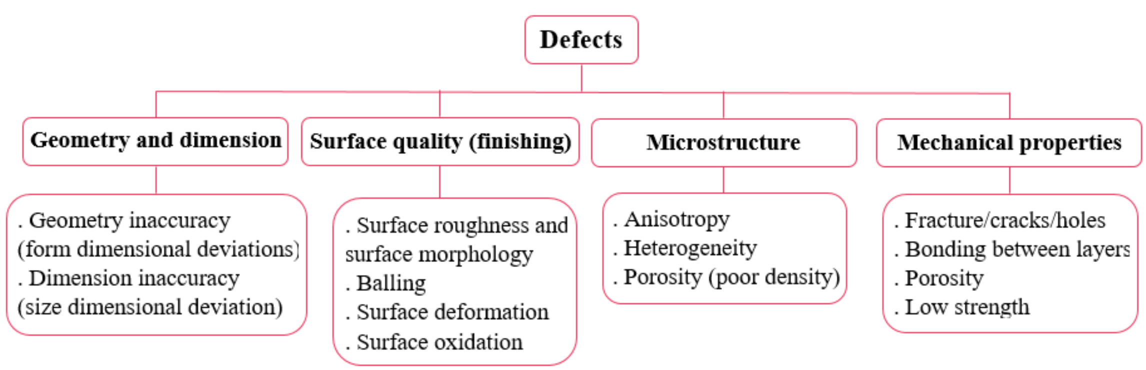

Figure 2.1. Common defects in SLS process

2.1.2 Defects related to geometry and dimensions

Geometric inaccuracy (form dimensional deviations)

Staircase effect and machine error parameters are two contributing parameters that lead to this defect. Regarding the staircase effect, the layer thickness is considered the main source because of the geometric approximation of a curved surface. This feature is introduced as a cusp height error. (Fig. 2.2). The thicker the layer, the larger the staircase effect [18-20].

There are two machine specifications (Machine error parameters) which lead to geometric inaccuracy: 1) Laser positioning error (i.e. a defective laser focus on the SLS/DMLS machines manufacturing platform); and 2) Platform movement error (i.e. a defective motion of manufacturing platform in the vertical direction) [19, 21]

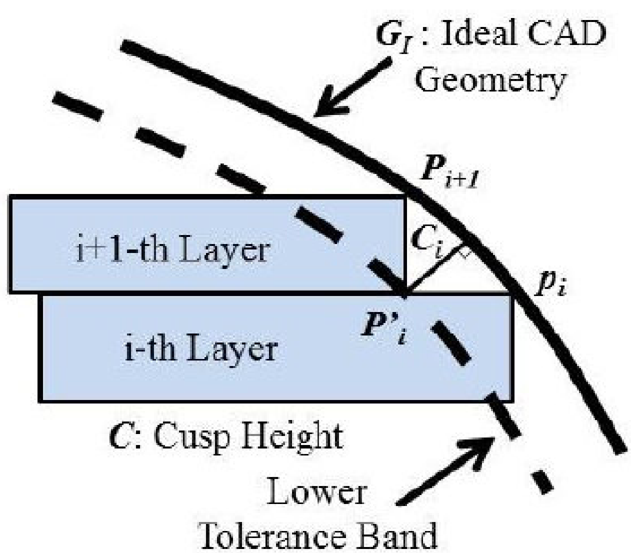

Figure 2.2. Cusp height and staircase effect [20]

Dimensional inaccuracy (size dimensional deviations)

Tap density, shrinkage, spot diameter or effective laser diameter, microstructural waviness, building direction and gas flow rate are the most important contributing parameters leading to dimensional inaccuracy.

Using a vertical vibration in a rotating roller to compress a new layer of powder for better density (Tap density) can lead to vertical displacement, and as a result dimensional inaccuracy, in previously melted layers [22]. There are two types of shrinkage in the SLS process: sintering shrinkage and thermal shrinkage [23]; Sintering shrinkage is mainly caused by densification while thermal shrinkage is due to cyclic heating [23]. Thermal shrinkage can be decreased by controlling process parameters, calibrating the building strategy, or applying a compensation technique. The most effective factors are as follows [23-25]:

- The higher the laser power, the larger is the thermal shrinkage.
- The higher the scan speed and scan spacing (hatch space), the lower is the thermal shrinkage; the hatch space is highly effective in DMLS whose effect is depicted in Fig. 2.3.
- The temperature variation leads to non-uniform shrinkage in a particular layer [26].
- Part weight, build chamber temperature, cooling rate, layer thickness and material can affect shrinkage in a way that shrinkage decreases with increasing layer thickness, part bed temperature, and interval time (the time between the building of two subsequent layers) [27-29].
- Liquid flow is dislodged by capillary and gravity forces when the mixture of two metal powders with significantly different melting points is used [30].

Shrinkage can take place either in the X-Y plane (In-plane shrinkage) or in the build direction (Z-direction). In-plane shrinkage (X and Y shrinkage) is much less

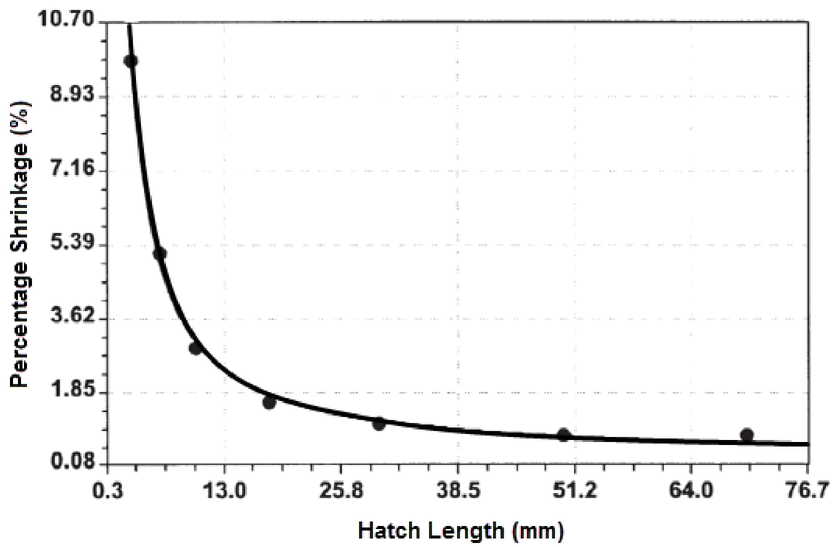

Figure 2.3. Hatch length vs. percentage of shrinkage in the DMLS process [25]

than the shrinkage in the build direction (Z-direction) due to z-growth phenomena; shrinkage decreases with the increase in nominal dimensions [23, 31]. The most significant process parameters that affect shrinkage are laser power and scan length along the X-direction, laser power and beam speed along Y-direction, and beam speed, hatch spacing and part bed temperature along the Z-direction [32]. Furthermore, changes in geometry alter the scan length affecting shrinkage in the X-direction; the speed compensation technique can compensate the shrinkage in which the laser scan speed is adjusted dynamically according to the scan length based on the shrinkage values at different speeds [33]. This technique is developed for the DMLS process in [24].

Spot diameter or effective laser diameter (the diameter of the sintered area) is usually bigger than the exerted laser beam diameter, which leads to a dimensional error. For correction, the laser beam should be shifted from the boundaries of the cross-section, which is referred to as beam offset [34, 35].

In SLS, sintering creates a wavelike solid layer (microstructural waviness) because of hatching distance and balling phenomena. The wavelength is equal to the hatching space and reduces the dimensional accuracy and the surface quality. (Fig. 2.4) [36].

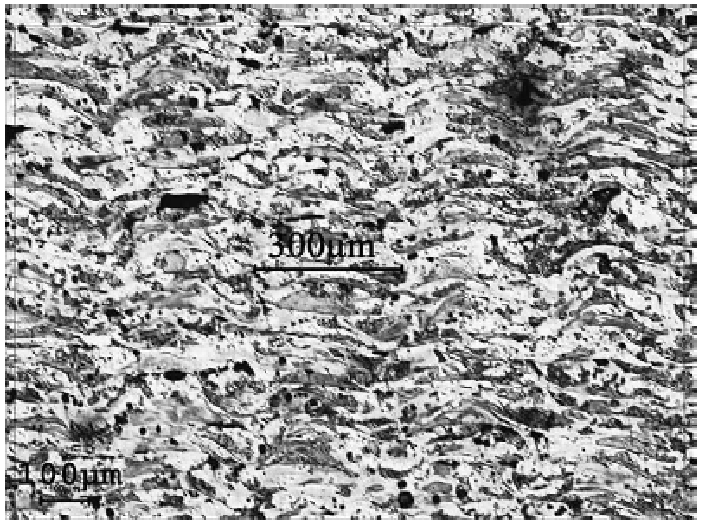

Figure 2.4. Side view shows a wavy layer, hatching width, and layer thickness [36]

The literature emphasizes the effect of building direction on geometric dimensions and tolerance. It shows that in DMLS, the dimensional error decreases along the width direction and increases along the thickness direction when the building direction is altered from 0° to 90° [37]. The unit sphere approach is introduced in reference [38] for finding the best build orientation.

Scholars emphasize the significant effect of gas flow rate on achieving and maintaining a high dimensional tolerance but there is no information yet about its effects [22].

2.1.3 Defects related to surface quality (finishing)

Surface roughness and morphology, balling, and surface deformation are the three main sources of surface defects.

Surface roughness and surface morphology

There are numerous contributing parameters which change the surface roughness and surface morphology of manufactured part including scan strategy and laser specifications such as scan speed, scan pattern and remelting, overlapping ratio and hatch space, spot size, energy density and laser pulse length. The other contributing parameters, which affect surface quality, are powder deposition, pits on the surface, fractures, cracks and holes, the quality of the substrate, staircase effect and surface orientation.

Scan strategy and laser specifications As Fig. 2.5 depicts, for low scan speed (lower than 15 mm/s) the average roughness decreases with increasing speed, for medium speed it fluctuates, and for high speed (more than 100 mm/s), it almost remains constant. A variable speed can also affect the created cross-section of the melt pool; for instance, scan speed between 1 mm/s to 4 mm/s creates rounded tracks, which leave a trench surrounding the track. Furthermore, decreasing scan speed can increase melt flow in the melt pool leading to an irregular surface [22, 39-43].

Different scan strategies (patterns), such as raster, spiral, staggered, and zigzag scanning, lead to different surface roughness. Furthermore, multiple time remelting in different directions or with a zigzag scan strategy improves the surface roughness. Applying remelting strategy to the last layer can improve the surface roughness up to about 90% [40, 44, 45].

The overlapping ratio defined as $k = (b - s)/b$ (Fig. 2.6) depends upon the hatch space value. The previous experiments show that the surface roughness fluctuates by changing in overlapping ratio in a way that it will be minimum at k=29.3%, 59.2%, 71.7%, etc. (Fig. 2.7). The general trend shows that the surface roughness becomes smaller with increasing scan overlap or in other words, reducing the hatch space. The

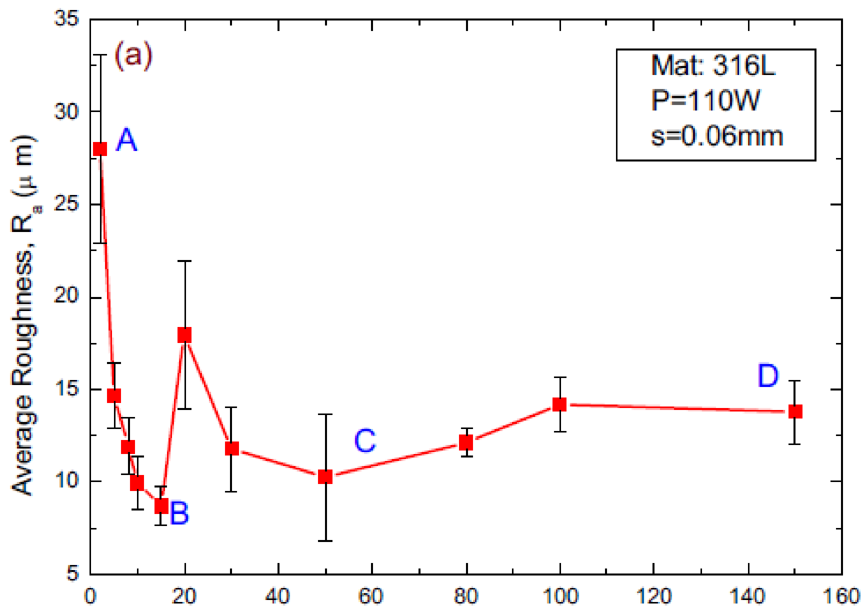

Figure 2.5. Measured average roughness at s = 0.06 mm for 316L [39]

two highly recommended optimized values in terms of reproducible geometry for the tracks are 29.3% and 59.2% [22, 39, 46].

It is noteworthy that in the DMLS process, decreasing the hatch space to 0.15 mm is able to improve the inter-track bonding (reduce sintered porosity) and hence, reduce the surface roughness [42, 47].

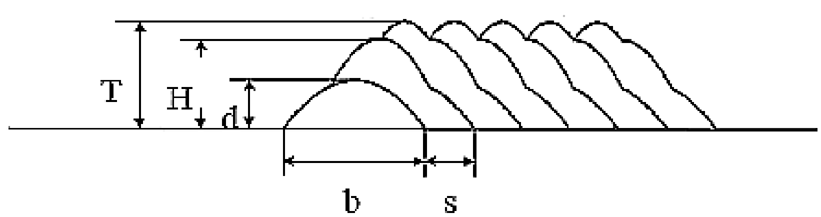

Figure 2.6. Parameters in overlapping ratio [22]

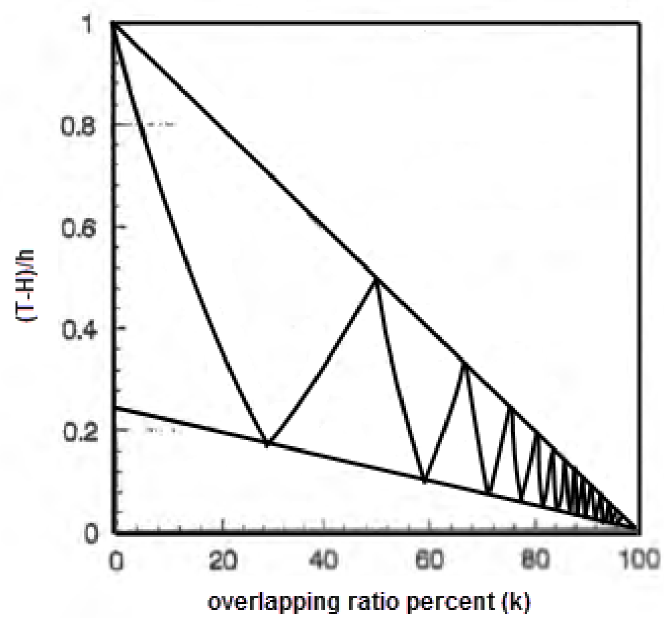

Figure 2.7. Surface roughness as a function of overlapping ratio [22]

It should be noticed that altering the parameters mentioned above in section 2.2.1.1 affect energy density. In general, surface quality increases by using higher energy density [48]; however, as Fig. 2.8 shows that super high energy density leads to super-elevation in the border of the manufactured geometry in SLM process [49, 50].

Larger spot size leads to lower roughness [44] and also an increase in the laser pulse length leads to an increase in the surface roughness in the vertical build direction [51].

Powder deposition Uniform powder deposition, smooth deposited powder layer, and uniform spreading are crucial for surface quality. In this regard, the deposition mechanism and efficiency of powder fluidity are two significant contributing parameters.

There are three types of deposition mechanisms: rotating/counter-rotating roller, wiper blade, and slot feeder. Four aspects need to be controlled in these mechanisms [22, 49]:

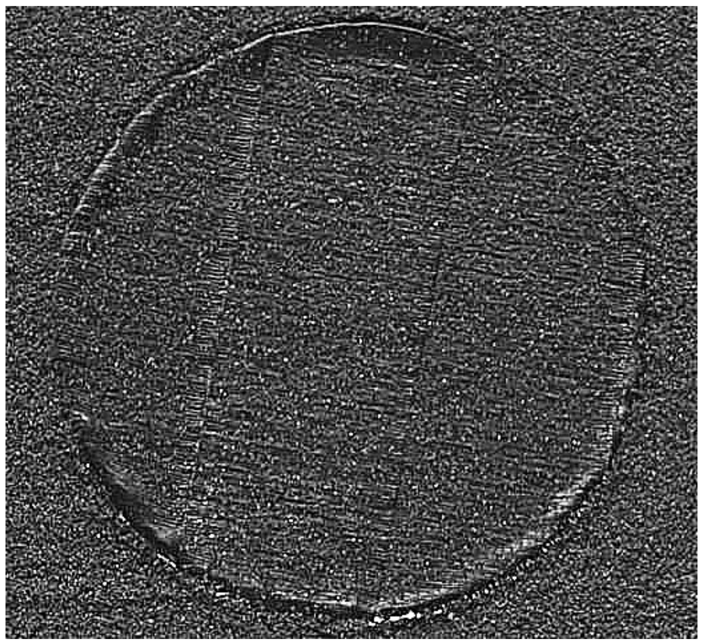

Figure 2.8. Super-elevation in the border of a fabricated cylinder in the SLM process [49]

1. The quantity of powder: surplus powder is needed to ensure complete coverage.

2. Surplus powder leads to increased weight, which increases friction between the new layer and the solidified layer leading to misalignment of layers. Bonding the first layer to a wire mesh solves this problem.

3. The scraper blade touches the powder along with a fixed line so, any scratch on the blade leads to some irregularities swept along the layer.

4. The deposited powder cannot be compacted by using a scraper blade.

The literature recommends combining the two approaches, namely, the hopper (slot-feeder) and rolling; in this case, items 3 and 4 above are solved and only the height (vertical dimension) needs to be monitored. Furthermore, large balling damages the paving system and as a result, it cannot distribute powders uniformly. This problem may eventually stop the process (Fig. 2.9) [52].

Powder specifications affect significantly powder fluidity in a way that if the particle size is too small and the shape is too irregular, they will impede the smooth deposition of layers. Generally, finer particles will produce the best surface finish under ideal melting conditions; however, a decrease in powder size increases some weak forces such as Van der Waals attraction forces, electrostatic charges, magnetic forces, and capillary liquid forces, which reduce powder fluidity. Furthermore, particle shape, surface area, surface roughness, and surface chemistry are also affected significantly by the bulk of powder. In fact, more surface roughness, surface area or smaller size of powder particle leads to the bigger amount of friction within a powder mass and hence, less flowability. It should be noticed that spherically shaped particles lead to ideal flow properties [53-56].

Pits on the surface Sometimes some spherical particles, which are bigger than the layer thickness, are created due to rapid solidification. These particles are broken from the surface by the recoating blade (Fig. 2.10), which leads to pits on the surface. Large pits in an area with limited melt pool overlap could be a source of defect for the new layer. [57].

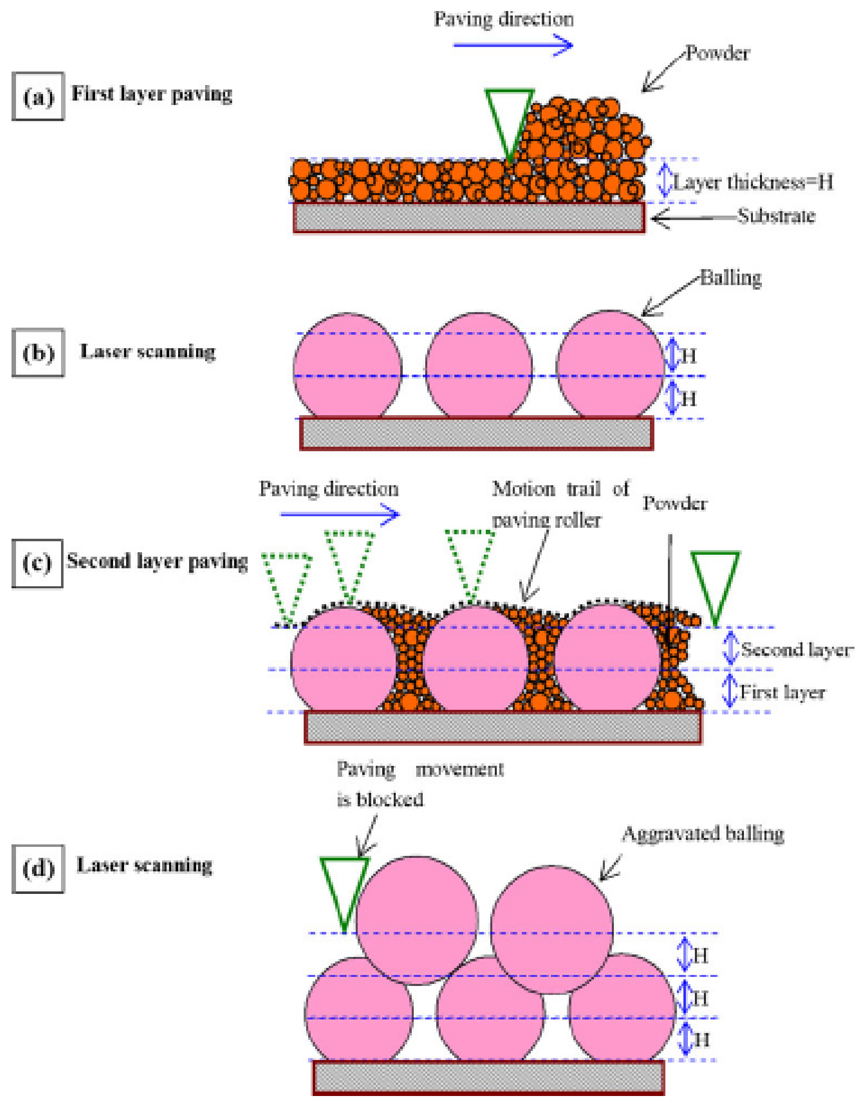

Figure 2.9. Schematic diagram showing big-sized balling block effect [52]

Fractures, cracks, and holes Altering scan specifications can result in fractures, cracks, and holes on the surface. For instance, higher scan speed and scan length lead to more narrow and deep longitudinal cracks on tracks (Fig. 2.11), which are mostly generated in zone III shown in Fig. 2.12.

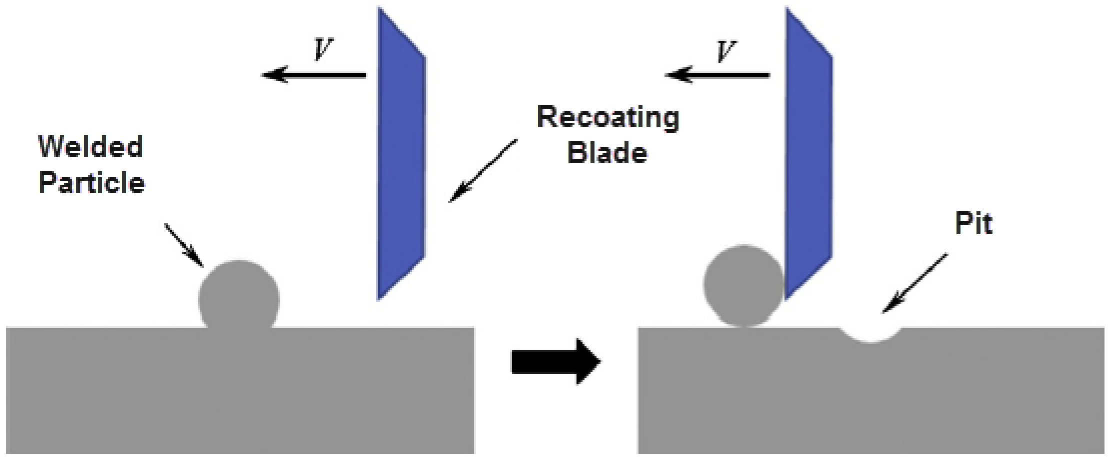

Figure 2.10. Defect caused by recoating blade [57]

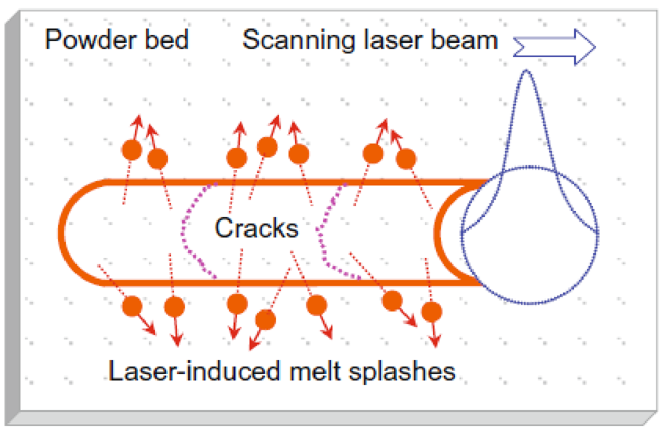

Figure 2.11. Creating longitudinal cracks on tracks [58]

The quality of the substrate The roughness of the deposited layer has a significant effect on the surface quality of the subsequent layers. This is because a rougher surface leads to defects, such as more porosity and less bonding between two adjacent tracks or layers [46].

Staircase effect The staircase effect is one of the other contributing parameters for surface quality, which was explained in "Geometric inaccuracy (from dimensional deviations)."

Surface orientation Reference [59] measured the surface roughness, in terms of R_a (average roughness) and R_z (surface roughness depth). The work shows that the roughness of side surfaces is better than top surfaces. For instance, in a fabricated artifact, the side surface revealed R_a equals 3.9 ± 1.4 µm and R_z equals 24 ± 1 µm while the top surface revealed R_a equals 7 ± 0.5 µm and R_z equals 35 ± 3 µm.

Balling

One of the most referenced defects in the scientific literature is balling. This phenomenon, which may form some discontinuous scan tracks, is affected by numerous contributing parameters including energy density (energy input), contained gas of chamber, the rate of cooling, powder effect, Plateaus coefficient (Rayleigh-Plateau limit) and poor wetting which are explained in the following sections.

Energy density (energy input) Energy density or energy input is a factor that correlates laser specifications and layer thickness. One equation, which estimates this factor, is $\mathrm{E} = \dfrac{P}{v \times h \times d}$ in which P is laser power, v is scan speed, h is hatch space and d is layer thickness. Generally, increasing the energy density decreases the possibility of balling (zone IV in Fig. 2.12). More balling phenomena produces more rough tracks and as a result, decreases surface quality [58, 60]. It is also recommended that the heat input can be controlled more precisely with using laser pulse mode. This feature can be leverage in online controlling approaches [61].

The other equation introduced in some literature is $\mathrm{E} = \dfrac{p \times \dfrac{t}{h \times l}}{d}$ in which t is exposure time and l is point distance [62]. It also mentioned that energy density, and as a result energy absorption, is increased by with the decrease in spot size [22, 48].

Contained gas of chamber Any miniature changes in the chamber-contained gas can lead to some serious defects in the manufactured part. Because, additional

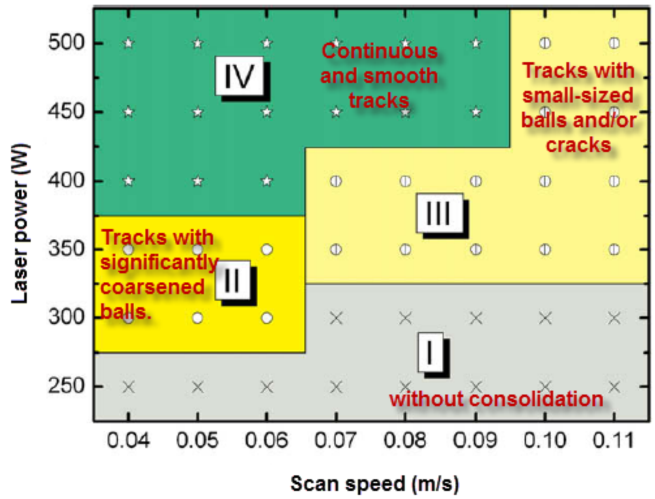

Figure 2.12. Effect of laser power and scan speed on balling phenomena [58]

solute oxygen leads to instability in melt beads and thus, reshape tracks into balls such that by increasing the oxygen content from low ($\sim 0.1\%$) to high ($\sim 2\%$ to $\sim 10\%$), the balling size goes from very small to large. As a matter of fact, the balling phenomena appears in a surrounded air situation when the ratio of melt pool length to width reaches a critical value close to π [22, 52].

Rate of cooling Contact of the melt with a cooler substrate leads to reshaping the tracks into balls [22].

Powder effect Heating pre-alloyed powder to the mushy zone increases the resistance of powder to balling because of increased melt viscosity. On the other hand, balling is more difficult to control when involving smaller particles due to Marangoni convection which occurs due to the high oxygen content of the powder and high input energy [22].

Plateau's coefficient (Rayleigh-Plateau limit) Rayleigh-Plateau limit (RP_L) or pinch effect refers to the condition where $\lambda/2r = \pi$. Under this condition, the structure of a liquid cylinder, i.e. laser track, collapses into a series of droplets (balls) when the length (λ) of cylinder exceeds its circumference [22].

Poor wetting High scan speed and low scan power lead to poor heating of the substrate. This poor heating leads to poor wetting which causes balling; on the contrary, oxide reduction, removal, or prevention leads to significant improvement in the wetting conditions. Also, the surface quality of the melted powder, the temperature of the workpiece, radiation wavelength, and polarization affect absorptivity and hence, wetting between the liquid and solid phases [22, 63].

Surface deformation

Warping and distortion are two types of surface deformation that are mainly created by thermal specifications of the process. Warping means a surface bent out of its natural shape while distortion means any type of changes, not necessarily bending, in the appearance of the surface. These defects are mostly caused by thermal gradient between the scanning zone with accumulated heat and the zones with lower temperature in the fabricated layer. Smaller hatch spacing increases heat accumulation because of slow cooling of the layer; however, it leads to a homogeneous and continuous layer. Furthermore, it gradually increases the average temperature of the powder bed. The other contributing parameters that lead to these defects are as follows [64, 65]:

Warping Thermal stress, laser power, and scan length are three main contributing parameters for warping.

Thermal stress leads to distortion and warpage, because of the thermal gradient that exists between different zones of a layer as well as, between the current layer and substrate [66-71].

Adjusting laser power according to proximity and the extent of formerly melted powder can have a significant effect on uniform sintering, avoidance of warping, poor adhesion between layers, and part growth near the edges [22]. If the laser power increases enough, powder particles are melted in the SLM process. Generally, surface quality in SLM is less compared with the SLS process and the reason is that melt pool instabilities lead to low surface quality for down-facing surfaces and higher roughness for up-facing surfaces [72].

It is possible to elude layer warping by retaining scan length (length of tracks) below 15 mm [22].

Layer distortion Scan specifications, deposition-starting point, length of the plate, and the number of layers are reported in the literature as the contributing parameters for layer distortion.

When the scan speed is decreased below a certain value, serious thermal deformation occurs. This value is dependent upon the laser power and type of material used [57]. Furthermore, scan pattern, as another scan specification, has a significant effect on thermal evolution and thus, thermal deformation [73].

The test shows that if the deposition starting point is rotated by 90 degrees in each new square layer, the bending distortion reduces in a way that the total distortion of 50 layers obtained by rotation of starting point will be approximately twice as large as the distortion of 10 layers obtained without rotating the starting point [74]. Furthermore, an increase in the length of the plate leads to an increase in the deformation at the end of the plates [25]; also, the total deformation increases with the increase in the number of layers (Fig. 2.13) [25].

Surface oxidation

Both protective ambient atmosphere and contaminant sources such as powder production, storage, and handling, significantly affect surface oxidation, which decreases surface quality.

The most suitable atmospheres for SLS are vacuum sintering and vacuum sintering with inert argon or nitrogen gas. Use of argon gas has been recommended because it leads to high density and adequate finished surface without the need to treat powder

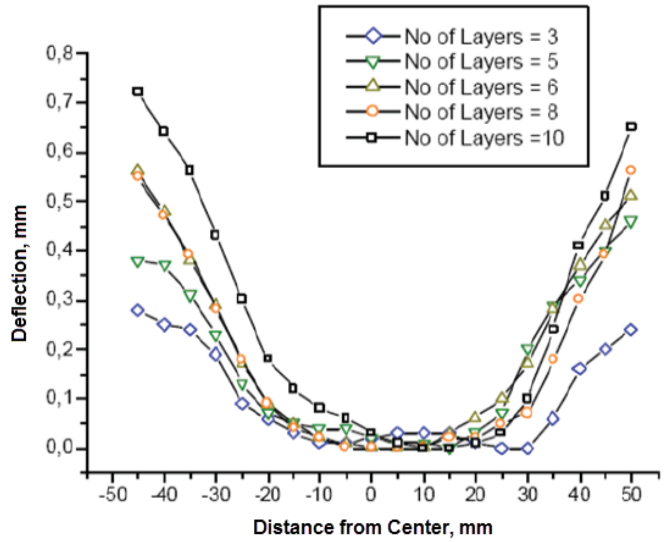

Figure 2.13. Number of layers vs. deformation in metal plates [25]

and better densification, especially in higher scan speed. However, scholars use treated powder to control oxidation in a vacuum atmosphere for SLS. It is also mentioned that percolation of contained gas through the powder layer and using a smaller size of powder decreases the possibility of oxidation [22, 75].

2.1.4 Defects related to microstructure

Anisotropy, heterogeneity, and porosity (poor density) are the defects, which have an effect on the microstructure of the fabricated part. The contributing parameters for each defect are summarized below:

Anisotropy

Scan direction and layer orientation can affect the isotropic property of fabricated part.

Scan direction The scanning direction affects the tensile strength, elongation, and other mechanical properties. A multidirectional scanning mode is required to print isotropic parts [46, 76-78].

Layer orientation Different layer orientation relative to Z-axis leads to different compressive strength with a maximum at 90° and minimum at 0° and 45° (Fig. 2.14). Thus, it is concluded that AM-made parts are structurally and mechanically anisotropic [79, 80].

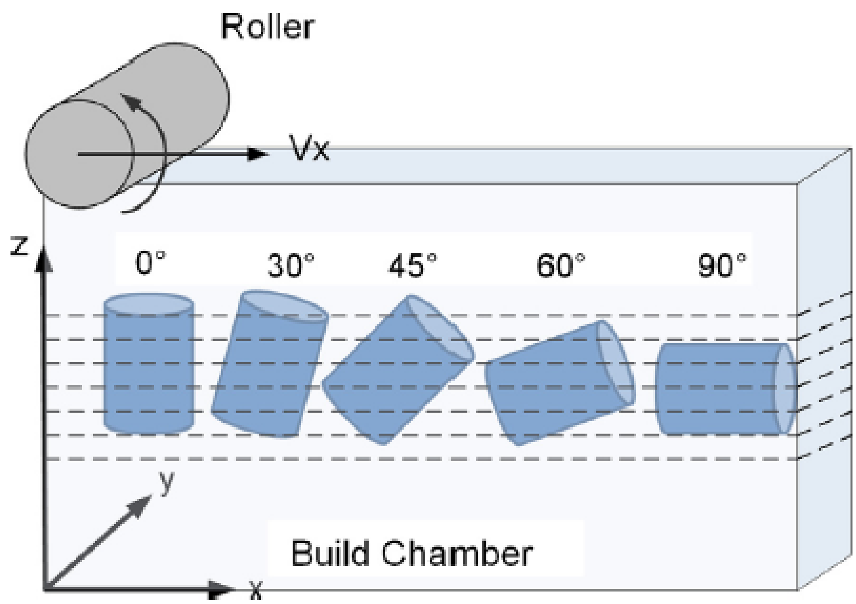

Figure 2.14. Part printed in five different layer orientation [79]

Heterogeneity

Powder conditioning, scan strategy, energy density, temperature, and solidification condition are contributing parameters that cause heterogeneity, as described below.

Powder conditioning Powder conditioning leads to improvement in both melt density and density homogeneity. One approach is to put powders in a vacuum condition for 12 hours at a temperature of 450°C [22].

Scan strategy Scan pattern affects the homogeneity of the manufactured part. Raster scanning often produces inhomogeneous layer properties; similarly, short hatch space leads to a less homogeneous part [22, 24].

Energy density The higher energy density leads to better microstructural homogeneity [47].

Temperature The varying temperature during layer deposition leads to heterogeneity [81].

Solidification condition Different solidification conditions lead to different grain structures which lead to heterogeneity [72, 81].

Porosity (poor density)

Porosity is one of the most frequent defects in the SLS process, which leads to poor density. Generally, maximizing the size of the fusion zone minimizes the inter-run porosity. Thus, there are numerous parameters which can increase the level of porosity including laser specification (laser power, scan speed and spot size), laser mode, scan strategy, balling, powder size, powder morphology, drying treatment, layer thickness, melt pool size and morphology, poor wetting, powder packing density (powder apparent density), overlapping ratio, entrapped gas, layer orientation, densification, and gas flow condition. More details about how these parameters correlate with the porosity of fabricating parts are explained in the following subsections.

Laser specification As Fig. 2.15 depicts, higher laser power or lower scan speed, or in other words, higher volumetric energy input leads to less porosity. This is because absorbing more energy by powders increase sintering and leads to larger inter-agglomerate sintering necks form; as a result, less porosity is generated [48, 59, 60, 72, 82-87].

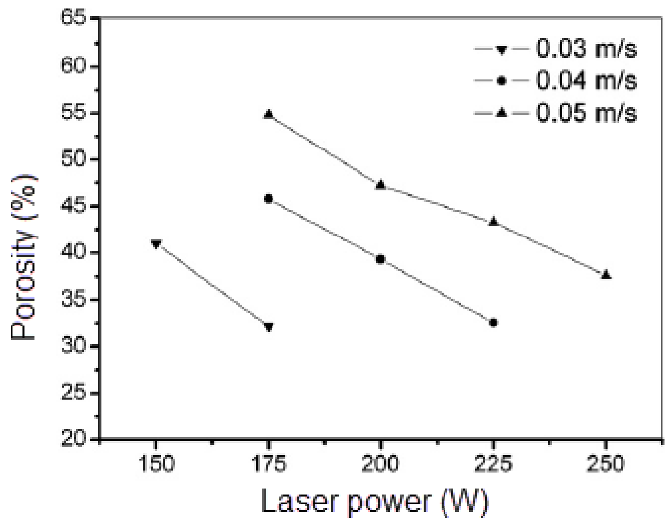

Figure 2.15. Variation of porosity by changing laser power and scan speed for SS 316L in the DMLS process [84]

On the other hand, penetration depth is decreased by large spot size or too low laser power compared to layer thickness. The lower penetration depth, which causes un-melted powder particles underneath of tracks, leads to porosity [57].

Furthermore, scholars have shown that an optimum value for laser energy density that minimizes porosity in the manufactured parts (Fig. 2.16). Values below optimum lead to discontinuous tracks with some gaps in between as well as generate some small size of balling (smaller than 50 µ). On the contrary, higher than this value leads to an increase in balling with bigger size (around 100 µ) because of changes in the composition of molten materials and increase in surface tension [9, 62, 77, 83, 88, 89].

There are various benchmarks in the literature depicting the correlation of laser power and scan speed with porosity (see Fig. 2.12, Fig. 2.17.a and Fig. 2.17.b for instances) [58, 90]. Fig. 2.17.a reveals five different zones as follows: Z1: interconnected porosity occurred mainly at temperatures below the melting point, Z2: inter-run porosity, Z3: a highly dense structure but with small areas of isolated porosity, Z4: a highly dense structure but with large areas of isolated porosity and Z5: a

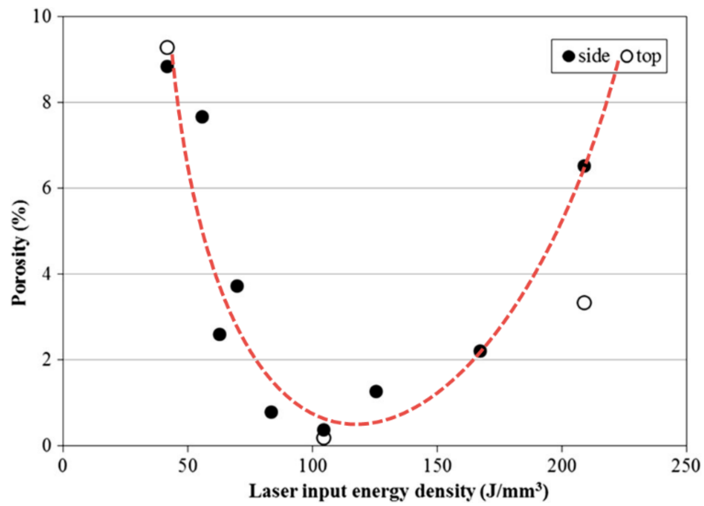

Figure 2.16. Energy density vs. percent porosity [62]

fully dense structure with no porosity [22]. Fig. 2.17.b also revealed the same type of information for 316L Stainless Steel in the DMLS process, in which the different zones are: Zone I: no melting area (powders are not sintered), Zone II: partial melting (porous sintered surface), Zone III: melting with balling (coarsened metallic balls) and Zone IV: complete melting (fully dense sintered surface).

Laser mode Pulsed mode consolidates the metallic powders at a lower average power as well as increase the density of the consolidated part compared with continuous wave [30].

Scan strategy Different scan strategies including various scan pattern, hatch space, and remelting strategy can be employed during the fabrication of a part, which affects porosity [91, 92].

Six different scan patterns are introduced in references [65, 93]: X is assigned to a unidirectional scan. 2X is similar to X, but with each layer scanned twice. In an Alternating strategy, the start point is rotated by 90° in the next layer. X& Y 2HS demonstrate that each layer is scanned twice with perpendicular tracks and different hatch spaces. In the Pre-sinter strategy, the layer is first scanned by half the power

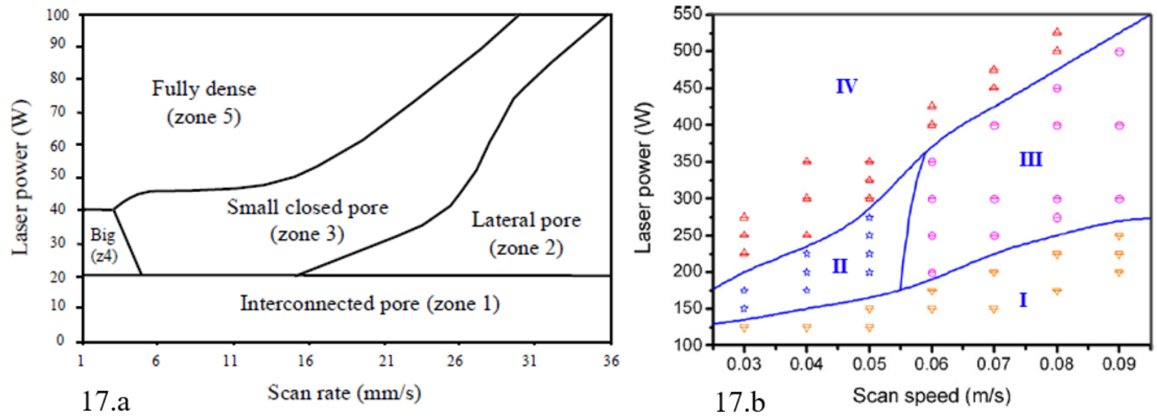

Figure 2.17. Correlation of laser power and scan speed with a porosity of a single layer (b: for 316L SS in DMLS process)[22],[84]

and then, it is followed by a second scan with full power. In the Overlap strategy, each layer is scanned twice with overlap between every two adjacent tracks. The results are compared in Fig. 2.18. This figure reveals that the best densities for minimum velocity (v = 500 mm/s) and for maximum velocity (v = 1000 mm/s) are obtained by the pre-sinter strategy.

The larger hatch space leads to more porosity [52, 84, 94].

Using laser remelting after every layer can eliminate pores created between neighboring melt pools and increase the density to almost 100% in parts manufactured by SLM [45, 89].

Balling Balling is a dominator factor in single layer porosity because of pores between metallic balls [22, 95, 96].

Powder size Smaller powder leads to less porosity. This is because larger size powder (more than 100 µ) requires higher energy density for melting, resulting in more porosity for a specific energy density [84, 97, 98].

Powder morphology More spherical and less irregular powders create less porosity because of better flowability and less surface contamination [54, 55, 99].

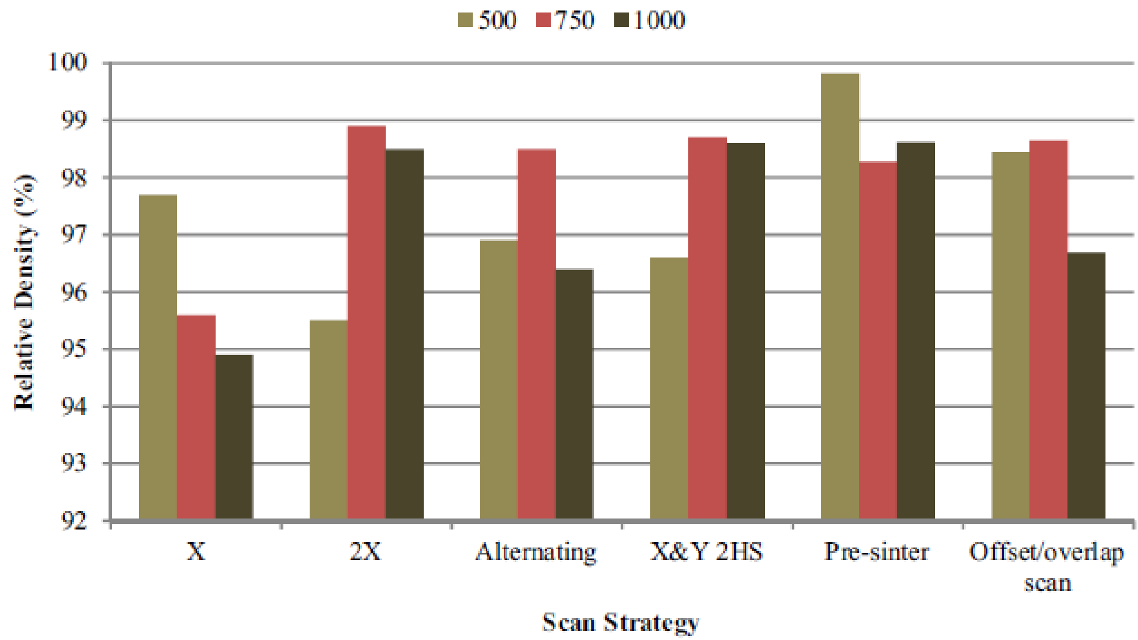

Figure 2.18. Influence of scanning strategy on relative density [65]

Drying treatment The untreated or coarsely treated powder will lead to more cracks and porosity, regardless of the environmental factors. This problem may be overcome by heating powder during pre-processing between 100°C to 1000°C [22].

Layer thickness Lower layer thickness leads to deeper laser penetration, which leads to better bonding between sequence layers, less porosity and thus, higher density. It should be noticed that layer warping and irregular layer thickness are the initial reasons for inter-layer porosity [22, 84, 94].

Melt pool size and morphology Generally, in SLS, powder particles are sintered in solid state sintering [100] and the concepts of melting and melt pool are mostly relevant to SLM; however, melt pool may be created in SLS when the heat density is increased because of the type of scan pattern, remelting strategy, etc. As such, factors which affect the generated melt pool, including Marangoni convection, energy density, scan overlap, and purity of powders, should be considered. A significant factor changing melt pool morphology (melt pool cross-section) is Marangoni convection. This phenomenon can generate deep narrow tracks that reduce the bond between them and thus, increase the inter-run porosity. The effect of Marangoni convection is controlled by altering the hatch space and scanning strategies [22].

Exerting high energy density by using excessive laser power or underdone scan speed magnifies the width and depth of the melt pool [39, 64, 76, 101]. As shown in Fig. 2.19, increasing scan overlap reduces the melt pool depth or penetration [22].

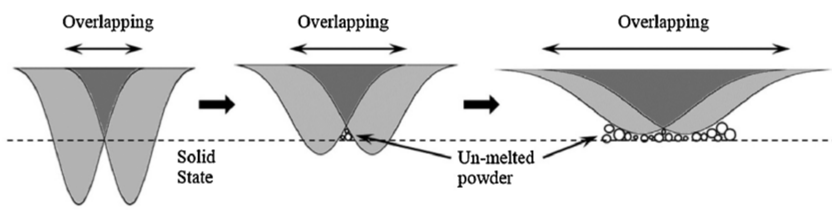

Figure 2.19. Effect of overlapping on penetration depth [57]

Higher purity of metals and alloys powder with low oxygen and Sulphur create a wide, shallow melt pool [22].

Poor wetting Poor wetting increases inter-run porosity because the wetting angle must be acute (Fig. 2.20) unless some porosity is created between the tracks. This angle depends upon the energy density [22, 102].

Powder packing density (powder apparent density) The density of deposited powder in a layer with a high packing has a significant effect on the final density of the sintered or melted layer in which the density increases by elevating the apparent density. The contributing parameters are particle size, particle shape, particle size distribution, and mixing, in a way that mixing different size of powders enhances the apparent density. It should be noticed that the apparent density of powder with dendrite shapes is significantly lower than the spherical ones [103-106].

Overlapping ratio High overlapping ratio (Fig. 2.7) leads to inter-run porosity [22].

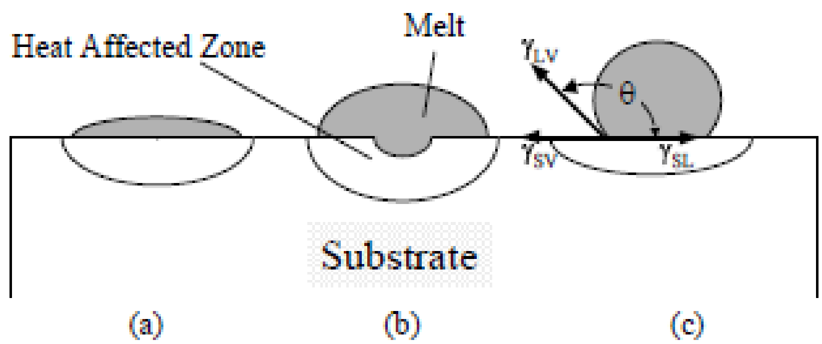

Figure 2.20. Three types of wetting angle when a track bonds to a solid substrate [22]

Entrapped gas Sometimes small pores are generated because of trapped gas between powders. One reason for generating the gas bubbles is exerting high energy density to the melt pool, which leads to gas bubbles release due to vaporization of the low melting point of the combinations of the alloy. The released gas forms some porosity because high solidification rate of the melt pool does not permit the gas bubbles to rise up and escape out of the molten area. These pores may be eliminated by scanning of subsequent layers [57, 63].

Layer orientation Five different layer orientations were examined (Fig. 2.14); the results reveal that the layer orientation relative to vertical Z-axis has an effect on porosity and as a result, compressive strength in a way that the lowest porosity (the highest compressive strength) exists at 90° and the weakest compressive strength (the highest bulk porosity) exists at 0° and 45° [22, 79].

Densification The ratio of the void fraction of the powder bed in the SLS process complies with the first order kinetic law ($\frac{\partial \epsilon}{\partial t} = -k'\epsilon$). In this equation k′ is sintering rate, ϵ is void fraction of the part, which varies between ϵ_b (which is the initial void fraction of the powder bed before the start of laser sintering) and ϵ_s (which is the minimum attainable porosity in a sintered part, which varies between 0.02 and 0.3 according to the material used). The sintering rate (k′) is a function of the laser energy input. Hence, the sintered density of metal powders in the SLS process should be an exponential function of the laser energy input ($\ln(1-D) = -K\psi$) where ψ is specific energy input and D is densification factor defined as $D = \dfrac{\epsilon - \epsilon_b}{\epsilon_s - \epsilon_b}$. The exponential function reveals that increasing energy density leads to better densification but there is a saturation level and thus, even using very high energy density does not lead to full density.

Optical microscopy images show that after densification the microstructure in SLS is significantly similar to the equilibrium state, as with the conventional powder metallurgy (PM) or cast (Fig. 2.21) [56, 100, 107].

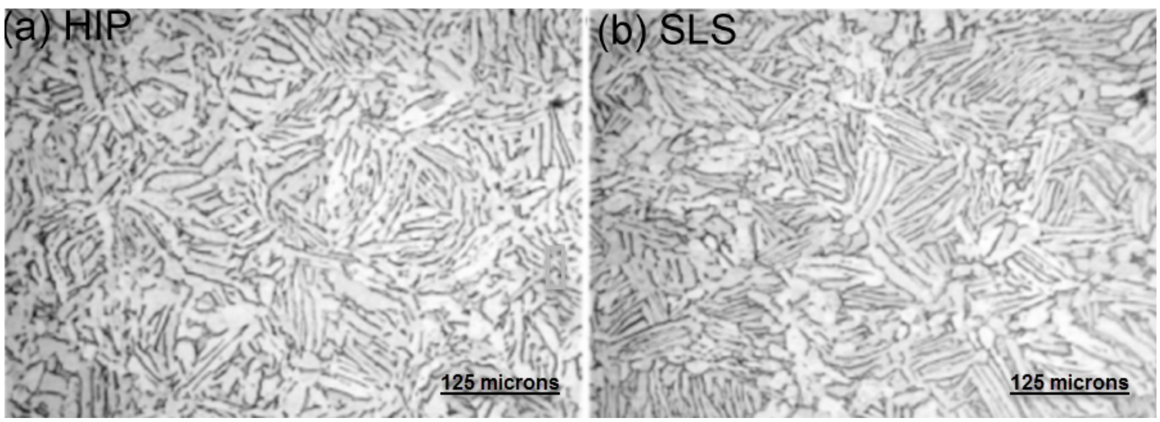

Figure 2.21. Optical microscopy images of (a) a HIP Ti-6Al-4V and (b) an SLS then HIP Ti-6Al-4V [100]

Gas flow condition More uniform gas flow rate across the build area causes less porosity in the fabricated part. It is also shown that the effect of gas flow decreases as it becomes more uniform [108].

2.1.5 Defects related to weak mechanical properties

Fractures, cracks and holes, inadequate bonding between layers (inadequate fusion bond), porosity, and low strength are the defects resulting in weak mechanical properties.

Fractures, cracks, and holes

These defects lead to weak mechanical properties, which were explained in section 2.2.1.4.

Bonding between layers (fusion bond)

The value of layer thickness, Marangoni convection and heat penetration, scan overlap, spreading of deposited powder, pulse ratio, and gas flow direction affect the bonding between layers. Less bonding leads to weaker mechanical properties.

Layer thickness is an essential contributing parameter in bonding between layers, which is highly affected by the spreading mechanism. Its value is often kept constant during the process between 50 µm to 1.5 mm, which significantly affects construction speed. Minimum layer thickness is selected based on particle size and largest powder agglomeration. Smaller layer thickness will increase the bonding between layers because of a better re-melted substrate [99, 109].

The primary factor for the strength of the fusion bond between layers is heat penetration, which is highly affected by energy absorption and Marangoni convection; more energy absorption leads to deeper penetration. Marangoni convection is just affected by soluble oxygen and not a surface film of oxygen [22, 110].

Increasing the scan overlap decreases the melt penetration which leads to less bonding between layers [22]. Surface irregularities are significantly dependent on the spreading of deposited powders. These regularities highly affect the bonding between layers [22].

Reducing the pulse ratio leads to discontinues input energy and thus, unstable melt pool depth, which leads to less bonding between layers [51].

Experimental results show that parts fabricated perpendicularly to the gas flow direction has significantly more bonding between their layers and thus, better mechanical properties compared with parts fabricated parallel to the gas flow direction [111].

Porosity

As it is explained thoroughly in section 2.3.3.14, more porosity leads to weaker compressive strength [79, 112].

Low strength

The strength of a fabricated part is highly dependent upon scan strategy, powder specifications, and gas flow rate.

Scan pattern (or strategy) and scan direction effect on isotropy, homogeneity and thus, tensile strength, elongation and other mechanical properties [22, 113]. References [86, 114] discuss the effect of scan spacing and sintering speed on the hardness of the fabricated part and emphasized the significant effect of scan spacing in the DMLS process. Fig. 2.22 shows the correlation between sintering speed, scan spacing, and hardness.

Hardness is a function of powder specifications such as grain size and grain structure of an individual particle in a way that the hardness of solidified tracks increases with a decrease in particle size. The other thermal and physical specifications of powder such as specific heat, thermal conductivity, and density are very effective on mechanical properties of the final part fabricated by SLS process. The literature shows that micro-hardness increases with increasing powder flow rate [22, 115-117].

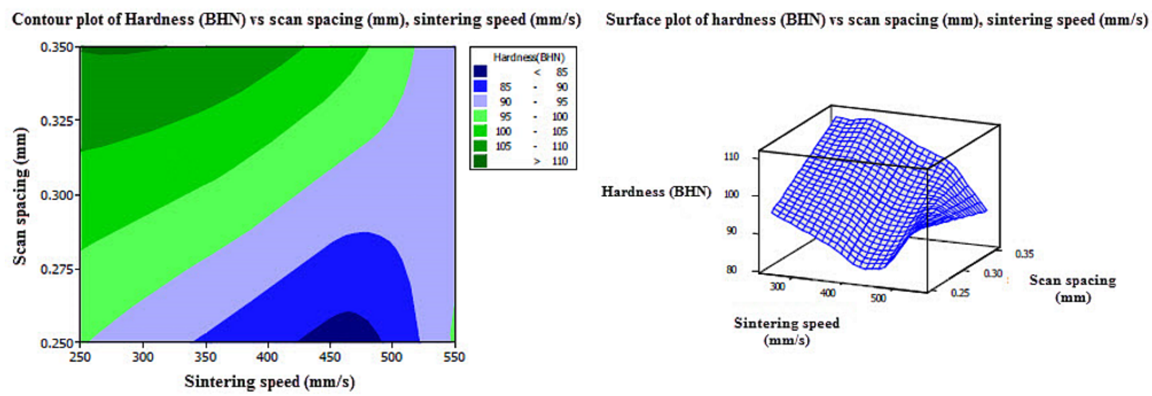

Figure 2.22. Correlation between sintering speed, scan spacing and hardness in the DMLS process [114]

The increase in gas flow rate creates higher disturbance in the powder flow path reducing track width and height. This issue decreases the micro-hardness of the fabricated part [115].

2.2 Defects, process parameters and signatures for online monitoring and control

2.2.1 Introduction

This chapter contributes to a better classification of defects in the powder-bed fusion process to support online monitoring and control. Furthermore, this chapter summarizes the process parameters and the affected items to develop online monitoring, control, and error handling strategies. It also proposes an approach to applying the concept of signatures in online monitoring and control. This is a way of controlling part quality indirectly. A primary control strategy devises a methodology for online certification of the fabricated part layer by layer.

2.2.2 Classification of defects

There are two main approaches to controlling defects during the AM process, which are described below.

The first approach uses analytical models, in order to predict the values of the process parameters [16, 41, 64, 118-125]. However, there is a lack of mathematical and statistical models and algorithms for the AM process to predict process parameters accurately in order to avoid failures, improve the part quality, and produce a perfect product. These parameters are employed to account for the process specifications such as the material, ambient temperature, geometry, required speed of manufacturing, scan pattern, etc. To date, all of the conducted investigations are based on simulation and physics-based Finite Element Analysis (FEA) that are complex and, introduce high computational burden [64, 74, 118, 119, 126-131]. Efficient analytical and data-driven models that are capable of processing large data streams are strongly needed for real-time control. This limitation is due to the complex nature of the sintering process due to the change in material properties as a result of increased temperature, in the plurality of contributing parameters and process parameters, and the lack of understanding of physical and chemical reactions between powders during the process [12]. These problems encouraged scholars to consider the second approach.

The second approach is the online monitoring (OM) and control [12, 49, 60, 132-151]. The most significant advantages of this approach can be summarized as 1) The approach can be implemented without a full modeling of the physics of sintering phenomena; 2) the approach can be employed to avoid/eliminate the defects precisely. There is a good volume of literature on the different types of defects to avoid/eliminate in order to improve the quality of the final part by adjusting the contributing parameters within their operational ranges [24, 152, 153]. However, there is a lack of effective/systematic classification of the defects, which significantly affect quality matrices of the produced part and their contributing parameters. Furthermore, the correlation between those defects and contributing parameters is lacking. In addition, there is no focus on the most important parameters that can be monitored and controlled to avoid those defects; the literature, however, shows some primary grouping of parameters [138, 139].

This section (as depicted in Fig. 2.1) classifies the different defects (13 in total), mentioned in the previous section, under 1) Geometry and Dimensions; 2) Surface Quality (Finishing); 3) Microstructure; and 4) the defects behind Weak Mechanical Properties. In addition, it explains how the contributing parameters affect the defects.

From an online monitoring point of view, two steps are necessary to reach a flawless part. First, we monitor the process features (both defects and parameters) online in order to detect the generated defects and/or evaluate the conditions, which may lead to a defect. Second, we control the contributing parameters to avoid/eliminate those defects. All these defects and fabrication conditions can be recognized, following the proposed quintuple set of manufacturing features. This umbrella of categorization is established based on three criteria: 1) they must cover all the defects generated during the process; 2) they must allow for the evaluation of the essential contributing parameters for the majority of defects; and 3) they need to be detectable by current monitoring approaches, as well as controllable through process parameters. If this set of features can be monitored and controlled, achieving a flawless part should be possible [53, 141, 142, 154-158].

1. The homogeneous deposition of the powder As previously mentioned, uniform powder deposition, smoothness of every deposited powder layer, and uniform spreading are all very critical to surface quality [142, 159].

2. Thermal characteristics of the layer under fabrication Temperature characteristics such as homogeneous temperature distribution, heat accumulation in different zones, etc. is an excellent proxy [12] in order to attain the best possible homogenous microstructure that directly affects the mechanical properties.

3. Surface quality related defects for a single layer It includes a vast number of defects such as cracks, holes, etc. It is noteworthy that some of the defects such as porosity need to be checked after every specific number of layers [9, 37, 50].

4. Improper part geometry and dimension inaccuracy This is the most important category regarding repeatability. As explained in section 1 defects such as shrinkage leads to some geometric and dimensional inaccuracy [37].

5. Poor bonding between the layers Bonding plays a key role in the resulting mechanical properties and is mainly affected by energy density, penetration depth, and layer thickness [9, 10].

It was found that the defects/features could be handled by just a small set of controllable parameters. [133, 143, 154, 160]. These parameters are derived, classified, and explained in the following section. It also should be noted that current instruments and mentioned approaches in literature can monitor all of these fields, defects, and features [15, 49, 161-170]. Table 2.1 presents the most recommended approaches for monitoring the defects or evaluating the fabrication conditions.

Table 2.1.
Recommended approaches/sensors for OM of manufacturing features

No.	**Manufacturing feature**	**Recommended approaches**
1	The homogeneous deposition of the powder	Image processing for well-deposited powder (using CCD camera)
2	Thermal characteristics of the layer under fabrication	Thermography for layer heat specifications (using IR camera and photodiode)
3	Surface quality related defects for a single layer	Using ultrasound technique or image processing for monitoring surface quality layer by layer
4	Improper part geometry and dimension inaccuracy	Image processing (using CMOS camera) and checking dimension accuracy (using displacement sensor)
5	Poor bonding between the layers	Checking the layer thickness (using displacement sensor or ultrasound techniques) and melt pool depth (using IR camera in SLM process)

2.2.3 Classification of process parameters for online monitoring and control

Nowadays, the parts produced in SLS are used as end-user products. Therefore, producing a part with perfect homogeneous microstructure and exclusive defects is considered an ultimate objective of SLS process which faces a number of barriers, challenges, and gaps, including powder properties knowledge, chain capabilities measurement science, standardization, monitoring defects, and control manufacturing process. Energetics Incorporated addressed these items and prepared a roadmap for NIST to identify the gaps that need to be bridged [171]. Online monitoring and process control could significantly contribute towards achieving that ultimate objective. In this context, there are various defects, signatures, and parameters affecting the quality of a printed part and its microstructure, which can be controlled by aligning process parameters with optimized values through online monitoring. Hence, it is crucial to utilize some techniques to monitor and control process parameters and probably, desired signatures constantly, in order to avoid the defects. To further establish a thorough procedure for effective monitoring and control strategies, the process parameters can be classified into three categories as shown in Fig. 2.23. As this figure depicts, the first category is *pre-processed parameters*, which should be specified before starting the process. This category is divided into two subcategories. The first one consists of the *pre-defined parameters*, which must be chosen or set before the manufacturing process. There is an optimum value or best state to be chosen for each one of them. It is noteworthy that these parameters are constant for any powder bed fusion AM process regardless of the manufactured part. Consequently, vendors will not need to monitor or control them. This category mostly includes powder specifications and machine specifications.

The second subcategory consists of the *Pre-defined parameters that need to be monitored*. The latter includes the parameters inside the chamber as well as machine error parameters. These parameters must be specified before starting the manufacturing process as well, but they can be changed during the process; however, these changes are undesirable and thus, need to be monitored and kept constant. It is important to note that unlike the first group of parameters, they may have a different optimum value or state, based on the chosen material. To sum up, they would need to be monitored online to be kept fixed, but they would not need to be controlled and altered during the process.

The second category of parameters is the most important parameters for online monitoring in the powder bed fusion AM process. This category, referred to as *controllable parameters*, includes process parameters (laser specifications and scan strategy) and manufacturing specifications. These parameters need to be monitored and altered online based on 1) the feedback that controller receives from the sensors to adjust these parameters using benchmarks information; 2) manufacturing strategy such as laser pattern; and 3) the chosen manufacturing preference such as time of manufacturing, desired mechanical properties, density, etc. It should be noted that currently all of these parameters are pre-defined and constant during the manufacturing process; however, the manufacturers can assign the correct value or choose the suitable state of process parameters based on the above-mentioned items. There are two main reasons why these parameters should be monitored and controlled. The first reason is to avoid as many defects as possible and reach the best possible end-user part. In this case, the process parameters, such as laser power or laser speed, would need to be adjusted to their optimized value in real time. It should be noted that all of these parameters can be easily measured and controlled by the machine [140, 172]. The second reason is to eliminate the defects after their detection whenever possible. Actually, defects are created due to some manufacturing uncertainty such as the imprecision of the process, stochastic spreading of powder, the inability to predict and choose the most suitable process parameters, etc. The reason is that there is no analytical model that can be used reliably for a complete prediction of the process [12].

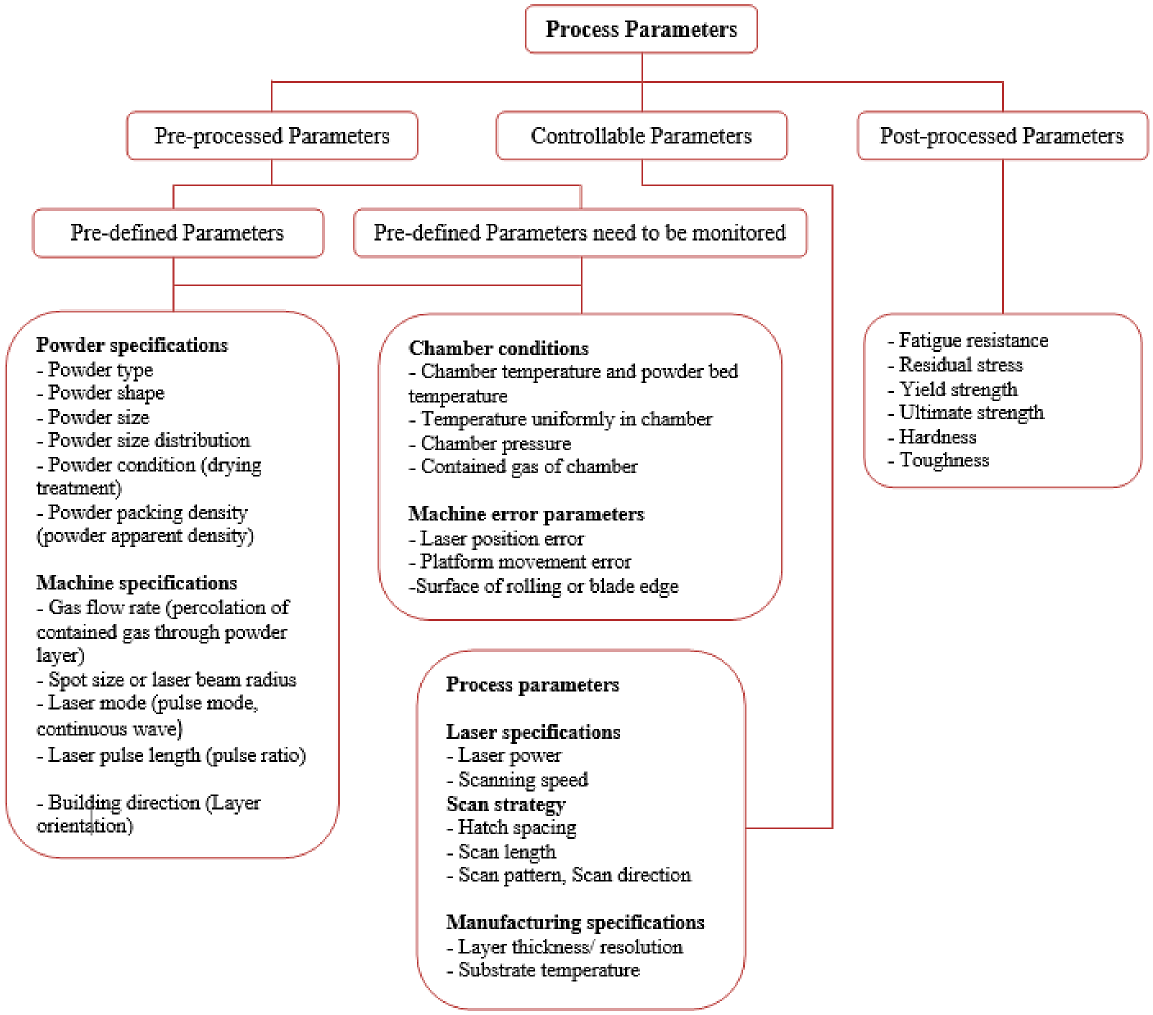

Figure 2.23. Process parameters classification

The final category is post-process parameters which cannot be monitored during the process. These parameters such as yield strength, ultimate strength, etc. expressing the mechanical properties of the manufactured part, are affected by microstructures defects and grain structures, For example, a microcrack can lead to stress concentration which reduces lifespan in fatigue condition [173]. The mechanical properties can be improved by controlling the contributing parameters affecting microstructure. At the very end of the process, these parameters show the quality of the manufacturing process and the success rate of online monitoring approach.

Table 2.2 , which is derived from previous sections, shows the defects or process features for the SLS process affected by classified parameters mentioned above. As depicted, there are only 4 parameters, which need to be monitored and kept fixed (the second category in Table 2.3) and 10 parameters, which need to be monitored and controlled (the third category in Table 2.4). These parameters are recommended for online monitoring and control of the SLS process.

Table 2.2.
First parameter classification using for OM in the SLS process

No.	Process Parameter	Affected items
	First category: predefined parameters	
1	Powder shape	surface contamination, the flowability of a bulk of powder (smooth deposition), powder packing density and powder apparent density, porosity, powder fluidity
2	Powder size	Flowability of the bulk of powder, balling, powder packing density and powder apparent density, material strength, oxidation, layer thickness
3	Powder size distribution	powder packing density and powder apparent density
4	Powder condition/ drying treatment	Balling, heterogeneity, porosity, oxidation
5	Powder packing density/ Powder apparent density	Porosity/ density
6	Gas flow (rate and direction)	Dimensional tolerance, bonding between layers
7	Building direction (Layer orientation)	Dimension inaccuracy, anisotropy, porosity, mechanical properties
8	Spot diameter and beam radius	Dimension inaccuracy, surface roughness, porosity (penetration depth), energy density and energy absorption
9	Laser mode (pulse mode, continuous wave)	Porosity (density), balling (wetting angle)
10	Laser pulse length/ pulse ratio	Surface roughness, bonding between layers

Table 2.3.
Second parameter classification using for OM in the SLS process

Second category: predefined parameters that need to be monitored		
1	Chamber temperature and powder bed temperature (workpiece temperature)	Shrinkage, heterogeneity, surface deformation, absorptivity
2	Gas flow rate	Dimensional inaccuracy, porosity, mechanical properties, bonding between layers
3	Contained gas of chamber	Balling, oxidation
4	Percolation of contained gas through powder layer	Surface oxidation

Table 2.4.
Third parameter classification using for OM in the SLS process

Third category: parameters should be monitored and controlled		
No.	**Process Parameter**	**Affected items**
1	Laser power	Shrinkage, balling (energy density), warping, layer distortion, porosity, melt pool size and morphology, the penetration depth
2	Scanning speed	Shrinkage, surface roughness, balling (energy density, poor wetting), layer distortion, porosity, melt pool size and morphology, fracture/cracks/holes
3	Laser positioning error	Geometry inaccuracy
4	Hatch Spacing	Shrinkage, surface roughness, energy density, heterogeneity, porosity, melt pool size and morphology, dimension inaccuracy (microstructural waviness), surface deformation (heat accumulation)
5	Scan length	Shrinkage, warping, fracture/cracks/holes
6	Scan pattern, Scan direction	Surface roughness, porosity/ density, heterogeneity, anisotropy
7	Platform movement error	Geometry inaccuracy
8	Layer thickness/ resolution	Staircase effect, shrinkage, energy density, porosity/density, bonding between layers/ penetration depth, construction speed
9	Blade edge or surface of rolling	Pit on the surface, powder deposition/ distribution
10	Substrate temperature	Balling, distortion and warpage, poor wetting, melt pool shape

This section recommends the procedure in Fig. 2.24 for online monitoring, online certification, and controlling of manufacturing process layer by layer based on the above parameters. In this procedure, the pre-processing parameters are checked first before starting the manufacturing of a new layer to preclude any diversion in their optimized pre-assigned values; in the next step, the part under fabrication is monitored for probable defects. In this stage, if no defects are detected, the part will be certified and the fabrication process continues. Otherwise, for a non-certified part, there are two possibilities; either the process should be abandoned because of major defects or it can continue under error handling strategies. In the latter case, two different types of defects may be recognized; defect type 1 which is smaller or less serious and can be eliminated by altering the process parameters such as laser power; on the other hand, defect type 2 cannot be removed by just altering the process parameters. Here, it is necessary to pause the modus operandi and manipulate separate error handling strategies. This is because some defects are bigger in size or more serious to be removed by just altering process parameters. After removing this type of defects and before starting manufacturing of the new layer, the controllable parameters set with the prime benchmark values again. This procedure continues to produce an ultimate flawless part.

2.2.4 Use of signatures in online process control

Another way to perform monitoring in SLS or other AM processes is to monitor and measure some signatures instead of monitoring defects and parameters directly. Signatures are defined as some manufacturing specifications or a combination of some parameters, which may be utilized to adjust the controllable parameters to avoid the defects. The Signatures can be divided into two different types: This paper defines the first type as Manufacturing Signatures which are manufacturing specifications that are affected clearly by the controllable parameters; hence, this correlation may be utilized to adjust the controllable parameters. It should be noted that all of these

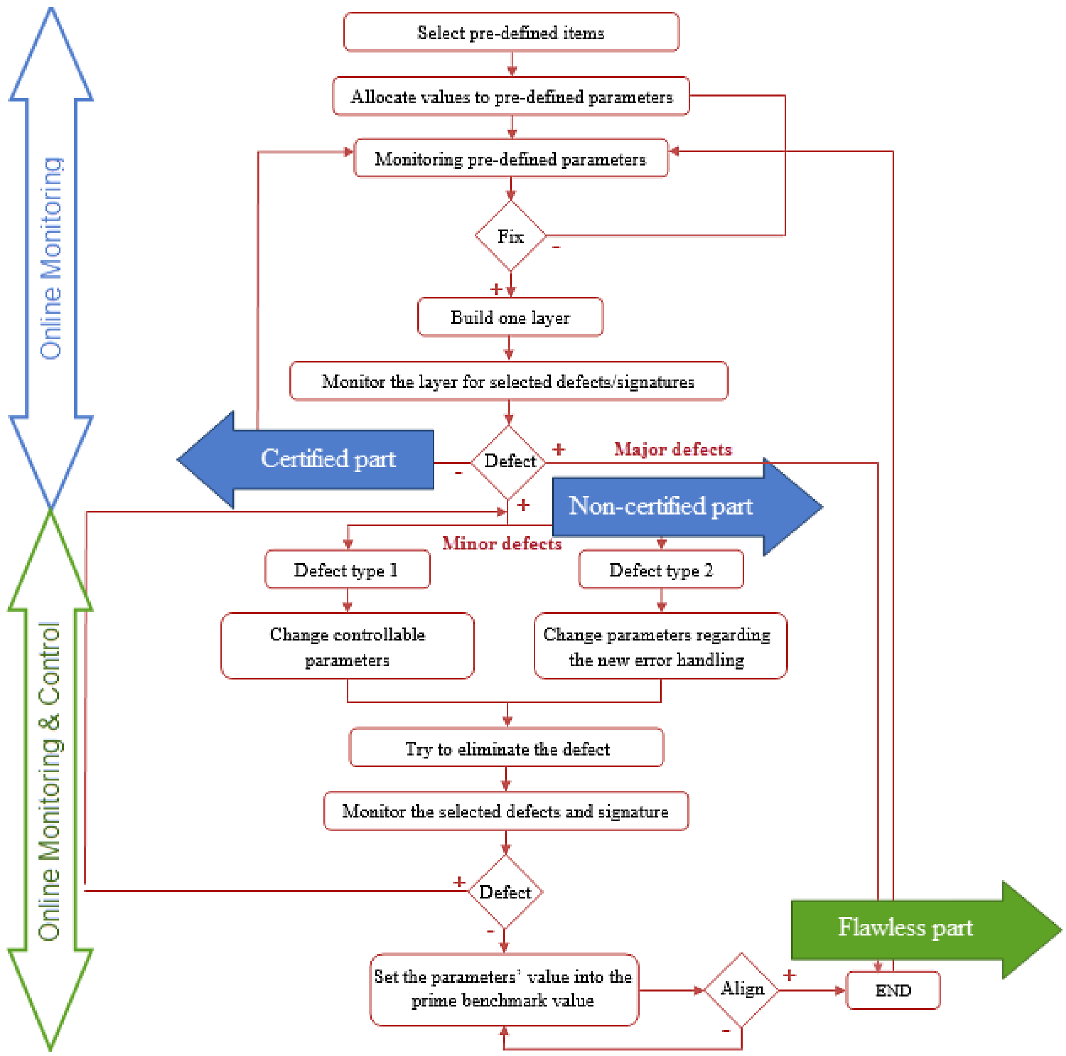

Figure 2.24. General monitoring and control procedure for the SLS process

Manufacturing Signatures relate to melting phenomena and melt pool specification [133, 141, 174-177]. Thus, they are suitable for use in the SLM process. The second type of signature can be defined as Cumulative Signatures which consist of controllable parameters that can be set according to some prepared benchmarks. These parameters can be used for both the SLM and SLS process [15, 154, 178]. The melt pool specifications, Marangoni convection and a feature set of laser scan are recommended in the literature (or here for the first time) to be used as signatures in monitoring. The detailed explanation of the correlation between these items and their contributing parameters was mentioned in section 2.

Manufacturing signature (for SLM process)

Melt pool morphology and melt pool dimensions Melt pool morphology (and as a result melt pool dimension including melt pool depth) has a strong effect on the bonding between scan tracks and as a result, inter-run porosity and final density, balling, Heat-Affected Zone (HAZ), penetration depth and porosity [22, 179, 180]. In HAZ, the dimensions of melt pool grow because of lack of heat conductivity and thus, the surface quality declines significantly. As it is revealed in reference [15], generating support structure can reinforce these areas while improving heat conductivity which leads to better surface quality. The parameters contributing to a melt pool morphology are scan speed, laser power, spot size, overlapping ratio, the number of the laser scan, and the type of powder. It is also possible to map the melt pool dimensions with the generated microstructure to indirectly control solidification microstructure [181, 182].

Melt pool temperature and solidification rate Melt pool temperature, solidification rate, temperature gradient and scan speed are closely related to each other and significantly affect solidification microstructure, homogeneity, and type of grain structure (cellular or dendritic). The governing equation is:

$$\frac{G}{R} = \frac{T_p}{u\ x_1} \tag{2.1}$$

Where T_p is melt pool temperature, u is scan speed, x_1 is the distance between the heat source and the rear of the weld pool, G is temperature gradient, and R is solidification velocity. Furthermore, melt pool temperature affects melt pool depth whose correlation is shown in Fig. 2.25; the solidification rate affects porosity (with entrapping gas), shrinkage, balling, and melt pool geometry.

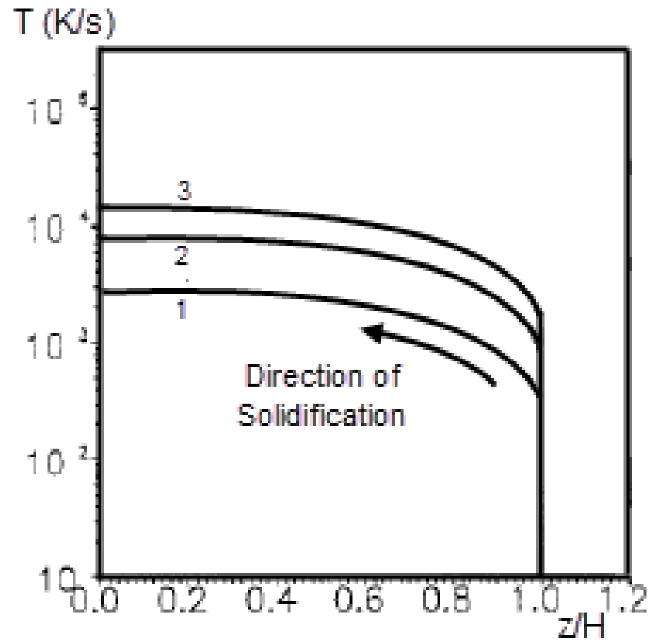

Figure 2.25. Dependence of melt pool temperature T vs. dimensionless melt depth at different scan speed [22]

Marangoni convection (MC) Altering the temperature coefficient of surface tension (due to the variation of the solute oxygen) and generating large thermal gradient between the center and edge of the melt pool (due to the use of laser Gaussian distribution) leads to surface tension gradient. This tension gradient triggers fluid flow in the melt pool causing changes in the temperature gradient. This phenomenon, called MC, changes the melt penetration, generates deep narrow tracks (leading to inter-run porosity), changes bonding between layers, the ratio of depth/width of melt pool and the melt pool morphology (cross section of melt pool). Balling, humping, changes surface morphology, solidification microstructure and warping are other affected items. [22, 47, 121]

Cumulative signature (for SLS and SLM)

Overlapping ratio and energy density (energy input) can be introduced as cumulative signatures. Overlapping ratio affects surface roughness, porosity, and the melt penetration. Energy density, however, can effect on balling, heterogeneity/ homogeneity, density (porosity), melt pool size and melt pool morphology, wetting angle, and solidification.

3. METHODOLOGY: PROPOSED LAYER-BASED TESSELLATION ALGORITHM TO GENERATE A MORE UNIFORM TEMPERATURE DISTRIBUTION

3.1 Study the effect of geometrical features and scanning strategy on the temperature distribution of printed specimens

The literature review in chapter 2 shows that thermal defects and abnormalities are the most prevalent defects, with which the manufacturers encounter. The chapter also explains in warping section that thermal stress, laser power, and scan length are three main contributing parameters for warping. Thermal stress leads to distortion and warpage, because of the thermal gradient that exists between different zones of a layer as well as, between the current layer and substrate [66-71]. In this chapter, we first conduct some primary experiments in FDM process (Fig. 3.1) and monitor the thermal specifications of printed layers to achieve more insight about the warpage and the role of geometrical features and scan strategy on the temperature distribution of printed layers. These experiments provide some information about the effect of size, shape, the distance between features, and the employed scan strategy on temperature distribution. As Fig. 3.2.a and Fig. 3.2.b show, simple rastering strategy generates a significant temperature gradient throughout the printing layers. This strategy exerts the heat flux (deposited filament in the FDM process or exerted laser in SLS process) from one side of the layer and goes along the geometry track by track to cover the entire surface. Fig. 3.2.c and Fig. 3.2.d show the effect of the distance of HAZs on each other. The printed geometrical features are identical in these two samples but they have a different distance from each other. The figures depict that the closer the distance is, the higher the thermal effects they have on each other. In addition, Fig. 28.d shows the greater temperature gradient between the edges and the center of the printed layer. Fig. 3.2.e, Fig. 3.2.f, Fig. 3.2.g, Fig. 3.2.h, and Fig. 3.2.i show the effect of the printed shape on the temperature distribution of the printing layer as well as its warpage. As the figures depict, the shape of HAZs directly affects the temperature distribution and temperature gradient throughout the printed layers. The comparison between Fig. 3.2.e and Fig. 3.2.f reveals that the distortion is larger between the HAZ and the area with no geometrical features to print. Furthermore, Fig. 3.2.g and Fig. 3.2.i show the warpage clearly in the edges and corners of the printed layer. This warpage increases after finishing the printing of the specimens, when they cool down.

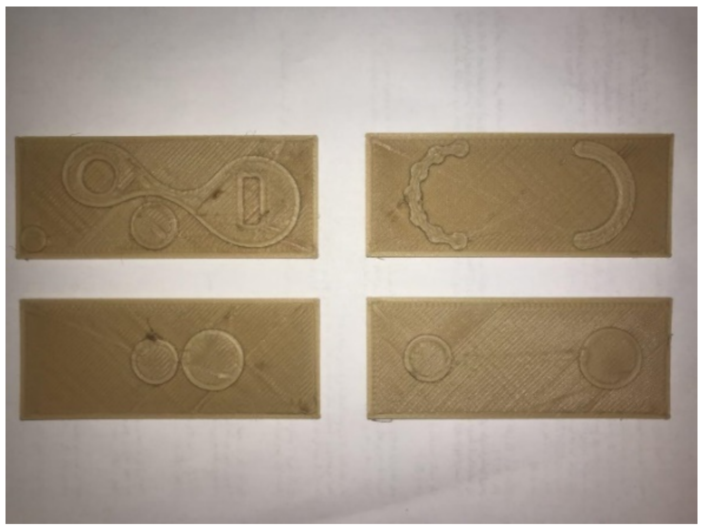

Figure 3.1. Printed specimens with different geometrical features

These experiments lead to proposing an innovative chessboard scanning strategy called tessellation algorithm, which can generate more uniform temperature distribution and diminish the layer warpage consequently especially throughout the layers with either geometry that is more complex or poses relatively longer dimensions. In addition, this chapter introduces an online IR thermography methodology, which helps not only to get more insight for our current experiments but it also helps to evaluate temperature distribution, temperature uniformity, and thermal evolution of

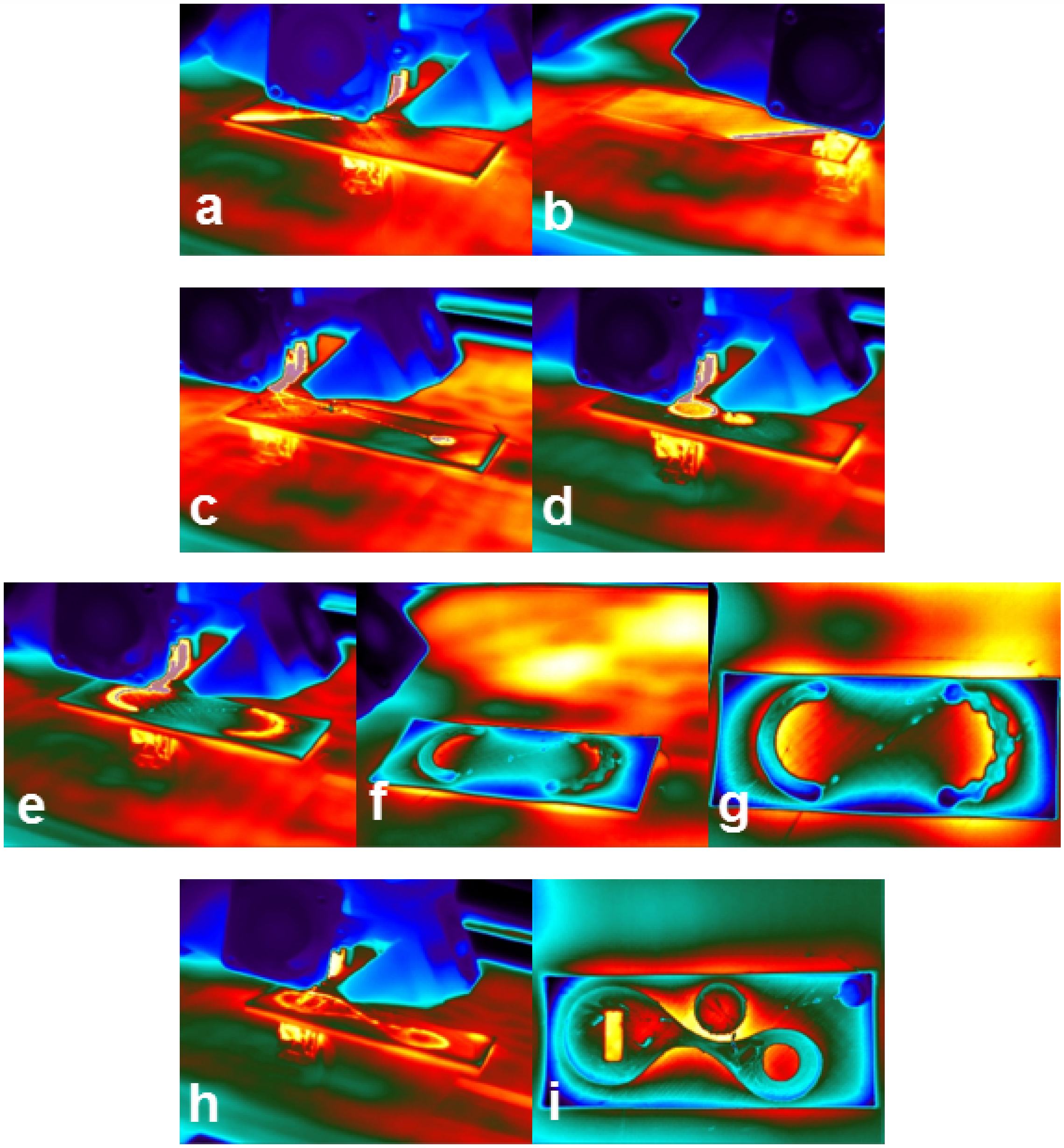

Figure 3.2. Temperature distribution in the printed specimens with different geometrical features

the fabricated layers in FDM, SLS, SLM, or any other thermal inherent AM process. Furthermore, it helps to improve the scanning strategies by sending feedback to a closed-loop controlling strategy. Because controlling of temperature field throughout the layer under fabrication is an excellent proxy for the ultimate quality of the fabricated part, since it has a direct impact on the resulting microstructure, density, and mechanical properties [12, 168, 183]. This methodology utilizes infrared technique and segmentation image processing to extract the required data about temperature distribution and HAZs of the layer under fabrication. The following sections introduce the tessellation algorithm, the IR thermography methodology, and explain how it extracts data about the thermal evolution of printing specimens as well as HAZ specifications.

3.1.1 Introducing tessellation algorithm to generate a more uniform temperature distribution

Introduction to tessellation algorithm

Marshall et al. in 2015 [184] showed that different scan patterns change the maximum temperature and temperature gradient in the printed layer. Study of various scan-strategies and their effects on temperature distribution has remained as a demanded. Chessboard strategy as one of the current printing strategy splits the printing layer into identical imaginary rectangular sections called island. Previous sections presented two different patterns to scan the islands in this strategy. Tessellation scanning algorithm/strategy combines the introduced online thermography in chapter 4 with a novel-printing pattern to decrease heat accumulation, control heat-affected zones (HAZ), and generate more uniform temperature distribution in a safe range of temperature throughout the printing layer. HAZ presents a zone with an average temperature higher than a specific temperature called threshold temperature. The temperature value depends upon the printed material. Overheating leads to thermal anomalies such as balling phenomena, undesired melting, etc. in these zones. HAZ has different shapes based on the boundary conditions, thermal conditions of the layers beneath, etc. The minimum detectable size of HAZ depends on the camera resolution. However, the code may consider a bigger size as the minimum for analysis. Fig. 3.3 shows different steps in this scanning strategy.

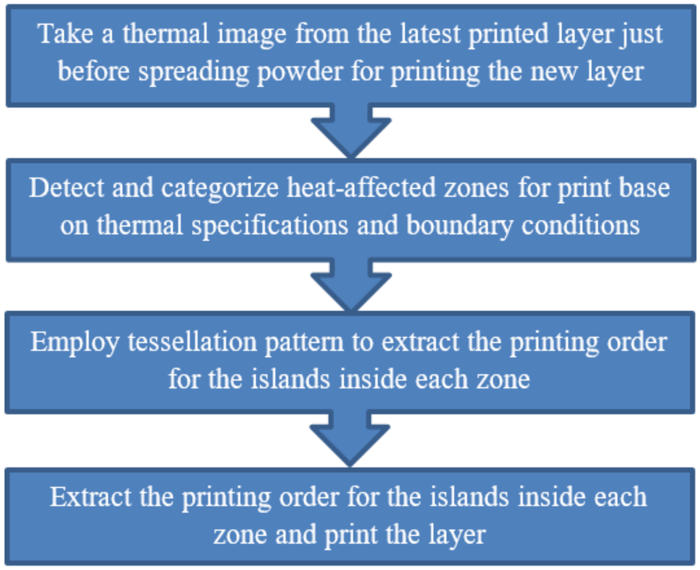

Figure 3.3. The main steps in tessellation algorithm

This printing strategy suggests the best order for printing heat-affected zones and then, the islands inside the zones, to generate the most possible uniform temperature distribution especially in the layers with a complex geometry. Selecting the order of printing for the zones is based on the thermal images and the zones specifications acquired in the proposed online thermography in chapter 4; moreover, it leverages the pre-knowledge data about the effects of boundary conditions on heat dissipation of the heat zones obtained by FEA experiments. The HAZ specifications, namely, the location of the thermal zones, the ratio of area to circumference, and the average temperature throughout the prior printed layer, acquired in thermography methodology and their boundary conditions specify the printing order of the zones. This methodology prints the zones with a lower average temperature or with boundary conditions with less heat dissipation sooner to avoid heat accumulation in the other zones and leaves more time for cooling of the printed zones. Fig. 3.4 shows the effects of different boundary conditions on temperature distribution and heat dissipation of the region exerted by a heat flux. First, the heat flux exerts on the circumference of the designed geometry in 0.1 seconds and then, it exerts on the splitting islands placed inside each heat zone from the left towards the right in 0.1 seconds each. The heat flux remains in previous islands during the exerting to the new islands. If there are different printing zones in a layer, the heat flux exerts on the very left one towards the very right one. The simulations show the following results:

1. The temperature value (especially) around the geometric center is higher and the heat dissipation is lower for a wider and larger region compared to a smaller region (no. 2, 3, 4, 5, 6).

2. Symmetrical regions, namely, the regions with symmetric shape and position of printing zones generate symmetrical temperature distribution (no. 1, 2, 4, 5, 9, 10, 11). In non-symmetrical regions, the temperature distribution follows the geometry (no. 6, 13, 16).

3. Large size heat-affected regions relative to the entire surface have significant thermal effects on the entire surface (no. 1, 2, 3); the size of the area affected by small or medium regions depends on the distances between the regions (no. 9, 10, 12). Small regions may affect just locally if the distance is far enough (no. 11).

4. Distance from the surface edges significantly affects heat dissipation. The simulations show that the heat inside the regions with farther distance to the edge, dissipate in a shorter period (no. 11, 12, 14).

5. The number and position of the regions change the temperature distribution. The temperature contours shift to that area with a higher number of regions and thus, temperature gradient increases throughout the surface (no. 7, 8).

6. Heat dissipation in narrow regions, namely, a small area with long circumference is significantly higher than wider regions (no. 13).

7. The Ratio of region area to its circumference (convex geometry versus concave geometry) affects the temperature distribution and heat dissipation. The model number 15 (convex) has the same area size as the model number 16 (concave) but the results show that the heat accumulates in the geometrical center of this convex region. The highest temperature gradient occurs between the center of the region and its circumference. In the concave region, however, the temperature distributes more throughout the region and the temperature gradient is not necessarily highest between its circumference and the geometrical center.

8. Simulations number 17 and 18 show that fabrication of couple support structures with smaller diameters is more effective on heat conductivity from printed layers to the layers beneath compared to the support structures with a bigger diameter; however, it does not affect the pattern of temperature distribution.

Tessellation algorithm leverages the aforementioned simulation results to print the heat-affected zones by following these rules:

1. Print bigger area sooner.

2. Calculate the distances between the HAZs and print the one with the farthest distance to the prior printed areas.

3. Combined small regions affect more on thermal distribution compared with the local separated ones.

4. The regions close to the edge of the printing layer take more time for heat dissipation thus, should print sooner.

5. Print the HAZs as scattered as possible. For instance, print the HAZs from opposite sides of a layer with the farthest distance is significantly preferred compared to start printing from one side and goes toward the other side of the printing layer.

6. Print wider regions sooner than narrow regions.

7. If the printing areas have the same area size, start printing with geometries with a smaller rate of circumference to the area due to more heat accumulation in these regions.

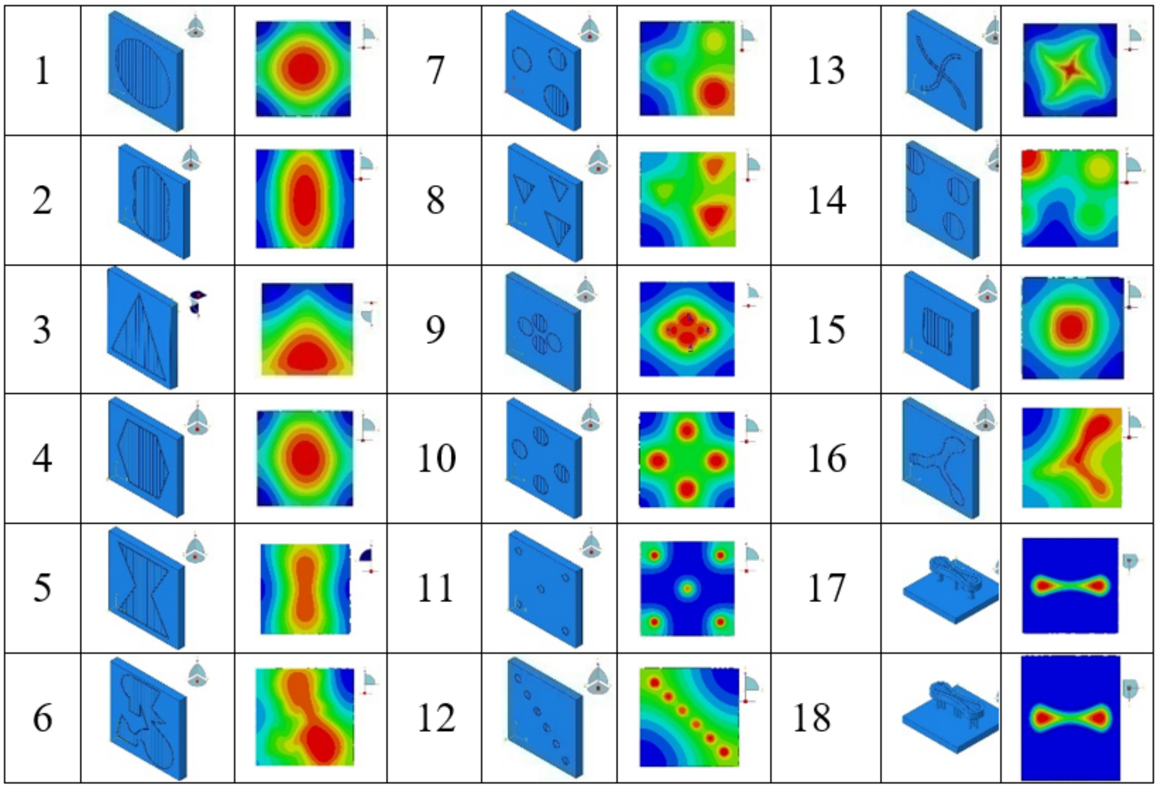

Figure 3.4. Investigate the effect of different boundary conditions on temperature distribution and heat dissipation of the zones exerted by a heat flux

Tessellation scanning pattern for optimization of islands printing order

First, Tessellation algorithm uses a thermography method to detect HAZs. Temperature distribution in each zone is almost uniform. In the next step, this algorithm employs a scanning pattern to print the islands and generate the most possible uniform temperature distribution. The most effective printing strategy is under study by employing the developed simulation technique. Previous sections studied two different possible scanning pattern, namely, rastering pattern and helical pattern. This section introduces a novel scanning pattern called a tessellation pattern, which generates a more uniform temperature distribution in the printing zone with a complex geometry. Moreover, the current machines can employ this scanning pattern to reduce warping in the layers with long dimensions or with a complex geometry by generating a more uniform temperature distribution. This pattern first splits the entire surface of a zone/layer into the imaginary islands with an identical shape such as chessboard methodology; however, the islands may possess a shape other than a rectangle in order to generate more uniform temperature distribution, better microstructure, and better bonding between the printing layers. The optimized shape is still unknown and it needs further study. This pattern starts employing hexagons to cover the entire printing layer. The next chapter will explain the reasons why this methodology chooses hexagon as the first option. The second step is to print the islands. The conception of uniform weight distribution throughout a level inspires this method how to generate more uniform temperature distribution. This pattern starts with printing the two islands with the farthest distance to each other. Then, it calculates the distance of all remained islands with the printed islands to detect the minimum distance of each island with one of the printed island. Finally, the patterns algorithm compares these minimum distances for all the remained islands and chooses the maximum one. The island with the maximum minimum distance will be the third island to print. This loop continues to select all the islands (Fig. 3.5). Hence, the printing order of the islands significantly depends upon the geometry of the printing layer.

3.1.2 Introducing a layer-based online IR thermography

Introduction

Online monitoring and control is the missing link in the automation of AM production chain to fabricate a flawless optimized product (Fig. 3.6). Monitoring and controlling of the thermal evolution of the process, as an efficient methodology, facili-

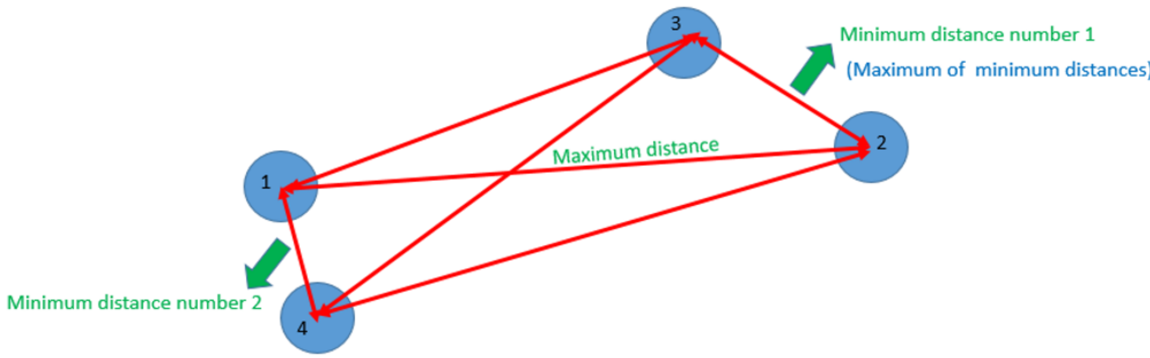

Figure 3.5. How to choose the order of printing islands inside a zone in Tessellation algorithm

tating adjusting the contributing parameters and thus, avoid or minimize the thermal anomalies. Temperature distribution throughout the layer under fabrication presents an efficient proxy to control the thermal evolution during the fabrication process [168, 183] because a non-uniform temperature distribution is a major source of some prevalent thermal abnormalities in thermal inherent AM processes such as FDM and powder-bed fusion process. This chapter introduces a novel IR thermography for these processes. The objective is to evaluate thermal evolution, temperature distribution, and detect macro scale HAZs and their specifications layer by layer real-time (during deposition of the new layer) throughout the entire bed area of fabrication process instead of current strategies of tracking micro scale melt pool specifications employed in SLM process. This monitoring strategy is capable to implement in current powder-bed fusion printing machine to modify the scan pattern by the control strategy in our future research works.

Research works and challenges

Our literature review in chapter 2 shows that a significant portion of the defects depicted in Fig. 2.1 roots in thermal characteristics of the process. Scholars are in

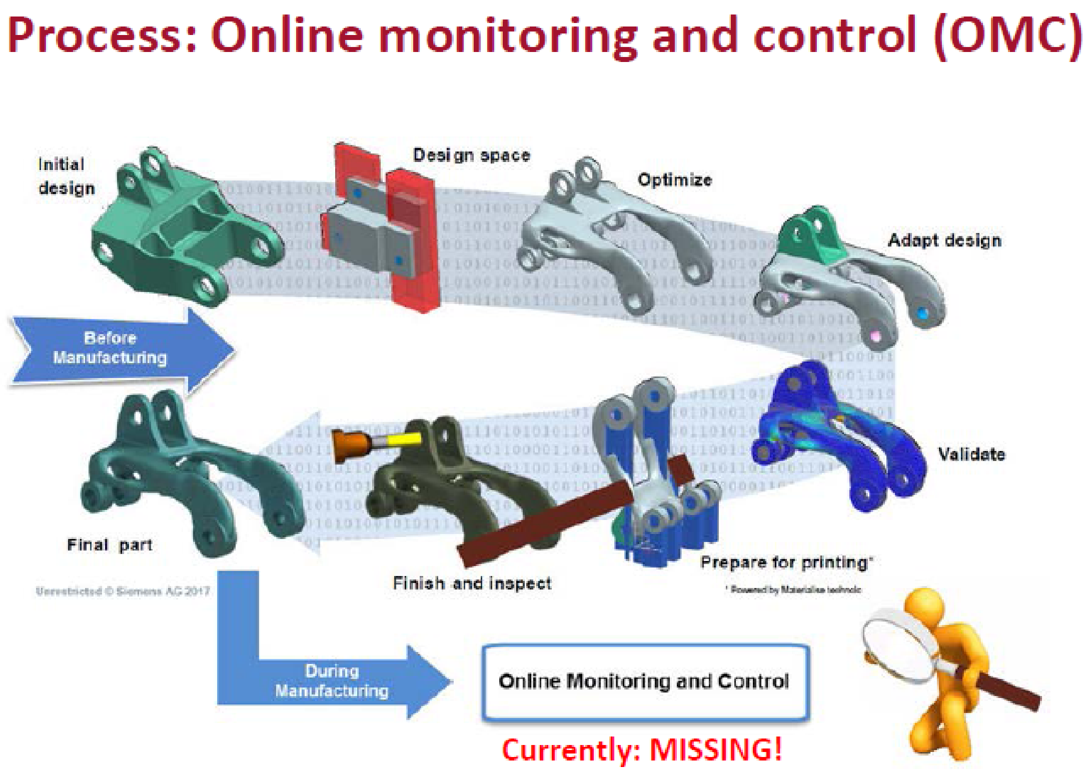

Figure 3.6. Design and optimization chain in AM

agreement with controlling of thermal evolution as the main source of avoiding the thermal anomalies. Inhomogeneous temperature distribution throughout the layer under fabrication creates inhomogeneous shrinkage, warpage, in-build curling, and poor repeatability of part properties in the SLS process [167]. Few scholars put efforts on formulating the process to be able to optimize process parameters based on some predictive equations. Carslaw and Jaeger [185] utilized Fourier heat conduction theory (Eq. 3.1), as the most common equation, to describe the governing heat conduction with the initial temperature and boundary conditions, presented in Eq. 3.2, Eq. 3.3, and Eq. 3.4 respectively. [16]

$$\lambda\left(\frac{\partial^2 T}{\partial^2 X}+\frac{\partial^2 T}{\partial^2 Y}+\frac{\partial^2 T}{\partial^2 Z}\right)+q=\rho c\frac{\partial T}{\partial t} \tag{3.1}$$

$$T(x,y,z)=T_0 \tag{3.2}$$

Surface convection and radiation is:

$$-\lambda\frac{\partial T}{\partial z}=\varepsilon_\theta\sigma(T^4-{T_\theta}^4)+h(T-T_\theta) \tag{3.3}$$

There is no heat loss at the bottom.

$$-\lambda\frac{\partial T}{\partial z}\bigg|_{z=0}=0 \tag{3.4}$$

Where λ is the conductivity coefficient, q the internal heat, ε_θ the thermal radiation coefficient, σ the Stefan-Boltzmann constant. This model does not consider the liquid flow in the melt pool, the shrinkage of the powders, and the laser beam characteristics, namely, diameter, power, and intensity distribution. However, scholars made efforts in other studies to include the factors [186], none of these efforts could reveal neither thoroughly and precisely the process because of its complex nature, complex or non-realistic boundary conditions, and variation of powders thermal characteristics during the process nor an analytical solution to completely satisfy the equations. However, there are some solutions associated with the simplified model [187], the solutions cannot cover the temperature distribution through the whole layer. For instance, the three dimensional Rosenthals point model temperature distribution for a point and line heat source [16] using a steady state on the surface of a semi-infinite plate along the x-axis (Eq. 3.5) [188].

$$\bar{T}=\frac{e^{-(\bar{x}_0+\sqrt{\bar{x}_0^2+\bar{y}_0^2+\bar{z}_0^2})}}{2\sqrt{\bar{x}_0^2+\bar{y}_0^2+\bar{z}_0^2}} \tag{3.5}$$

Where

$$\bar{T} = \frac{T - T_0}{\left(\dfrac{\alpha Q}{\pi k}\right)\left(\dfrac{\rho c V}{2k}\right)}, \bar{x}_0 = \frac{x_0}{2k/\rho c V'}, \bar{y}_0 = \frac{y_0}{2k/\rho c V'}, \bar{z}_0 = \frac{z_0}{2k/\rho c V'} \tag{3.6}$$

Therefore, employment of analytical approach for controlling the process is not practical yet due to the lack of precise model and accurate solution. Finite element analysis has been another approach for modeling the process. This approach, however, reveals a good vision about the thermal evolution during the process, cannot employ it real-time due to the enormous time of analysis. Numerous studies for thermography in powder-bed fusion processes shows the capability of online monitoring, namely, real-time thermography, as a powerful alternative for the analytical approach and finite element analysis. Employment of this approach does not need to a deep knowledge about the nature of the process, precisely reveals the temperature distribution through the whole layer, and it is possible to quickly get feedback to adjust the parameters in situ during the fabrication process. However, there are various gaps, limitations, and challenges to be able to commercialize this approach. Traditional monitoring approaches predominantly applied to the study of melt-pool characteristics in the SLM process and their effect on ultimate part quality such as microstructure, mechanical properties, shrinkage, etc. [184]. Numerous literature investigated monitoring the thermal behavior of the process real-time. This section reveals a number of efforts, the achievements, and the challenges in following. In one effort Chivel and Smurov in 2010 measured the important thermal parameters in powder-bed fusion process such as maximum surface temperature, the temperature distribution in the processing area, temperature value versus laser power, and size of the melt pool [161]. This work developed an on-line temperature monitoring systems in order to measure the spatial distribution of brightness temperature at two wavelengths and selected temperature profiles, calculation of color temperature and maximum temperature in the focal spot, and measure the deviations of the maximum temperature from its optimal value. According to the study by Everton et al. in 2016, currently, some AM machine manufacturers offer additional modules for in-situ monitoring of powder-bed fusion process which can be added onto the basic AM machine, although in many cases, the data generated is stored but not analyzed in real-time for closed-loop feedback. The early work predominantly concentrated on monitoring of the melt pool using in-line cameras, in combination with photodiodes and some closed-loop control of melt pool temperature. Laser power is the only process parameter altered in these cases. For instances, S. Berumen et al. in 2010 developed a thermal monitoring mounted a high speed camera to measure the dimensions of the melt pool and a photodiode to measure the mean radiation emitted [133]. Closed-loop feedback could help to stabilize the melt-pool and keep the temperatures within a pre-defined window to reduce overmelted zones and resulting gas pores [189]. One challenge for using digital cameras to monitor the melt pool is the need of a continuous stream of images and the necessity for image processing and developing tailored algorithms and software to fulfill their specific needs in order to be able to capture useful information [135, 190-192]. Moreover, the electron beam powder-bed fusion process frequently employs in-situ thermal monitoring and control, as this process is inherently a thermal process as well. Schwerdtfeger et al. equipped their machine with a FLIR Systems A320 IR camera [193]. The thermal images taken after melting indicates the material flaws because of higher heat radiation correspond to the flaws; moreover, it shows the transfer of flaws from layer to layer. Price et al. at the used a similar system to determine the repeatability of temperature measurements, build height effect on temperature profiles, transmission losses due to metallization of sacrificial glass, molten pool emissivity, molten pool dimensions and overhanging structure thermal effects [165]. Rodriguez et al. incorporated an IR camera into an ArcamA2 electron beam-PBF machine in order to analyses surface temperature profiles for each build layer and a limited investigation of the thermal effect of the printed intersections of cylindrical rods on each other [166]. Mireles et al. also set out to develop an automated feedback control method to maintain uniform build temperatures [194]. Parameter changes implemented to stabilize temperature resulted in part porosity. Some build failure happened due to the high memory consumption of image processing and some communication delays. This is not the only challenge that scholar encountered with. According to literature, there are a number of challenges to implementing a practical real-time thermal monitoring and control system for the laser sintering process. First, recognition of thermal defects, their contributing parameters, and the causal effects between the parameters and the defects. Second, incomplete thermal data acquisition from all the thermal aspects of the process. Third, lack of methodologies and software to capture, analyze data, and feedback to the control system. Forth, real-time adjustment of process parameters. Fifth, poor spatial resolution and limited fields of view for thermography with using IR camera. Sixth, macro-scale monitoring of thermal evolution of the process (especially in SLS) instead of focusing on micro-scale monitoring of melt-pool (especially in SLM) to overcome some current most frequent thermal fabrication challenges such as distortion, warpage, heterogeneous microstructure, etc. and finally, access to an open-source software to implement the designed closed-loop control methodology and adjust the process parameters real-time.

Experimental Setup and design of experiments

Camera specifications

This project employs a FLIR Research IR Camera (A325sc) (Fig. 3.7) with the resolution of 320 240 LWIR and fast data transfer up to 60 Hz to monitor the thermal evolution of the process online and extract the necessary thermal data from the fabrication process layer by layer.

Table 3.1 shows the camera specifications. According to the spectral range, this camera can just monitor the process, which uses fiber laser.

Figure 3.7. The experimental setup for IR thermography of FDM process

Table 3.1.
The camera specifications

Specification	Explanation
Detector Type	Uncooled Microbolometer
Mounting	1/4”-20 (on 3 sides), 2 $\times$ M4 (on 3 sides)
Spectral Range	7.5 13.0 µm
Size [L $\times$ W $\times$ H] w Lens	170 $\times$ 70 $\times$ 70 mm (6.7 $\times$ 2.8 $\times$ 2.8 in)
Operating Temperature Range	-15°C to 50°C (5°F to 122°F)
Customized Temperature Range	-20°C up to 2,000°C (3,632°F)
Weight [incl lens]	0.7 kg (1.54 lb)
Accuracy	±2°C or 2% of Reading
Power	12/24 VDC, 24 W Absolute Max.
Accessories	2 cables (1 for connecting to PC & 1 for power)

Mounting angle

According to the FLIR research users guide [195], the glass reflectance, accordingly, cameras viewing angle does not change much up to an angle of about 45° relative to normal incidence (Fig. 3.8). However, the closer viewing angle to the normal of the powder bed, the more accurate dimensions the camera records. The dimensions of the features are important for the future phases of the project. There are three options for mounting the camera. The best position is on top of the roof of the chamber. Most of the sintering machines have some holes which covered by a lid. It is possible to fabricate an intermediary support to mount the camera on one of these holes. A ZincSelenide (Zn-Se) window covers the hole to protect the equipment from metallization. The hole with an angle closer to the powder-bed normal (closer to the laser scan head) is preferred (Fig. 3.9). In this position, the camera places out of the chamber, and thus there is no concern about the effect of chamber temperature on camera and the placement of the cables. The alternative option is to mount the camera inside the chamber if either it provides a better viewing angle or there is no hole in the roof. In this case, a box should isolate the camera from the internal temperature of the chamber. The last position to mount the camera is outside of the chamber. In this case, an intermediary part with Zinc-Selenide (Zn-Se) glass will replace the glass of the machines viewing window (Fig. 3.10).

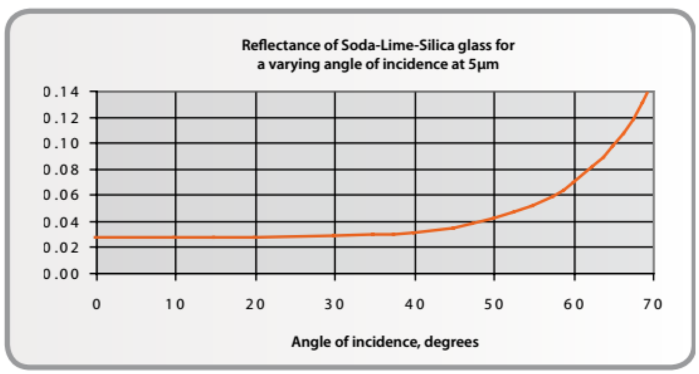

Figure 3.8. Glass reflectance as a function of camera viewing angle relative to normal incidence

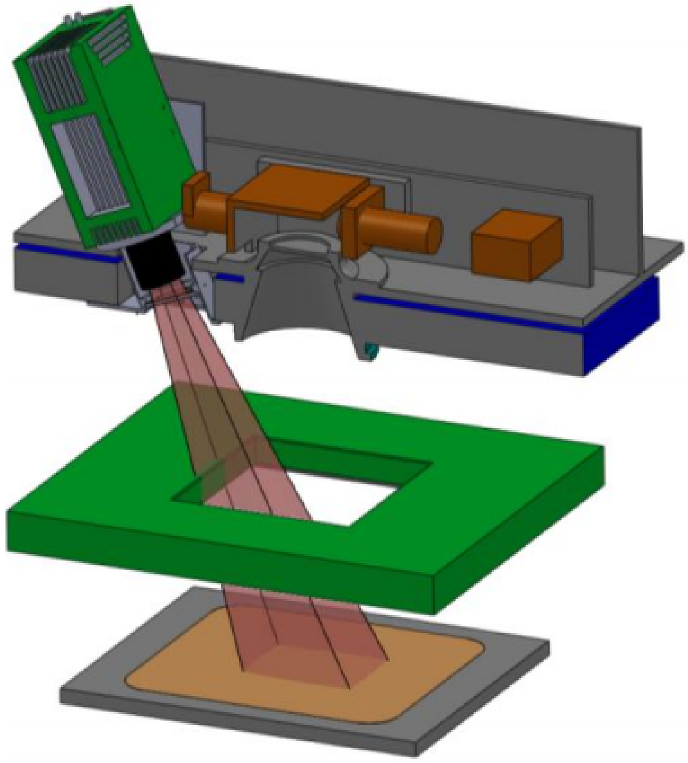

Figure 3.9. The placement of the camera on top of the chamber close to the scan head

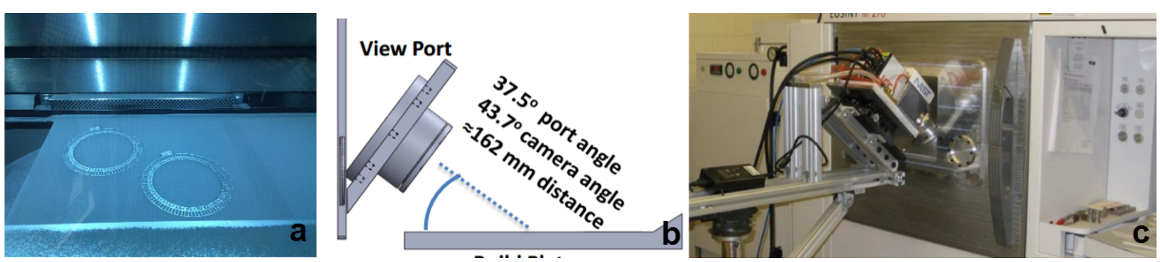

Figure 3.10. a. a view from the printed part from outside of the chamber; b. the intermediary part; c. the IR camera pointed to the powder-bed from outside of the chamber

3.1.3 Evaluate the thermal evolution of AM thermal processes

Introduction

While current AM machine tools are greatly improved from early versions, many of the same problems identified by early researchers in the 1980s persist [196]. Some of these defects directly have root in thermal characteristics and the temperature distribution of deposited layers. Warping and curling, for instances, are significantly dependent on the thermal interaction between the current layer and the layers fabricated earlier. These aspects of FDM process, suggest monitoring of the temperature distribution and thermal evolution of parts during deposition of layers, as a key towards a better understanding of the process. Numerous research efforts that address the monitoring and control of additive manufacturing (AM) processes to improve part quality. FDM is inherently a thermal process and thus, lends itself to being study by thermography. In this section, we applied the image-based thermography layer by layer with the usage of an infrared camera to investigate the thermal behavior and thermal evolution of the FDM process for the standard samples printed by ABS filament. This methodology employs the combination of the layer based temperature profile plot and the temporal plot to understand the temperature distribution and average temperature through the layers under fabrication. This information provides insights for potential modification of the scan strategy and optimization of process parameters based on the thermal evolution. In addition, this approach for monitoring the process will allow manufacturers to build, qualify, and certify parts with greater throughput and accelerate the proliferation of products into high-quality applications [147, 197]. We select the ASTM tensile strength test standard part (ASTM D638) (Fig. 3.11). Twenty-seven different specimens were printed and monitored. Table 3.2 shows the range of three printing process parameters, namely, nozzle temperature, printing speed, and print orientation to perform the experiments [198].

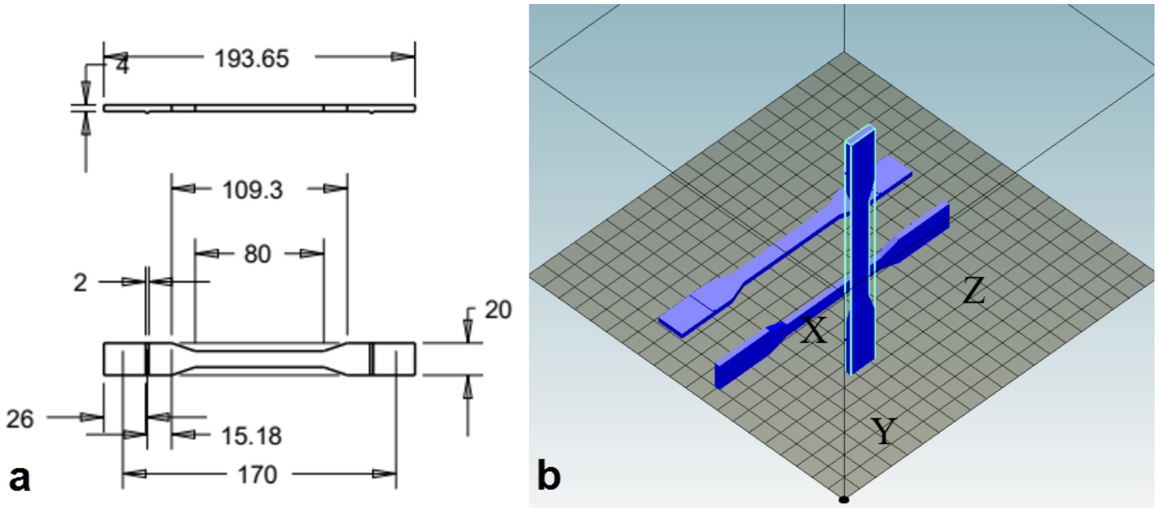

Figure 3.11. The modified ASTM tensile strength specimen used for printing; b. X, Y, and Z build orientation used in the fabrication of the specimens

Table 3.2.
Printing parameters adjusted for fabrication process of specimen S1-S27

Printing parameters	**Parameters values**		
Nozzle temperature in °C	215	225	235
Printing speed in mm/s	20	40	60

Introducing research IR max software

The Research IR Max software graphical user interface (GUI) is utilized for the in-situ monitoring of the fabrication process. Fig. 3.12 shows the main features of this software.

The software utilizes two different plots to depict the thermal data of the printing layers. First, the temperature profile plot, which shows the average temperature in the column of pixels in the monitored region of interest (ROI) (Fig. 3.13.a). Second, temporal plot, which provides the part build average temperature distributed across the layer surface with respect to printing time (Fig. 3.13.b).

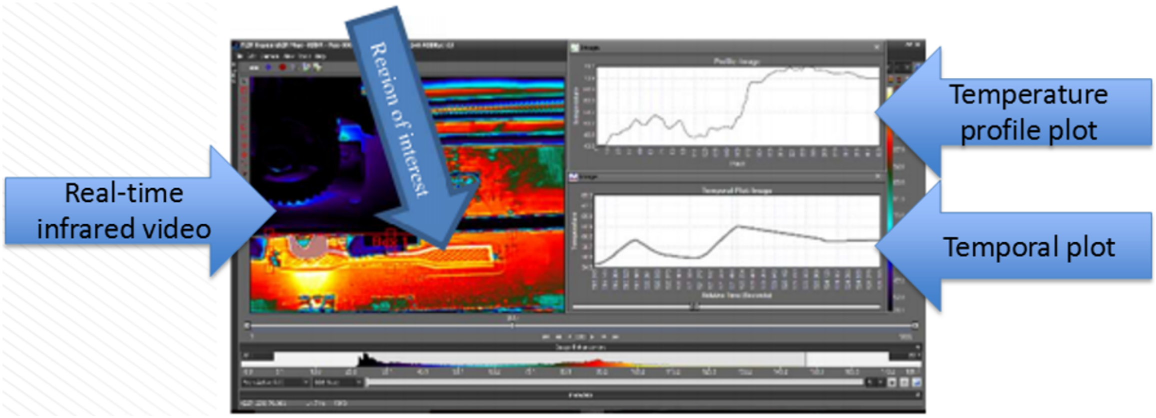

Figure 3.12. The Research IR Max software GUI to measure the thermal evolution of the fabrication process

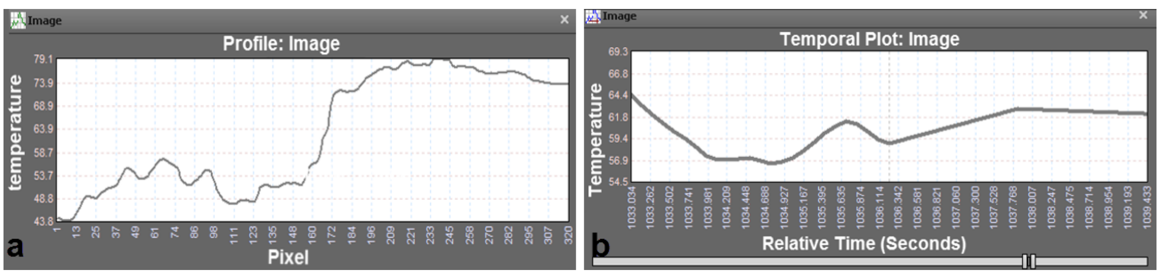

Figure 3.13. a. An example of a temperature profile plot; b. an example of a temporal plot

Analysis of thermal evolution by temperature profile plot

The monitoring methodology observes three plot trends (Fig. 3.14) during printing of a layer. The profile trends depend on the starting point of the printer nozzle, the printed direction of the previous layer, and the pattern followed in the material deposition. The plot is initially high and then it gradually decreases if the printing pattern starts depositing the layer from the geometric origin of the layer and continues printing the layer along the length of specimen toward the geometric endpoint of the layer (Fig. 3.14.a). On the contrary, the plot is initially low and then it gradually increases if the printing pattern starts depositing the layer from the geometric endpoint toward the geometric origin(Fig. 3.14.b). The third trend shows initially a high magnitude; although gradually reduces, begins again to gradually increases in magnitude. This occurs in two statuses. First, when the scanning pattern starts from either geometric origin or endpoint, continues to a point along the specimen, skips to the opposite end, and begins to deposit material while returning to the skip-point. We also observe this trend in the temperature profile plot during the printing of the first or last number of layers in Y-orientation. As Fig. 2.2.c shows, in these layers the printing cross-sectional areas exist just on the left and right-hand side of the layers and thus, the temperature of the middle of the layers falls down. This printing strategy repeats the profile trend during fabrication of successive layers. Same technique interprets the thermal evolution of different scanning patterns for fabrication of layers with different geometries for the powder-bed fusion process. In general, these trends show that a significant temperature gradient happens if the printer employs simple rastering pattern, namely, start printing from a side of the fabrication layer towards the other side. This provides the insight that the tessellation algorithm helps to generate more uniform temperature distribution.

Analysis of thermal evolution by temporal plot

As previous sections already mentioned, the temporal plot provides information on the temperature distribution of the layer under fabrication with respect to time elapsed. The nature of the generated plot interprets the thermal evolution and temperature uniformity of the part under fabrication. For instance, the temporal plots for the specimens printed in Z, X, and Y-axis orientation show the highest increase in the average temperature (heat accumulation) from beginning to the end of process respectively (Table 3.3). Our observation shows the time elapsed between the deposition of layers, the size of the cross-section, the nozzle temperature, and the number

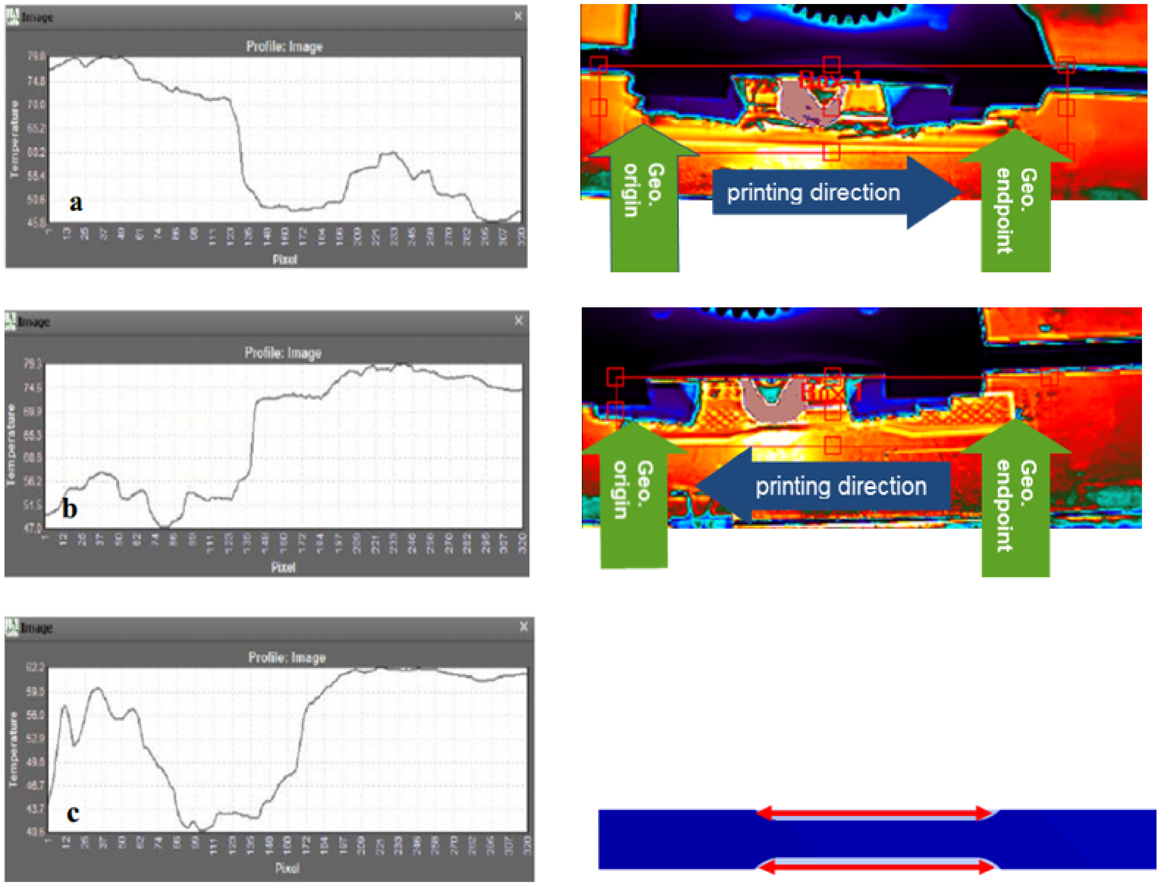

Figure 3.14. a, b, and c; Generic plot trends observed during the monitoring process of printing the specimen

of layers affect the average temperature of the fabrication process. Same monitoring technique should help the control strategy in the powder-bed fusion process to decrease the temperature gradient between layers, which is a contributing parameter for warpage, by controlling the average temperature of the fabricated layers. This is possible by controlling of process parameters such as laser power, scan speed, and scanning pattern.

Table 3.3.
Increase in average temperature of fabricated specimens in different printing orientations

Printing orientation	**Total No. of layers**	**Increases in Average Temp.**
X-axis orientation	35	5.8 °C (59.8 °C in 1^st to 65.6 °C in last)
Y-axis orientation	59	4.4 °C (54.9 °C in 1^st to 59.3 °C in last)
Z-axis orientation	1256	8 °C (48.2 °C in 1^st to 56.2 °C in last)

3.1.4 Detection of HAZs and extract their specifications

The first step is to monitor the temperature distribution through the powder-bed (Fig. 3.15.a [167]) and the layer under fabrication (Fig. 3.15.b [15]) real-time. Scholars employed various methods for online thermography that mentioned in the previous sections, however, interest in the employment of IR thermography is significantly arising. This approach is more accurate, does not need to touch the part under fabrication such as pyrometer to measure the temperature, and it measures the temperature in a wider area compared with pyrometers or the combination of CMOS camera and photodiode. Furthermore, IR thermography makes possible to acquire thermal data real-time, measure the temperature of each pixel simultaneously, collecting geometrical data of the layer under fabrication for future phases of the project, and access to a software interface with capabilities for further real-time thermal analysis.

Wegner and G. Witt in 2011 [167] utilized an InfraTec Jade III MWIR to measure the temperature distribution in a powder bed surface in different built heights in the sintering process. Krauss et al. in 2012 [168], investigated the possibility of monitoring the SLM process at the level of the heat-affected zone. They categorized the heat-affected zone for a typical scan strategy to investigate the process and material irregularities close to overhanging structures or part contours. Price et al. in a study in 2013 [165] showed the significance of overhang zones monitoring during the powder-bed fusion process. They showed that the melting of the first layer over

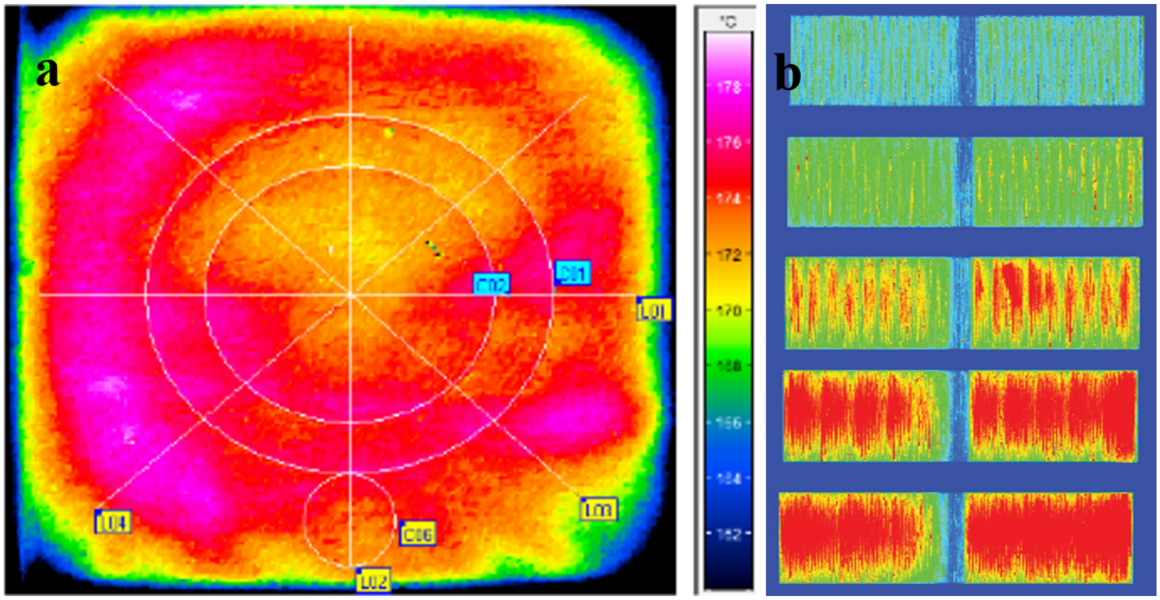

Figure 3.15. a. Measure the uniformity of temperature distribution in the powder-bed of a sintering machine; b. temperature distribution and overheating zones in overhang layers with different support structure conditions.

a powder substrate significantly decreases the cooling rate compared to cooling over a solid substrate. Printing more layers diminishes this effect completely after the third layer above the powder substrate. This work employs the combination of FLIR IR camera interfaced with the Research IR Max software, with MATLAB coding to make a smarter measurement planning methods. This method monitors temperature distribution throughout the layer under fabrication, overhang zones, with or without support structures, and HAZs, namely, the zones with a temperature above a specific value (threshold temperature). This method helps to study the thermal effects of these zones on each other. This methodology first takes a thermal image from these items just before spreading the powder for the fabrication of the new layer. Then, it acquires the thermal data, saves it automatically, and sends it for using in the designed analytical algorithms, as the main operations in the monitoring phase. The methodology repeats these steps layer by layer. Understanding of thermal evolution by obtaining the temporal plot and temperature profile trend, real-time, are the other operations in this task. The previous section explains this task thoroughly. The monitoring methodology sends the analyzed data to control system to adjust the desired parameters. To analyze the acquired data, the developed code in MATLAB for online IR thermography first extracts an ASCII file automatically in every couple of frames (Fig. 3.16) and in the second step, it calculates the ratio of temperature uniformity and the average temperature for each fabricated layer. Measuring the uniformity of temperature distribution in each layer is a crucial thermal characteristic because the control system needs to minimize the temperature gradient, through the layers under fabrication and between the fabricated layers. This can avoid sever thermal tensions, make the microstructure homogeneous, and prevent thermal anomalies. Yang et al. [199] introduced a ratio named Ru, that is calculated by the Eq. 3.7, for measuring the temperature uniformity where T and T represent the local temperature and average temperature, respectively.

$$R_u = \left(\sum \left(\frac{T - \bar{T}}{\bar{T}} \right)^2 \right)^{1/2} \tag{3.7}$$

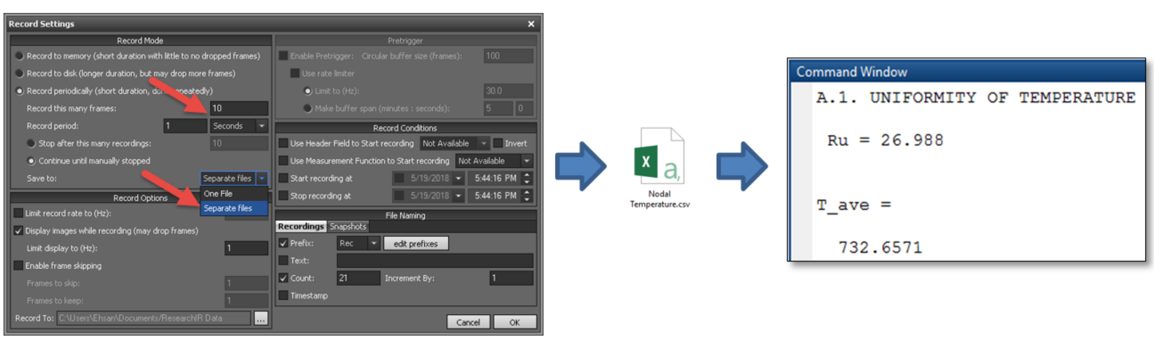

Figure 3.16. The settings in IRMax research software to collect the thermal data automatically

In the third step, this code employs image segmentation algorithm to detect heat-affected zones, measure the geometrical center of each zone (see Fig. 3.17 as an example) as well as the distance between zones and finally, their area and circumference. To detect HAZ the IR-Max software applies a thermal filter, called palette, to the acquired thermal image (see Fig. 3.18.a as an example)to generate a bicolor thermal image. This image shows the HAZs, whose temperature is equal to or above the threshold temperature with a different color (Fig. 3.18.b). Image segmentation algorithm detects the HAZs using thresholding (Fig. 3.18.c). The code saves the allocated pixels to each zone to measure the geometrical center, area, circumferences, and the distance of each zone with respect to each other. This methodology monitored the thermal evolution (previous section), temperature distribution, and HAZs of some fabricated samples in the FDM process (Fig. 3.18) to test the algorithm. Fig. 3.18 shows the results for one layer.

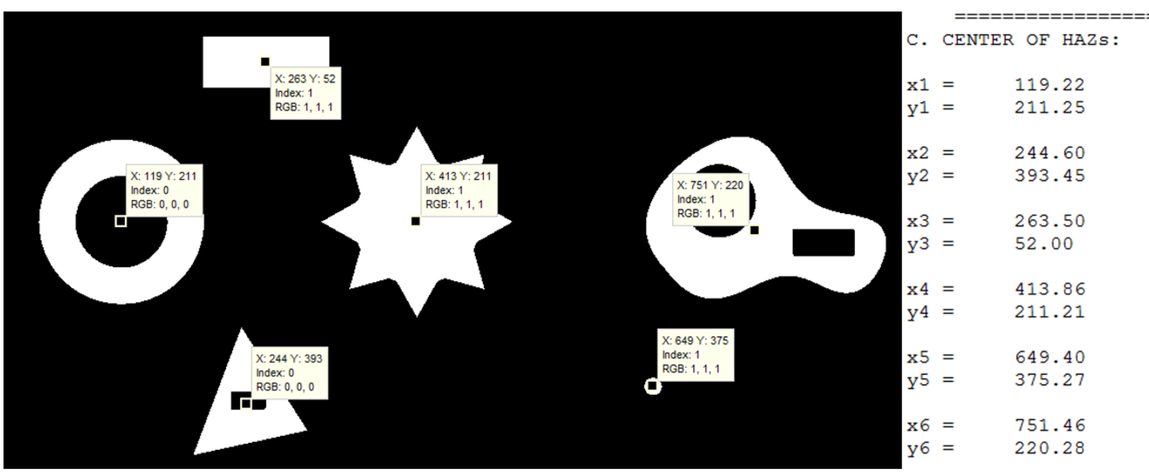

Figure 3.17. Measuring the geometrical center of random shapes with the MATLAB code

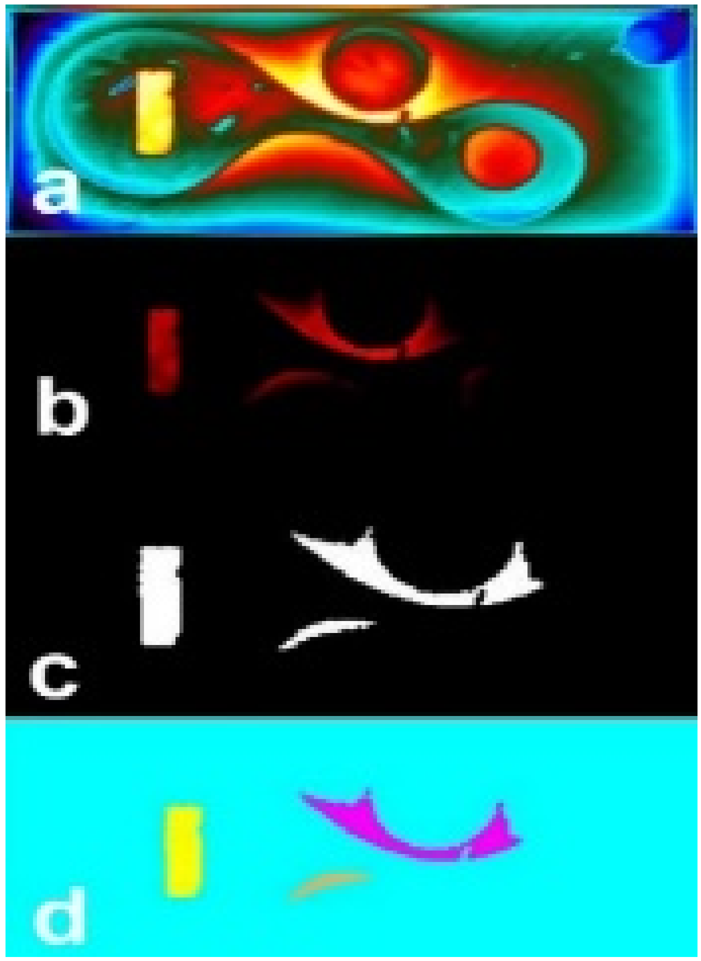

Figure 3.18. a. the acquired IR image; b. bicolor IR image, which shows HAZ; c, d. HAZs detected and classified by the segmentation algorithm

4. DEVELOP A NEW TECHNIQUE TO SIMULATE TEMPERATURE DISTRIBUTION IN THE POWDER-BED FUSION PROCESS

4.1 Introduction

Complex nature of powder-bed fusion process precludes any mathematical modeling to explain the process precisely. Consequently, numerous literature attempt to employ finite element analysis to simulate powder-bed fusion process; however, all the recommended approach are a very time-consuming process and thus, it is not practical to simulate temperature distribution for more than couple tracks in one printing layer. This chapter introduces a new technique to approximate the temperature distribution in any printing layer with a complex freeform geometry in a fraction of time. This technique assists designers to predict the temperature distribution in any printing layer of their designed component and thus, modify the design to generate more uniform temperature distribution and reduce thermal stress. Furthermore, it facilitates testing of different scan strategies for scholars with expenses of no physical experiments to help them approximate the effect of their novel scan strategies, namely, changing in laser specifications and scan pattern on temperature distribution and the temperature value of a fabricated layer.

4.2 Simulation of temperature distribution in one island

Current 3D printer machines in powder-bed fusion process employ two different scan strategies to exert the laser beam on the printing layer. First, employment of rastering pattern throughout the layer in which laser beam sweeps the entire printing layer in a simple back and forth movement (Fig. 4.1.a). The second strategy employs chessboard or island scanning pattern (Fig. 4.1.b) in which some identical rectangle, called islands, split the entire printing layer and the galvanometer exerts the laser beam on each island in rastering pattern. Second scanning pattern consumes more time to print each layer however it generates more uniform temperature distribution in complex geometry or in the layer with a large area size. The introduced simulation technique in our work employs the second scan pattern to approximate the temperature distribution for the complex geometries. The first step is to run finite element thermal analysis for one printing island. The previous literature shows that employment of hexagon islands improves microstructure and bonding between layers in the printed artifact by removing the discontinuity and gaps between the printing layers. Furthermore, the topology of a hexagon in natural structures manifests the concept of uniformity, they can fit together perfectly to cover an area without any gap, and the shape is closer to the shape of a circle which poses the most symmetrical geometry and boundary conditions to generate the most uniform temperature distribution. Hence, this technique employs hexagonal islands to cover a layer and simulate the thermal history of a single hexagonal island in ABAQUS to generate more uniform temperature distribution. Furthermore, employment of hexagonal islands is the base for the tessellation algorithm, which will be introduced later in future sections. The laser scans the island with the rastering pattern. This technique may employ the islands with different geometries to study their effects on the temperature distribution of the printing layer in the future works.

4.2.1 Selected parameters for simulation in ABAQUS

The high power laser in the sintering/melting process generates a significant temperature gradient between the laser spot and the adjacent area. This leads to a high cooling rate and thus, this technique employs transient thermal analysis to simulate the temperature distribution of a printed island with Ti-6Al-4V, which is a prevalent material in the powder-bed fusion process. This technique makes the following

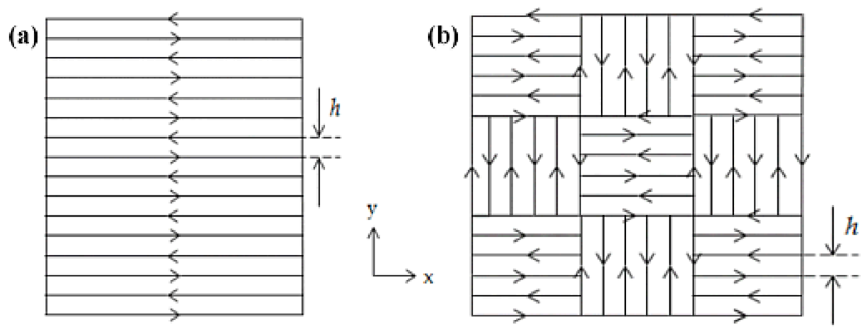

Figure 4.1. a. Simple rastering scan strategy and b. Chessboard or island scan strategy [200]

assumptions to simplify the simulation process and decrease the analysis time: first, this technique exerts a uniform heat flux to simulate the laser spot exerted on the printing island instead of the real Gaussian distribution of heat flux in the fiber laser (Fig. 4.3). Second, the laser exerts its power in a square shape instead of a circular shape. This assumption is because a moving circular spot of a laser makes a rectangular laser track, which consists of consecutive square shapes. These laser tracks fit together to cover the entire island and avoid the complexity of using DFLUX subroutine in ABAQUS to simulate the laser movement. As Fig. 4.2.a shows, this approach exerts a uniform heat flux on the consecutive square zones in each simulation step respectively. This technique has simulated a short track of laser first with different laser beam diameter, different scan speed, and different laser power in ranges recommended in current machines manual and literature. For instance, EOS machines manual [201] suggests the laser beam diameter between 100 and 500 µm and the scan speed between 40 and 500 mm/s. The criteria to select optimized parameters are to achieve a resulted temperature value close to the sintering temperature of the selected material, manifest more smooth temperature distribution, and a minimum number of tracks to cover the entire island. For instance, Fig. 4.2 compares the effect of laser beam diameter on the simulation of temperature distribution between the selected diameter (300 µm) and a bigger one.

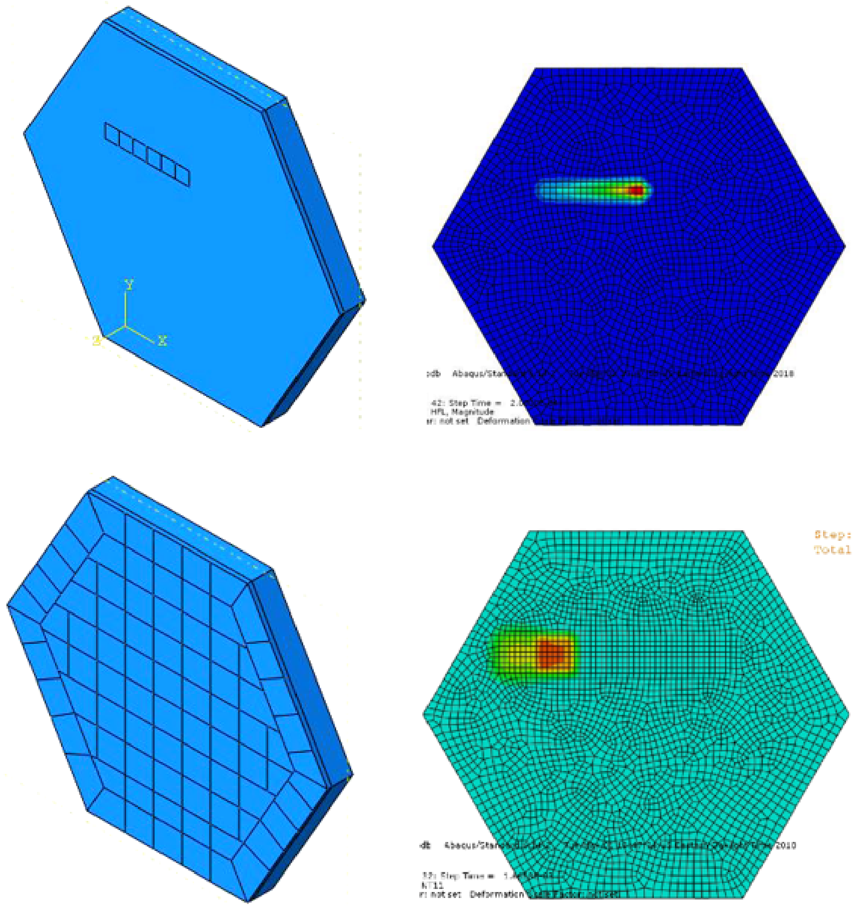

Figure 4.2. Comparing the effect of bigger laser beam diameter with smaller one on simulation of temperature distribution in a single zone

The total heat flux exerted by a laser equals to [202]:

$$q(r) = \frac{2P}{\pi {r_0}^2} \exp\left(- \frac{2r}{{r_0}^2} \right) = \frac{2 \times 100}{\pi \times 0.15^2} \exp\left(- \frac{2r}{0.15^2} \right) \tag{4.1}$$

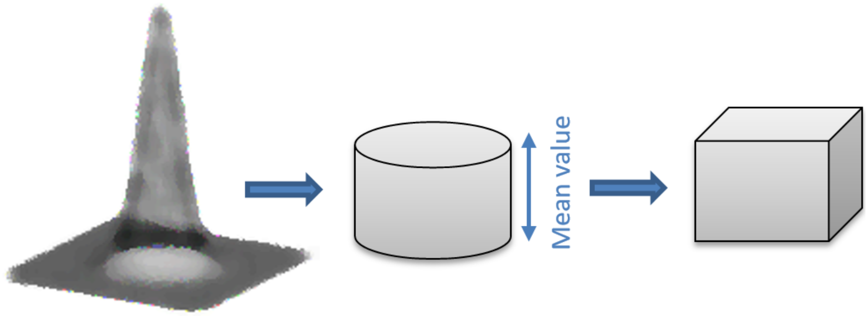

Figure 4.3. Uniform heat flux approximates the Gaussian distribution one exerted by the laser on a square spot

In which, P is the laser power, r_0 is the laser beam radius, and r is the radial distance of a point from the center. The exponential term shows the Gaussian distribution of the laser heat flux. Mean value equals to:

$$
\begin{gathered}
V = \int dv = \int_0^{r_0} \int_0^{\frac{2P}{\pi {r_0}^2}} \int_0^{2\pi} r d\theta dz dr = \pi {r_0}^2 \times q_{mean} \\
8650 = \pi {r_0}^2 \times q_{mean} \Longrightarrow q_{mean} = 1223724.7 \, \frac{mW}{mm^2}
\end{gathered}
\tag{4.2}
$$

Fig. 4.4 shows some material specifications, namely, specific heat and conductivity, which change during the process because they depend upon the temperature [203]. This technique uses a temperature-dependent data option to define these material properties. ABAQUS analyzes the model by Standard/Explicit Model and employs SI units (N, mm, Tonne, S, K). Table 4.1 shows the summary of all the other simulation parameters.

Table 4.1.
Selected process parameters to simulate the temperature distribution of a printed island

No.	Simulation parameter	Value	Unit	Explanation
1	Laser beam diameter	0.3	mm	-
2	Edge of laser spot area	0.266	mm	Square shape approximates the laser spot area
3	Scan speed	100	mm/s	-
4	Elapsed time to pass a laser spot	0.0002	sec	Time to pass one square; step time in ABAQUS
5	Initial increment step size	0.0001	sec	-
6	Laser power	100	watt	-
7	Exerted heat flux	1223724.7	mw/mm^2	-
8	Hatch space	0.3	mm	Equal to the laser beam diameter
9	Cooling time	0.001	sec	The last step time with no exerted laser
10	Layer thickness	0.08	mm	-
11	Total model height	0.48	mm	1 layer of powder and 5 printed (solid) layers
12	Primary temperature	773.15	K	Predefined field uses the nodal set; just solid layers
13	Film coefficient [204]	0.05		Convection in all steps in 363.15 K; top surface
14	Approximate global mesh size	0.1		-
15	Element type			-

4.2.2 Model specification

The previous section shows all the necessary parameters to simulate a model of printing zone called an island. The model top surface consists of all the square zones (laser spots) set together to cover the entire surface (Fig. 4.5.a). The optimized size for the island is the maximum possible size that generates uniform temperature distribution after exerting the laser. This study selects the dimensions according to the observation from the chessboard scanning strategy in industrial experiments, which shows in Fig. 4.5.b; however, future research may study more to find if there is an optimized size. These dimensions generate uniform temperature distribution

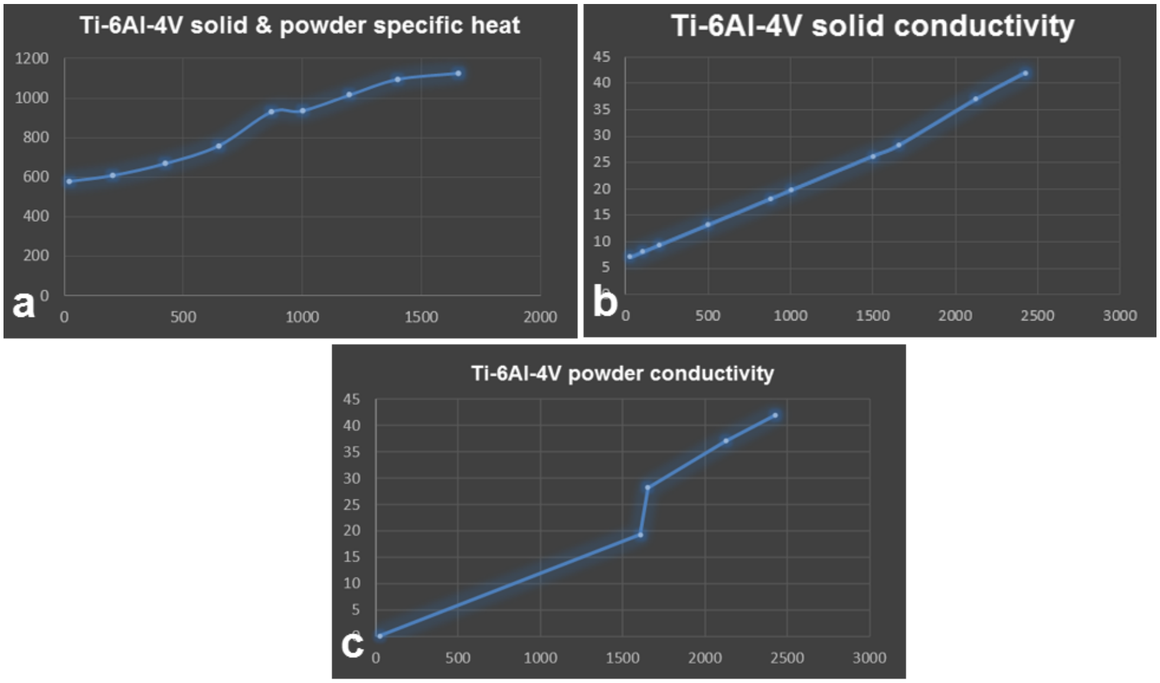

Figure 4.4. a. Solid and powder specific heat; b. Solid conductivity; c. Powder conductivity

after printing the island. The total number of steps to simulate this model is 317, which includes 316 square zones and the last step is the cooling step by exerting no laser. Fig. 4.5.a shows the first printing zone and the last one. The laser prints the circumference zones first (red path) and then, starts from zone A to print inside of the island, continues in rastering pattern to reach to zone B (orange path). The model modifies some of the square shapes to generate less distorted meshes and facilitate simulation. Fig. 4.6 shows the meshing structure.

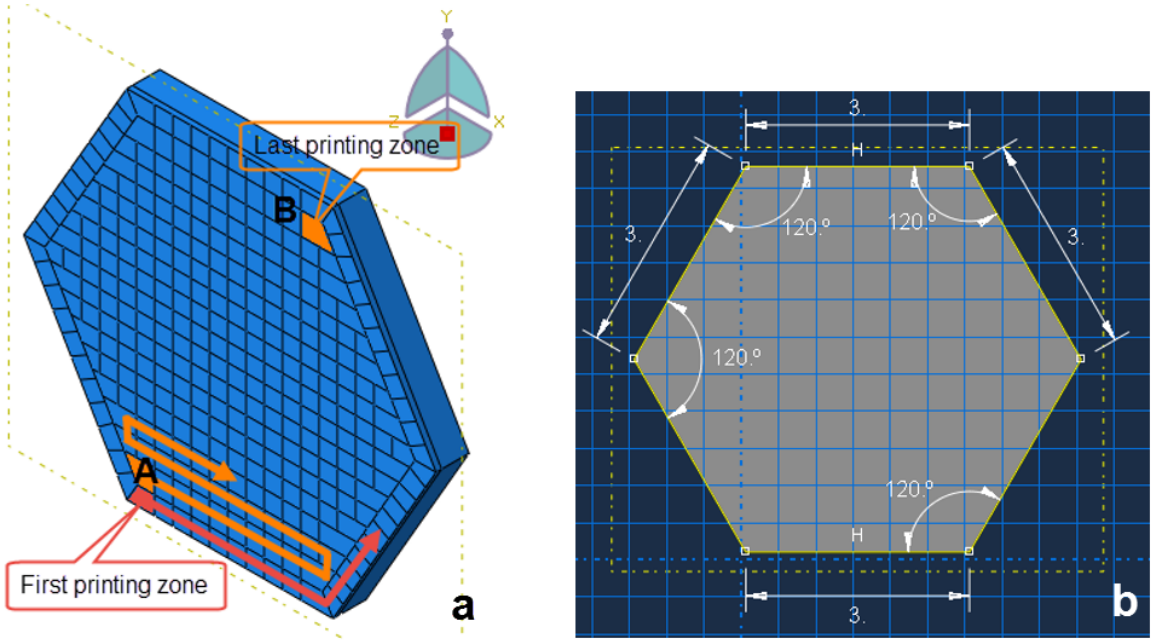

Figure 4.5. a. Scan zones and paths; b. Model dimensions

4.2.3 Thermal analysis

Melt pool specifications

Fig. 4.7 shows the moving melt pool in different positions. Fig. 4.7.e shows the final temperature distribution on the printed island at the end of step 317. In this step, time elapsed 0.0001second after passing of laser from the last square of the laser spot. This figure shows a uniform temperature distribution throughout the island just after 0.0634 of a second, which is the total time for printing the island. However, the top of the island shows the trace of the last track, high rate heat dissipation will remove it in a fraction of a hundredth of a second, such as the other tracks. In fact, Fig. 4.7.d shows that the trace of a track takes the time needed for printing approximately two tracks to disappear. The temperature range in Fig. 4.7.f shows that the temperature of the melt pool core is 1476.424 K and it drops down to about

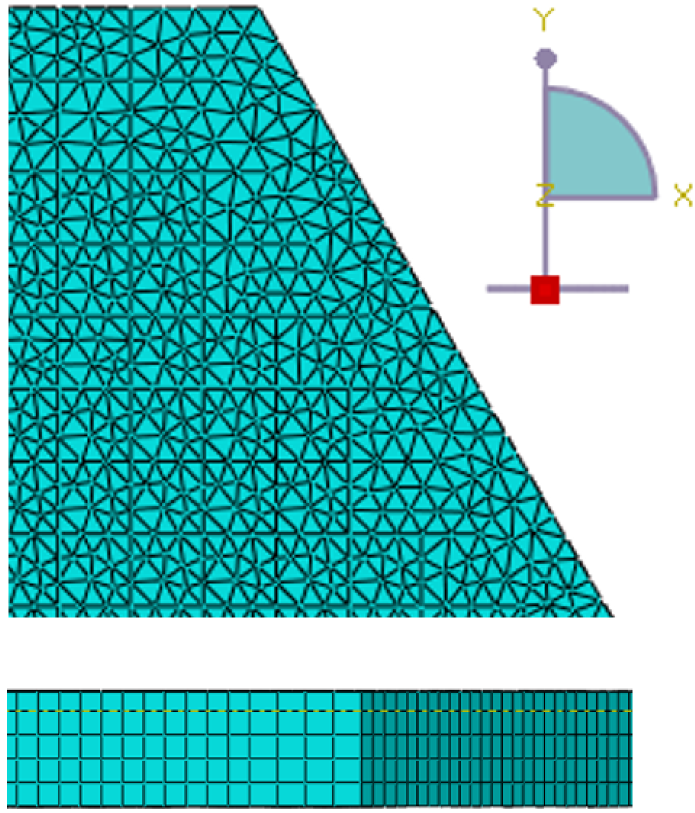

Figure 4.6. Mesh structure with wedge DC3D6

887 K at the tail of the melt pool. Fig. 4.8 shows that the melt pool penetrates about half of the first row of mesh, which is about 40 µm. According to the EOS manual, the layer thickness can alter between 20 µm to 80 µm and the default layer thickness of current machines in the industry is usually 30 µm. Hence, the resulted melt pool depth confirms the accuracy of the selected set of laser specifications, namely, laser power and scan speed and the simulated model. It also shows this set of parameter guarantee the bonding between the spread layer of powders and the layers beneath. Furthermore, it confirms the previous scholars experimental results regarding the possibility of remelting phenomena in the layer beneath by printing a new layer. This simulation takes around 24 hours to be complete.

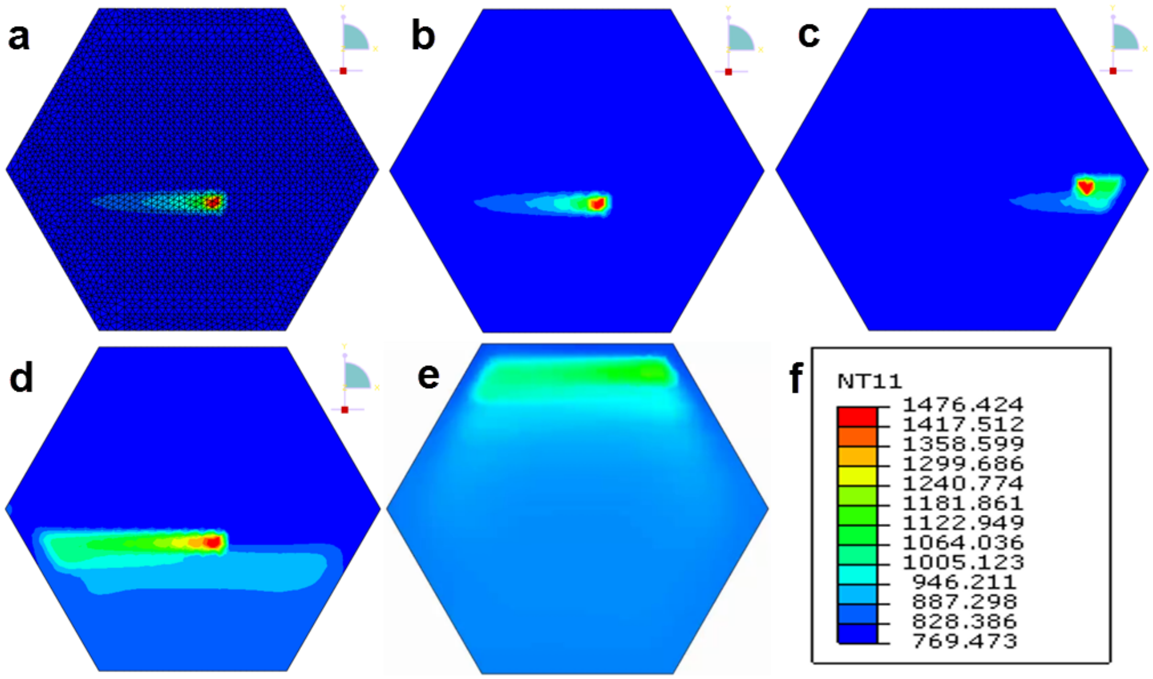

Figure 4.7. Moving melt pool in different positions: a, b, c: Heat flux visualization; d, e: Temperature nodal visualization; f. Temperature indicator of the melt pool

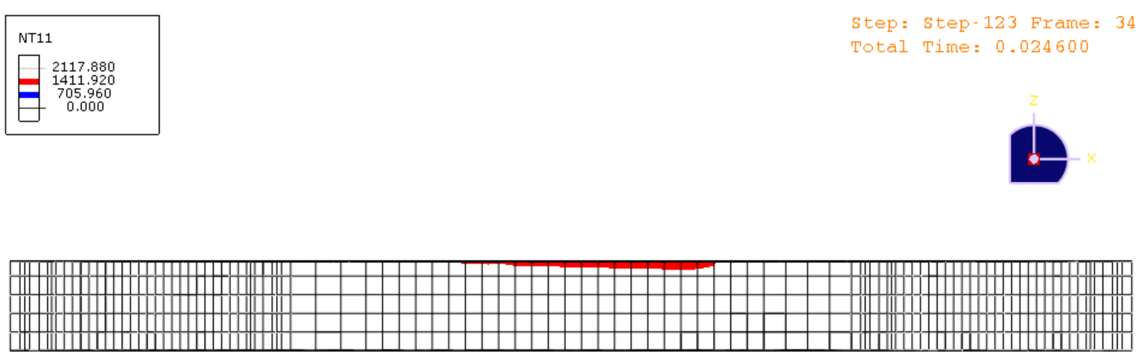

Figure 4.8. Melt pool depth at the side view of the printing island

Temperature profile of nodes in different positions

Explaining the thermal evolution of the printing island needs to consider each square zone consists of two different types of nodes. First, boundary nodes. These nodes which place on the boundary of each square zone are usually in common between two or more adjacent square zones. Some of these boundary nodes are in common between two consecutive adjacent square zones in a laser track; however, some of the others are in common between to adjacent square zones from two different laser tracks. The temperature vs. time profile for the latter one always shows two jumps such as Fig. 4.9. This is because the node is affected by thermal heat flux twice; once when the laser passes the first adjacent square zone and once again when it passes the second adjacent square zone. The second type of nodes is middle nodes. These nodes place inside a square zone and are not in common between any two different ones. The temporal profile for the middle nodes shows only one jump and a small bump before the jump such as Fig. 4.10 and Fig. 4.12. The bump happens when the laser scans the adjacent track just before the one that includes the node itself. This thermal effect raises the temperature up to around 125 K depends on the position of the node. Fig. 4.9.a shows the moment when the laser starts printing at the very first square zone. This square zone is on the edge of the island and the profile shows the temperature variation for the boundary node. This node is in common between the first zone and zone 65. As the Fig. 4.9.b shows the temperature jumps two times and every time it raises the temperature around 1000 K.

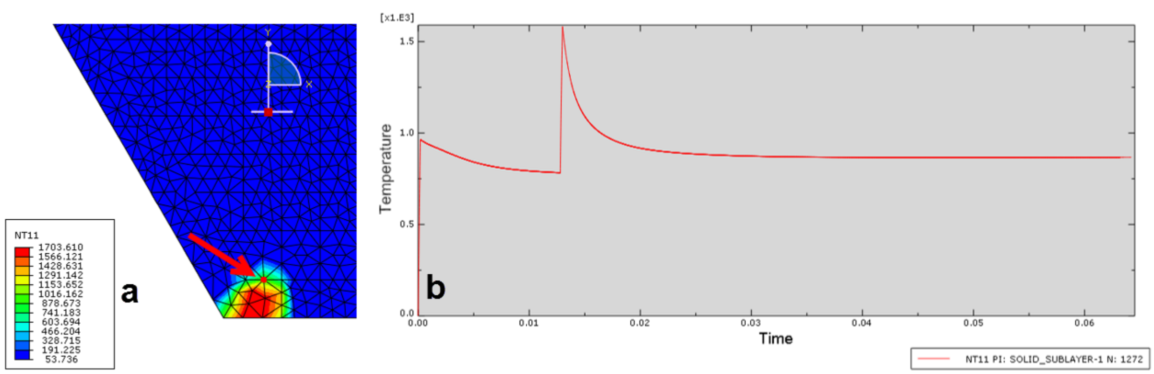

Figure 4.9. Temperature variation for a boundary node in zone one

Fig. 4.10.a shows the moment when the laser passing central node of the model. This node is a boundary node but it is in common between two consecutive square zones in one track and thus, the temperature profile in Fig. 4.10.b shows just one jump and a small bump before that.

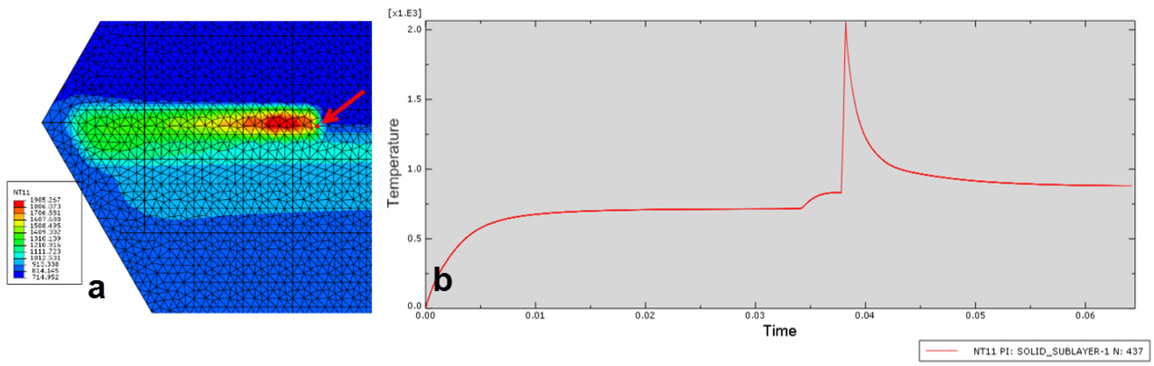

Figure 4.10. Temperature variation for the islands central node

Fig. 4.11 compares the temperature variation between two boundary nodes in the first square zone and the central zone. The temperature profile in Fig. 4.11.b shows that the time elapsed between the two jump at first square zone is longer than the one at the central square zone. The reason is there are 64 square zones, namely, 64 steps in simulation, between the two first jump while there are only 19 steps between the second two jumps. The temporal profile also reveals that it takes about only 0.015 of a second for the temperature to reach to a steady state after a jump.

Fig. 4.12 demonstrates the temperature variation at four middle nodes placed in four adjacent square zones, in four consecutive laser tracks. The temperature profile in Fig. 4.12.b shows that first, the temperature variation follows a very similar pattern for the nodes with the same type and same boundary conditions. Second, it shows a small bump after each jump and the time when it happens; in fact, the starting point of the jump in the temperature profile of the printing laser track coincides with the starting point of the bump in the temperature profile of the prior printing laser

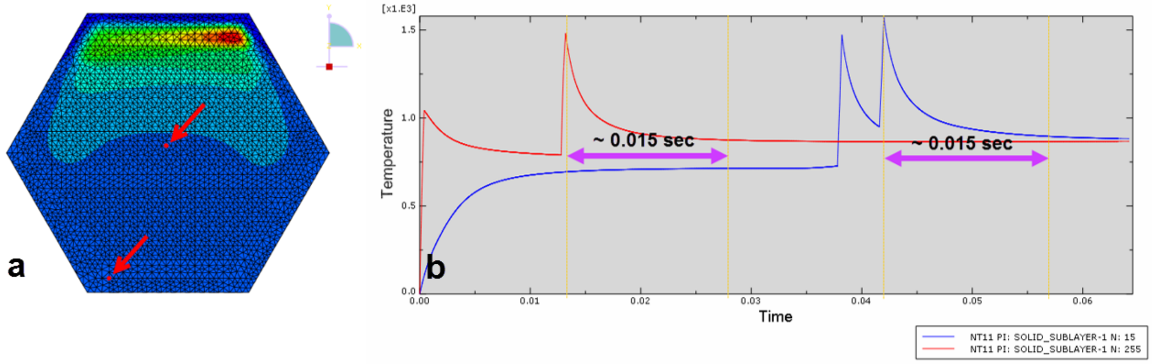

Figure 4.11. Comparing temperature variation between boundary nodes in square zone 1 and central zone

track. This phenomenon shows that a melt pool significantly affects the temperature of the adjacent areas within a distance of one hatch space. Fig. 4.12.b also shows that the time elapsed between the first two jumps is almost equal to the one between the third two jumps and it is longer than the one between the second two jumps. This is because there are 18 square zones between the first two nodes; however, there are only 12 square zones between nodes 2 and 3 (Fig. 4.12.a). Furthermore, the temperature profile shows that the temperature in all the objective points drops down to a steady temperature rapidly.

Fig. 4.13 demonstrates the temperature variation at four middle nodes placed in four consecutive square zones, in one laser tracks. The temperature profile in Fig. 4.13.b shows that first, the temperature variation follows a very similar pattern for the nodes with the same type and same boundary conditions. Second, it shows a small bump just before each jump. Aforementioned observations show that the bump happens when the laser scans the adjacent track just before the one that includes the node itself. This phenomenon shows that a melt pool significantly affects the temperature of the adjacent areas within a distance of one hatch space. Furthermore, the temperature profile shows that the temperature in all the objective points drops down to a steady temperature rapidly.

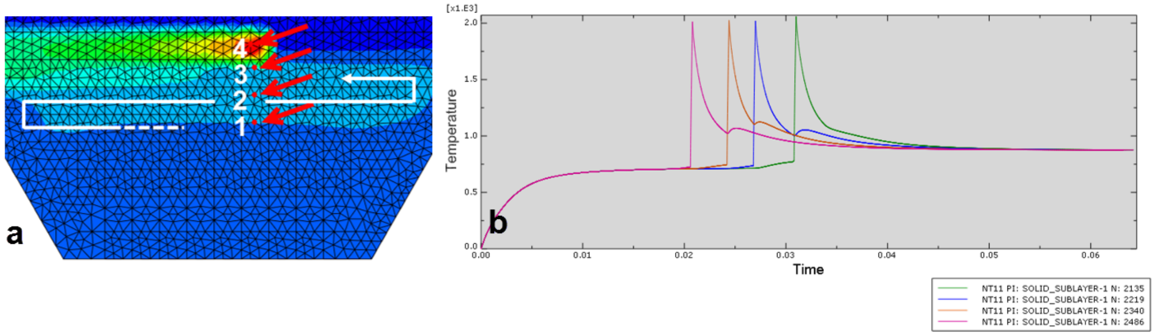

Figure 4.12. Comparing temperature variation between the middle nodes of adjacent square zones in different consecutive laser track

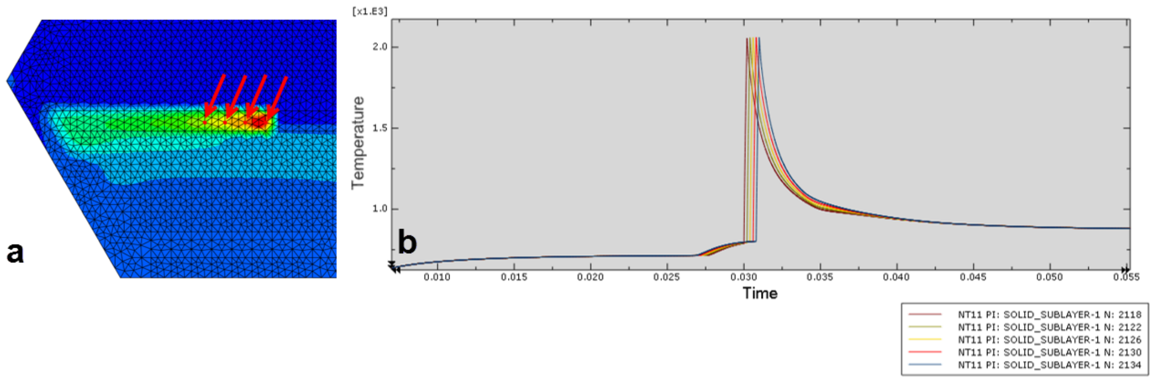

Figure 4.13. Comparing temperature variation between middle nodes of consecutive zones in one track

Fig. 4.14.a shows a random node at the back of the island and Fig. 4.14.b shows the temperature variation during the printing of the island. This node is a boundary node which is in common between two adjacent square zones in a laser track but the profile trend is similar for all the other types of nodes at the back of the island. Th profile shows a gradual increase in the temperature starts at the primary predefined field temperature and reach to the final temperature of the island which is in common between all nodes both sides of the island.

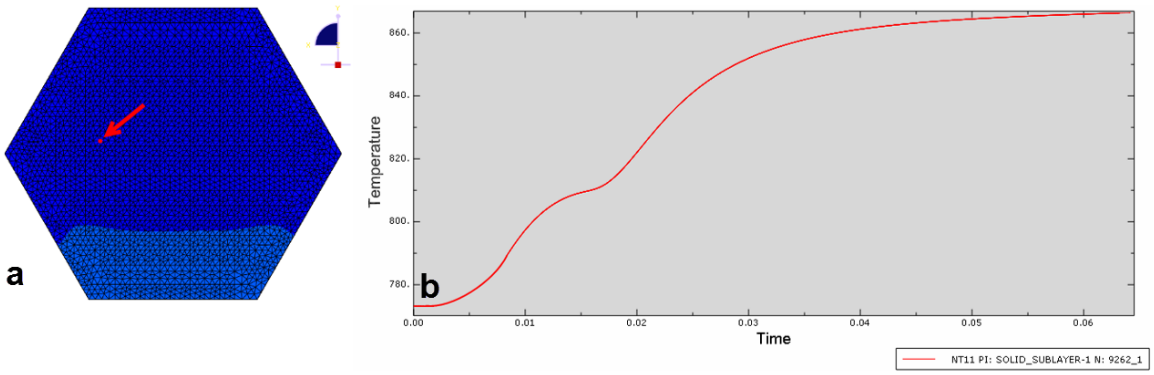

Figure 4.14. Temperature variation of a random node on the back of the model

Nodal temperature data of all nodes show that after printing of the island the nodal temperature drops down to a final steady temperature. Hense, the primary temperature of the sub-layers raises up from 773.15 K to around at the start of the process to around 875 K at the end of printing of the island. Table 4.2 shows the final temperature of a boundary node from the first zone, the model central zone, a random node from the front, and a random node from the back.

Table 4.2.
Final temperature of nodes in different positions

No.	Node position	Temperature at last step
1	A boundary node in the first zone	867.343 K
2	Central node of the model	879.733 K
3	A random node at the front surface	875.77 K
4	A random node at the back surface	875.302 K

4.3 Investigate the effect of different scan strategies on temperature distribution and temperature uniformity of a single printing layer

4.3.1 Rastering pattern

The designed methodology simulates the temperature distribution generated by the chessboard scanning strategy. It assists the designers to examine the effects of the geometric design of each layer, support structures, and process parameters on temperature distribution, temperature value, and heat-affected zones (HAZ) and modify their design if it is necessary. It also assists scholars to study different scan strategies, namely, different patterns and process parameters to optimize the thermal evolution of the process. For instances, this simulation technique employs two different scan patterns, namely, rastering pattern and helical pattern to print the island in chessboard scanning strategy and approximates the temperature distribution throughout a printing layer. This circular layer with a radius of 15 mm consists 36 islands and sits on top of 0.4 mm solid layers (Fig. 4.15.a), and in the middle of a 40 by 40 mm powder layer (Fig. 4.15.b). The layer thickness is 0.08 mm. This section shows the temperature distribution and thermal analysis for rastering pattern. This pattern prints the islands on the printing layer in a simple back and forth path. Fig. 4.15.b shows the printing order of the islands with the red arrow path. Furthermore, Fig. 4.15.c shows the approach of how the method meshes the printing layer to expedite the simulation. The approximate global size is 0.4 mm in the printing area; however, the size of edge elements is 1 mm.

This methodology leverages the simulation results in section 5.2 to expedite the simulation of chessboard strategy. The results showed that it takes 0.0632 fractions of a second to scan the entire island and the final nodal temperature of the islands nodes tends to around 875 K after scanning. Hence, the simulation technique first exerts different values of surface heat flux in the specified period on a random island in the printing layer (Fig. 4.16.a). Tried and error method reveals that a load with the magnitude of 2830 generates a uniform temperature distribution with a value

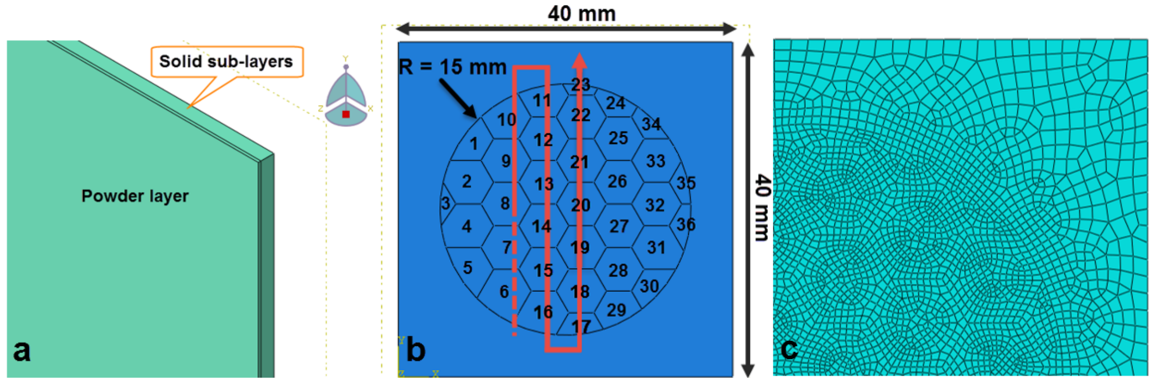

Figure 4.15. a. Powder layer and solid sub-layers in the printing sample; b. the model specifications; c. mesh structure

around 875 K (Fig. 4.16.d) throughout the island (Fig. 4.16.b, Fig. 4.16.c). Section 5.2 shows the dimension of the islands and all the other parameters for simulation.

Next, the simulation technique exerts the derived load in the prior step to all the islands, which cover the printing layer. The technique employs a rastering pattern, shown in Fig. 4.15.b, to print the islands in the chessboard scanning strategy and approximates the temperature distribution throughout the layer. Fig. 4.17 shows the resulted temperature distribution and temperature indicator.

Examination of the temperature profile for different printing islands in this scanning pattern gives better vision to understand the thermal evolution of the printing process. Fig. 4.18 shows the temperature variation at a middle node of the first printing island. The profile shows temperature first raises up rapidly during printing of the island and reaches to the pick of 872.493 K then, gradually drops down to 754.084 K at the last step and reaches to plateau.

Fig. 4.19 shows the temperature variation at a middle node of the middle printing island, namely, zone number 18 out of 36 different islands. The profile shows a flat temperature profile before printing the island, it raises up rapidly during the printing

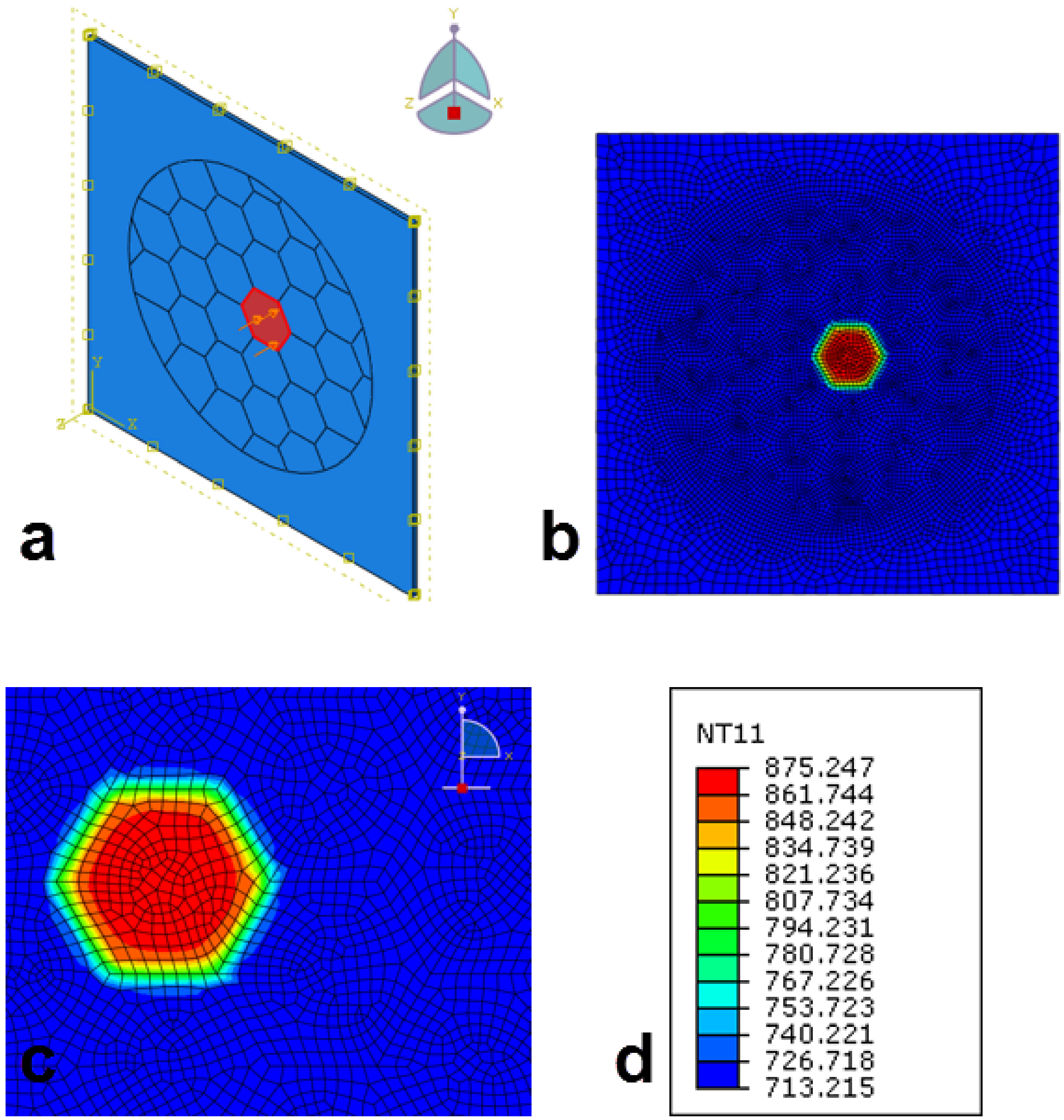

Figure 4.16. a. the island exerted by the heat flux; b, c. the resulted temperature distribution in the printed island; d. temperature indicator

of the island and reaches to the pick of 867.641 K. Then, it gradually drops down to 791.777 K at the last step and reaches to plateau.

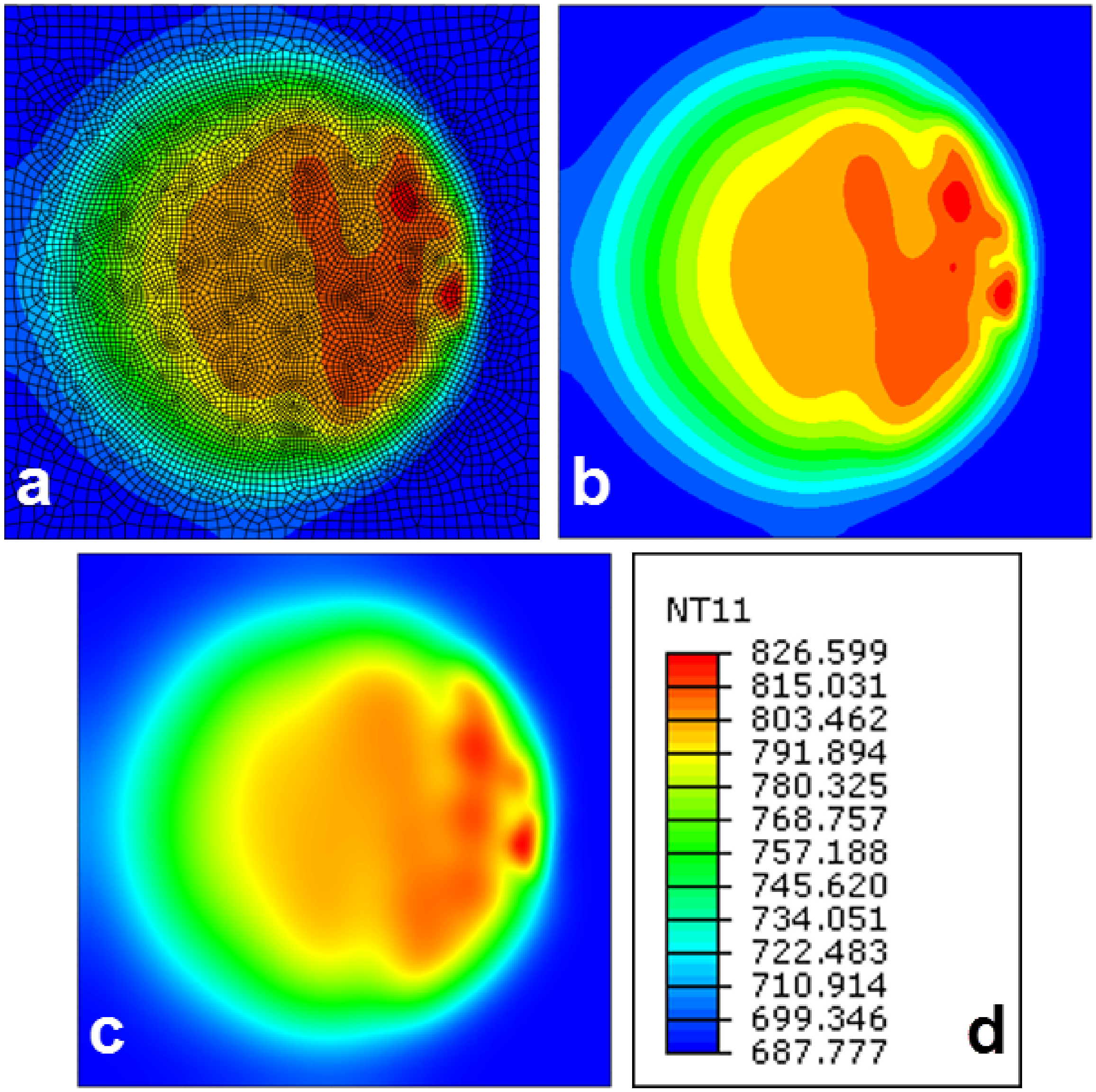

Figure 4.17. Resulted temperature distribution (a, b, c) and temperature indicator (d) for a layer scanned by rastering pattern in chessboard strategy

Fig. 4.20 shows the temperature variation at a middle node of the last printing island. The profile shows temperature raises up rapidly during printing of the island, it reaches to the pick of 881.227 K and then, drops down to 821.685 K at the last step.

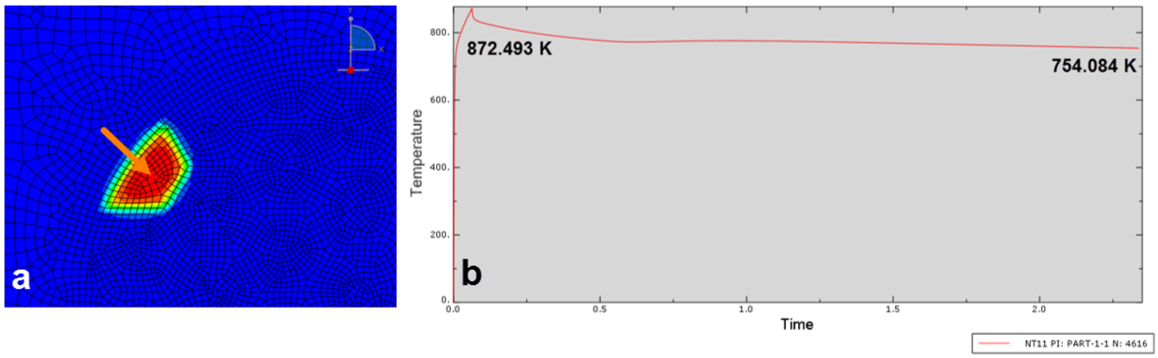

Figure 4.18. Temperature variation at a middle node in the first printing island

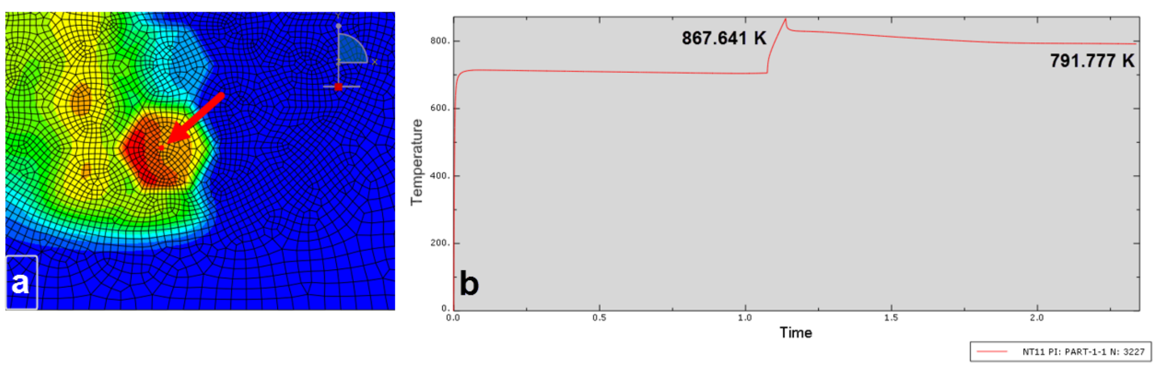

Figure 4.19. Temperature variation at a middle node in the middle printing island

As the prior three temperature profiles show, the pick temperature in all three islands are very close to each other; however, the temperature at the final step significantly increases in the last printing island, middle island, and the first island respectively. The reason is that the cooling period is longer for the first island compared with the other two islands and it is longer in the middle island compared with the last printing island.

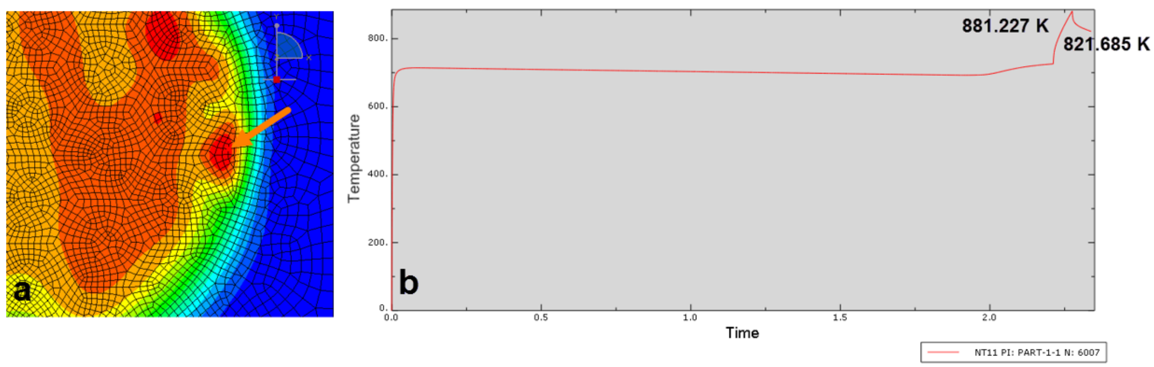

Figure 4.20. Temperature variation at a middle node in the last printing island

Fig. 4.21 shows the temperature variation at the central node of the model. The profile shows temperature raises up rapidly during printing of the island, it reaches to its pick and then, gradually drops down and reaches to plateau. Furthermore, the profile shows a small bump before the jump. This is because the central node is inside island number 20 and it is very close to the boundary of the island; hence, laser affects thermally on this node while it is printing the previous neighbor islands, namely, islands number 13 and 14.

4.3.2 Helix pattern

This section shows the temperature distribution and thermal analysis for the helical pattern. This pattern starts printing the islands from the central island on the

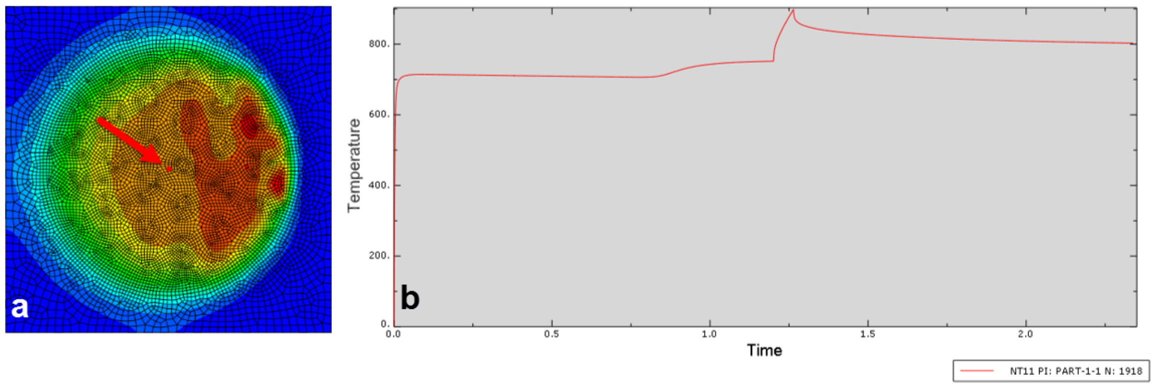

Figure 4.21. Temperature variation in the central node of the model

printing layer and continues printing toward the peripheral islands in a helical path. Fig. 4.22 shows the printing order of the islands with the red arrow path. All the other parameters are the same as the prior sections.

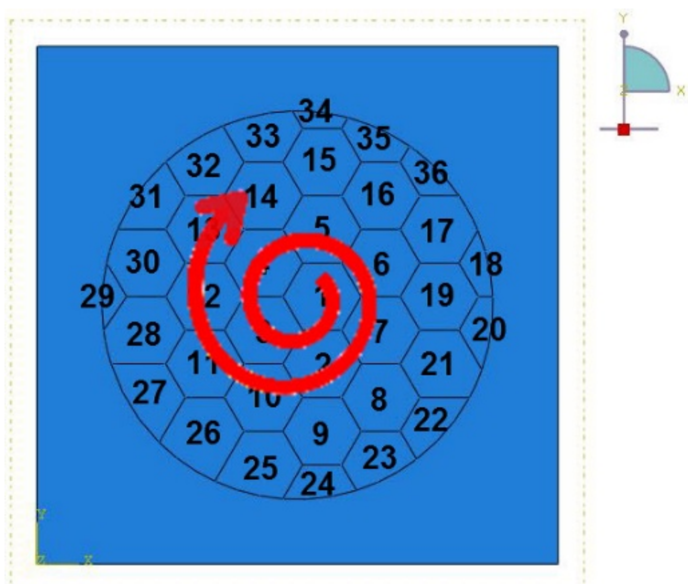

Figure 4.22. Printing order of the islands in the helical pattern

The technique employs this pattern to print the islands in the chessboard scanning strategy and approximates the temperature distribution throughout the layer. Fig. 4.23 shows the resulted temperature distribution and temperature indicator.

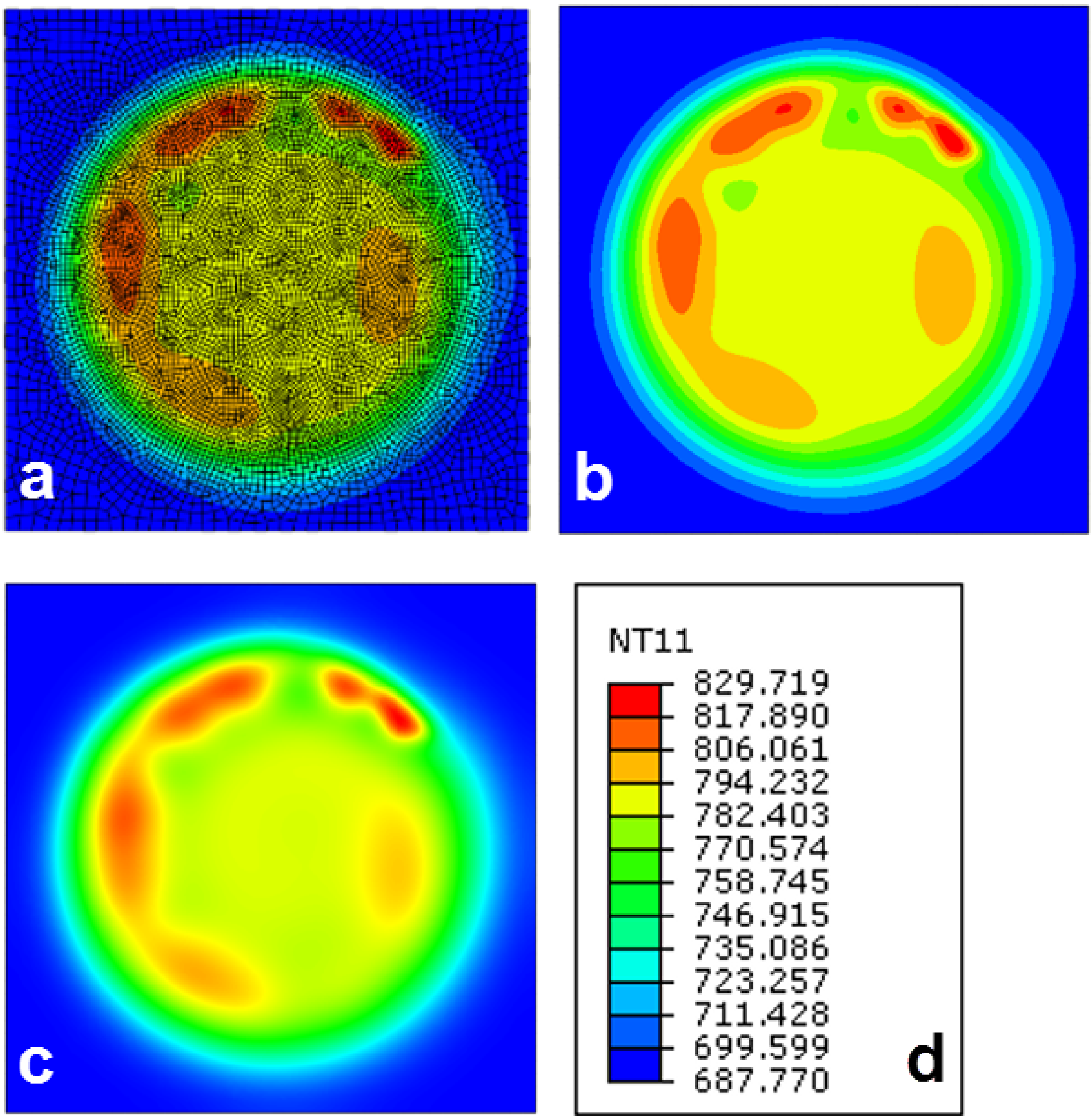

Figure 4.23. Resulted temperature distribution (a, b, c) and temperature indicator (d) for a layer scanned by the helical pattern in chessboard strategy

Examination of the temperature profile for different printing islands in this scanning pattern gives better vision to understand the thermal evolution of the printing process. Fig. 4.24 shows the temperature variation at a middle node of the first printing island. The profile shows temperature first raises up rapidly during printing of the island and reaches to the pick of 873.838 K then, gradually drops down to 788.766 K at the last step and reaches to plateau.

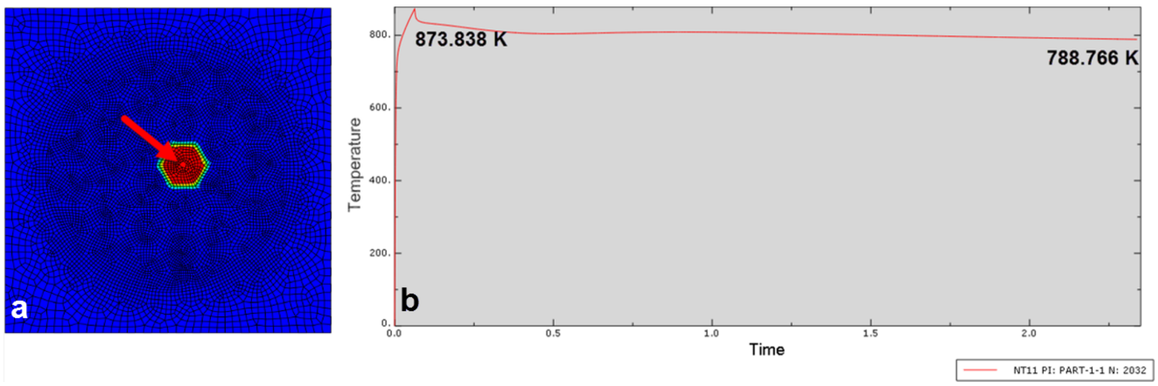

Figure 4.24. Temperature variation at a middle node in the first printing island

Fig. 4.25 shows the temperature variation at a middle node of the middle printing island, namely, zone number 18 out of 36 different islands. The profile shows a flat temperature profile before printing the island, it raises up rapidly during the printing of the island and reaches to the pick of 857.982 K. Then, it gradually drops down to 756.655 K at the last step and reaches to plateau.

Fig. 4.26 shows the temperature variation at a middle node of the last printing island. The profile shows temperature raises up rapidly during printing of the island, it reaches to the pick of 890.977 K and then, drops down to 829.216 K at the last step. As the prior three temperature profiles show, contrary to the rastering pattern, the pick and ultimate temperature in first printing island are significantly higher than the ones in the middle printing island. The reason is all adjacent islands of island number one are powders with small conductivity; however, island number 18 is

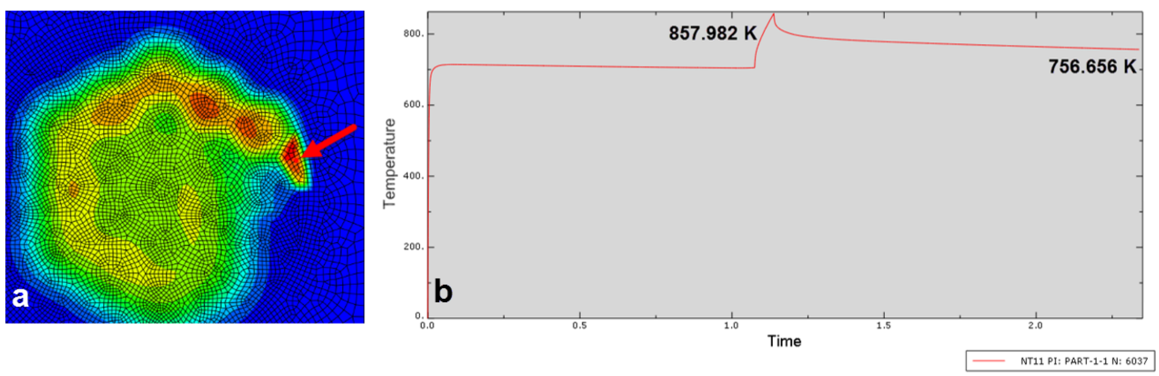

Figure 4.25. Temperature variation at a middle node in the middle printing island

surrounded by a solid island with higher conductivity. Furthermore, the temperature gradient between the middle island and adjacent islands in the helical pattern is higher compared with the rastering pattern and hence, the cooling rate is higher. The last island posses highest pick temperature such as the one in rastering pattern because of heat accumulation of previously printed islands.

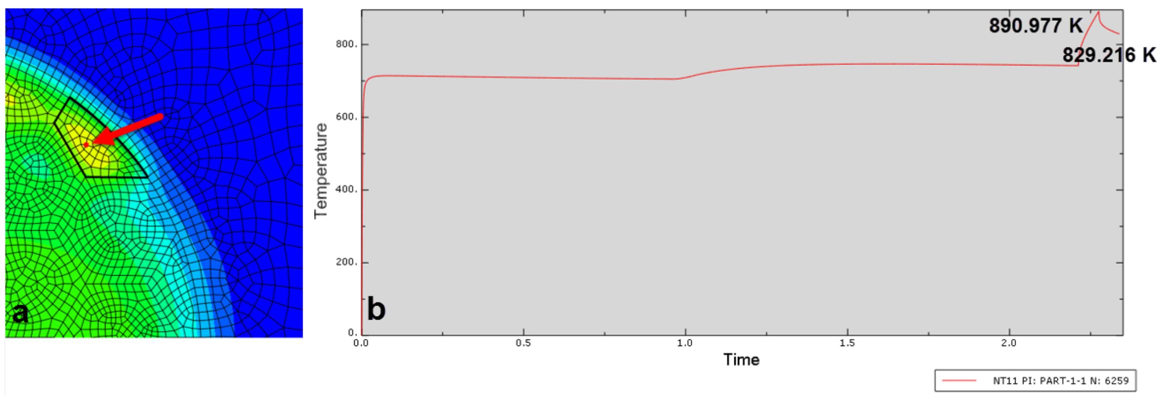

Figure 4.26. Temperature variation at a middle node in the last printing island

Fig. 4.27 shows the temperature variation at the central node of the model. The profile shows temperature raises up rapidly during printing of the island, it reaches to its pick and then, gradually drops down and reaches to plateau. This jump happens at the very beginning of the profile because the node sits in the first printing zone and thus, the temperature profile for this node is quite similar to the Fig. 4.24.

4.3.3 Tessellation pattern

Fig. 4.28.a and Fig. 4.28.b show the printing order of the islands in the tessellation-scanning pattern for the designed layer introduced in previous sections. A developed code in MATLAB uses the coordinate of the center of each island, which we measured manually (Fig. 4.28.c and Table 4.3), to arrange the islands for print. The code shows the order of printing as follows:

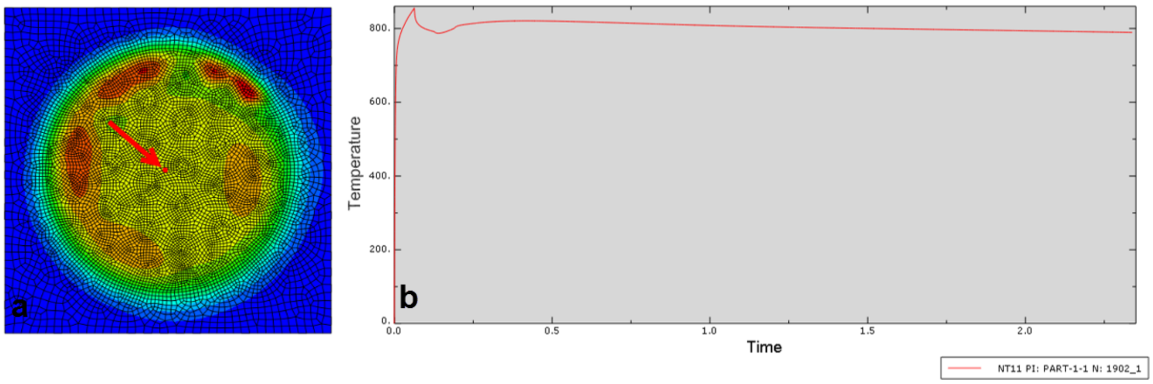

Figure 4.27. Temperature variation in the central node of the model

17, 23, 3, 36, 19, 6, 10, 34, 21, 30, 8, 13, 26, 9, 14, 12, 20, 25, 27, 32, 15, 7, 5, 16, 29, 28,11, 24, 18, 1, 33, 31, 35, 2, 4, 22.

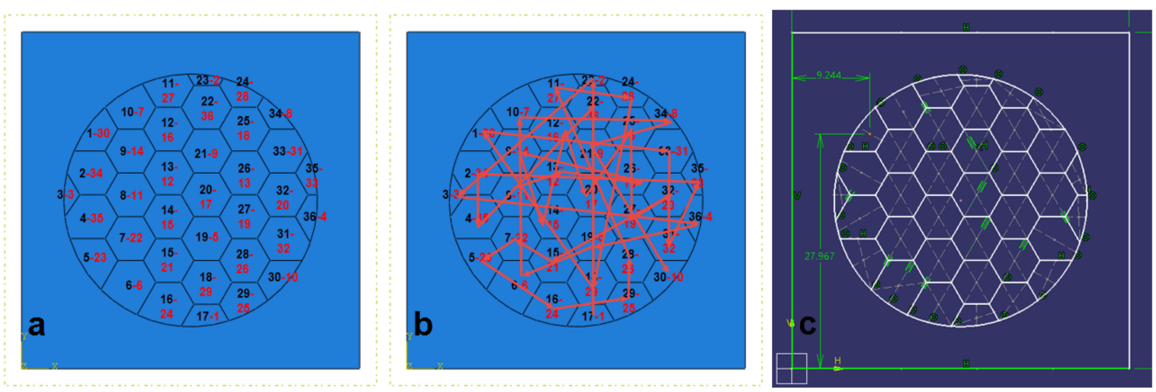

Figure 4.28. Printing order of the islands in the helical pattern

Fig. 4.29 shows the temperature distribution and temperature indicator for the layer printed by this pattern. Fig. 4.28.b shows the printing order of the islands with the red arrow path. All other parameters are the same as the prior sections.

Table 4.3.
The coordinate of the center of each island

No.	X	Y	No.	X	Y
1	9.244	27.967	**18**	21.9	15.464
2	8.215	23.365	**19**	21.9	20.66
3	5.792	20.66	**20**	21.9	25.856
4	8.049	17.86	**21**	21.9	31.052
5	8.472	12.907	**22**	21.9	34.404
6	12.647	9.83	**23**	25.892	32.77
7	12.9	15.464	**24**	26.4	28.454
8	12.9	20.66	**25**	26.4	23.258
9	12.9	25.856	**26**	26.4	18.062
10	13.184	30.561	**27**	26.4	12.866
11	17.744	33.055	**28**	26.218	7.985
12	17.4	28.454	**29**	30.283	10.624
13	17.4	23.258	**30**	31.167	15.31
14	17.4	18.062	**31**	30.9	20.66
15	17.4	12.866	**32**	30.9	25.856
16	17.4	7.67	**33**	29.932	29.879
17	21.9	6.027	**34**	34.099	22.507

Examination of the temperature profile for different printing islands in this scanning pattern gives better vision to understand the thermal evolution of the printing process. Fig. 4.30 shows the temperature variation at a middle node of the first printing island. The profile shows temperature first raises up rapidly during printing of the island and reaches to the pick of 870.758 K then, gradually drops down to 756.065 K at the last step. We can see a small fluctuation at the end of the profile, which shows the effects of printing the adjacent islands, namely, 24, 25, and 29 on the temperature of the first zone.

Fig. 4.31 shows the temperature variation at a middle node of the middle printing island, namely, zone number 18 out of 36 different islands. The profile shows a flat temperature profile before printing the island, it raises up rapidly during the printing of the island and reaches to the pick of 870.758 K. Then, it gradually drops down to 756.065 K at the last step and reaches to plateau.

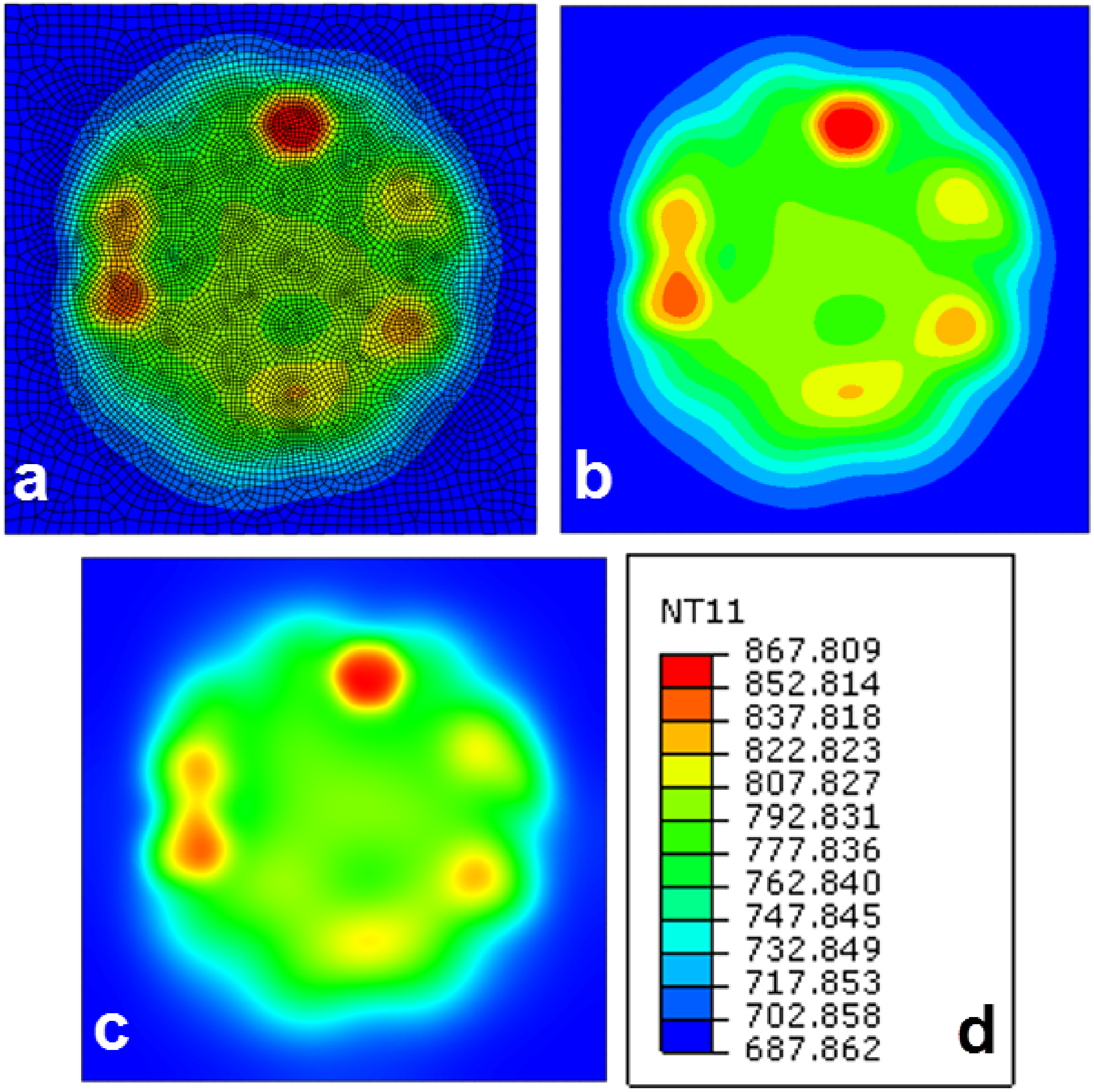

Figure 4.29. Resulted temperature distribution (a, b, c) and temperature indicator (d) for a layer scanned by the helical pattern in chessboard strategy

Fig. 4.32 shows the temperature variation at a middle node of the last printing island. The profile shows temperature raises up rapidly during printing of the island, it reaches to the pick of 906.401 K and then, drops down to 866.178 K at the last step. This island has a flat profile before printing of the island. As the prior three

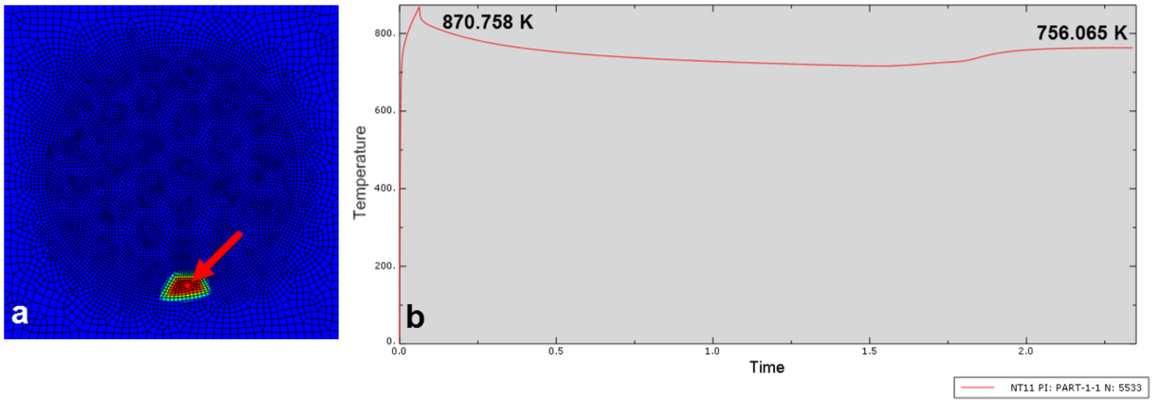

Figure 4.30. Temperature variation at a middle node in the first printing island

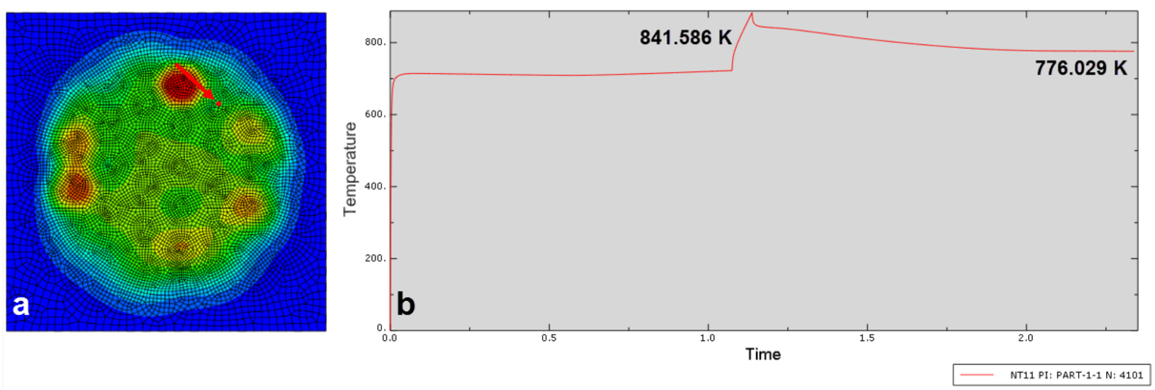

Figure 4.31. Temperature variation at a middle node in the middle printing island

temperature profiles show the pick temperature for the first island is higher than the middle. The reason is the first island surrounded by powder whose conductivity is less than the solid islands surrounded zone 18. The highest pick temperature is for the last printed island because the heat accumulation in the printed layer and as a result, the temperature of the last island just before the jump is higher than the other two island. The ultimate temperature increases with the printing process.

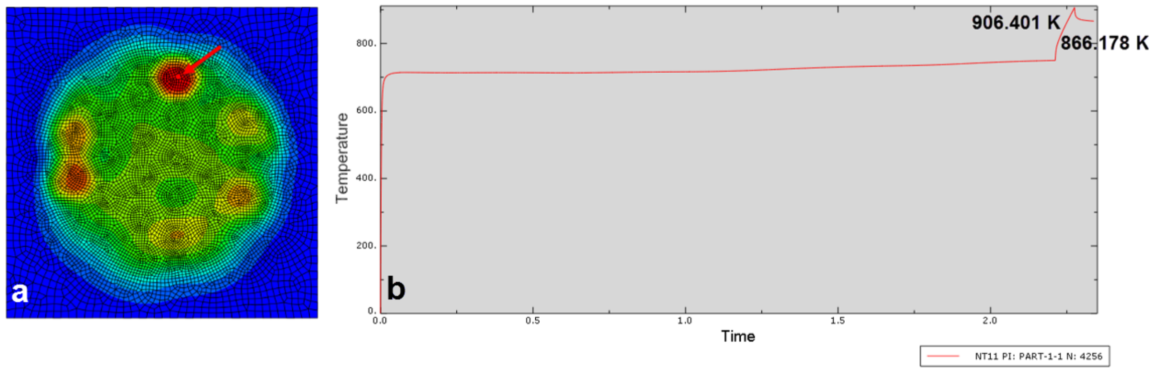

Figure 4.32. Temperature variation at a middle node in the last printing island

Fig. 4.33 shows the temperature variation at the central node of the model. The profile shows temperature raises up rapidly during printing of the island, it reaches to its pick and then, gradually drops down and reaches to plateau.

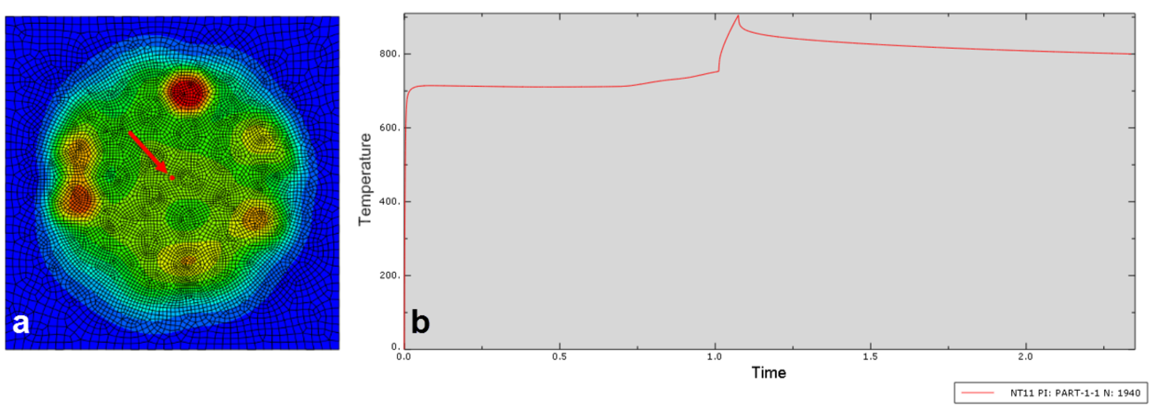

Figure 4.33. Temperature variation in the central node of the model

4.3.4 Employment of the tessellation pattern for the ASTM specimen

The tessellation-scanning pattern can generate a uniform temperature distribution especially in specimens with long dimensions. This reduces the warping and elevates the ultimate printing quality. For instance, the developed simulation technique employs the tessellation-scanning pattern to print the ASTM D3039 standard specimen for tensile strength test. As Fig. 4.34 shows, this specimen has long dimensions. The current 3D machine cannot print this sample because warping jams the blade up during the fabrication process.

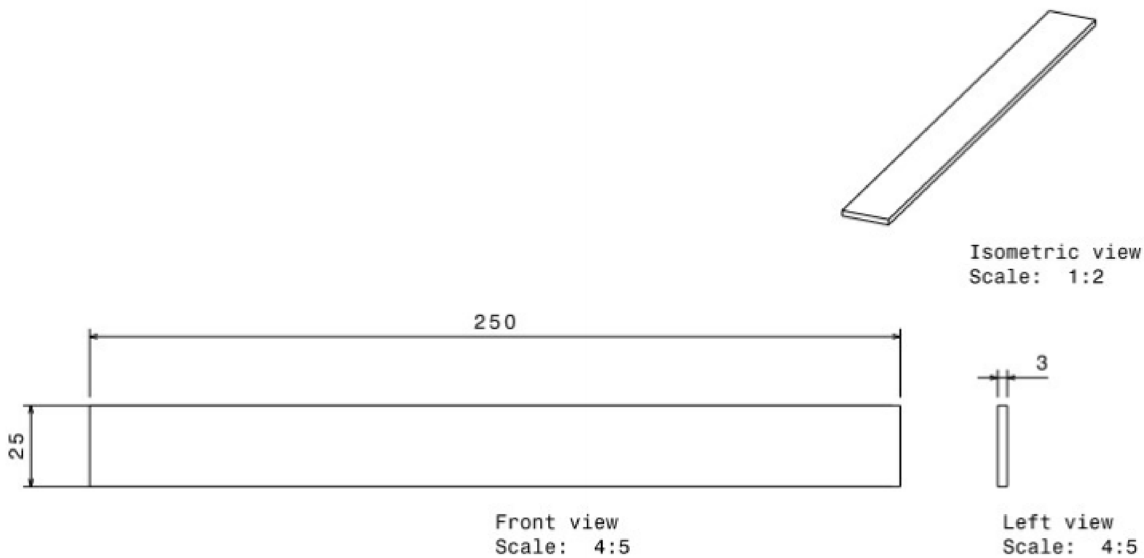

Figure 4.34. ASTM D039 specimen dimension

Fig. 4.35 shows how the islands are numbered. A developed code in MATLAB reveals this order for printing of the islands:

5, 271, 25, 35, 151, 11, 191, 195, 105, 125, 85, 213, 96, 36, 250, 206, 115, 66, 110, 30, 50, 235, 240, 155, 16, 75, 126, 205, 3, 15, 53, 173, 201, 161, 101, 131, 61, 221, 41, 181, 31, 91, 171, 241, 1, 261, 211, 111, 81, 121, 51, 141, 231, 251, 21, 71, 175, 135, 275, 253, 143, 163, 153, 63, 83, 122, 59, 222, 48, 62, 42, 64, 118, 88, 242, 114, 44, 234, 254, 134, 34, 74, 124, 174, 263, 203, 43, 23, 103, 113, 133, 183, 13, 93, 243, 33, 273, 223, 123, 73, 233, 193, 185, 65, 165, 225, 245, 95, 145, 265, 9, 230, 238, 208, 27, 77, 97, 182, 39, 192, 28, 176, 140, 207, 189, 237, 229, 92, 184, 56, 8, 197, 139, 132, 239, 160, 164, 220, 217, 137, 47, 67, 247, 7, 127, 57, 257, 167, 147, 117, 17, 177, 37, 87, 187, 227, 157, 107, 267, 169, 142, 259, 168, 209, 112, 108, 218, 22, 38, 52, 102, 219, 202, 18, 109, 149, 119, 172, 162, 78, 128, 2, 262, 58, 32, 99, 69, 152, 98, 252, 249, 19, 198, 79, 138, 159, 248, 129, 258, 72, 188, 179, 158, 199, 178, 29, 49, 232, 68, 12, 148, 228, 82, 89, 212, 268, 272, 204, 104, 24, 144, 194, 14, 224, 84, 154, 244, 54, 94, 269, 214, 260, 180, 70, 130, 20, 215, 210, 190, 55, 120, 10, 90, 60, 45, 80, 150, 40, 200, 255, 170, 100, 270, 26, 116, 186, 216, 146, 246, 226, 266, 136, 86, 6, 166, 236, 106, 46, 156, 76, 256, 196, 274, 264, 4.

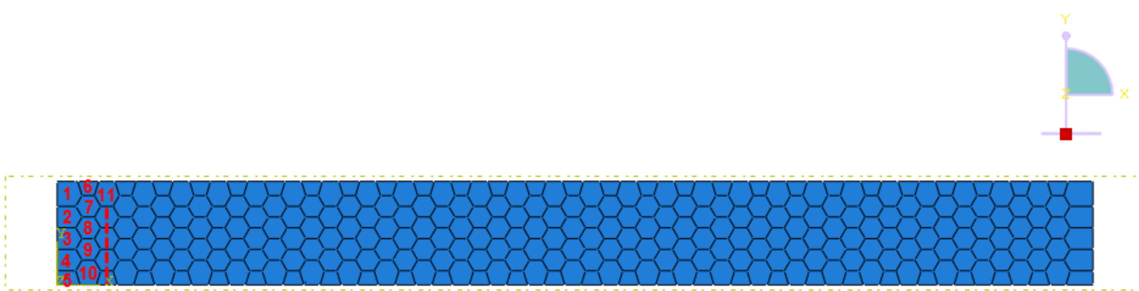

Figure 4.35. The primary number of the islands before ordering for print

Fig. 4.36 shows the temperature distribution and temperature indicator for the layer printed by tessellation-scanning pattern. The generated uniform temperature decreases warping caused by temperature gradient and heat stress.

Fig. 4.37 shows that temperature variation in different printing islands is uniform and the only fluctuation is the time when the laser scans the island. The defined pattern to jump between the islands makes enough time between printings of the islands to cool them out and avoid heat accumulation.

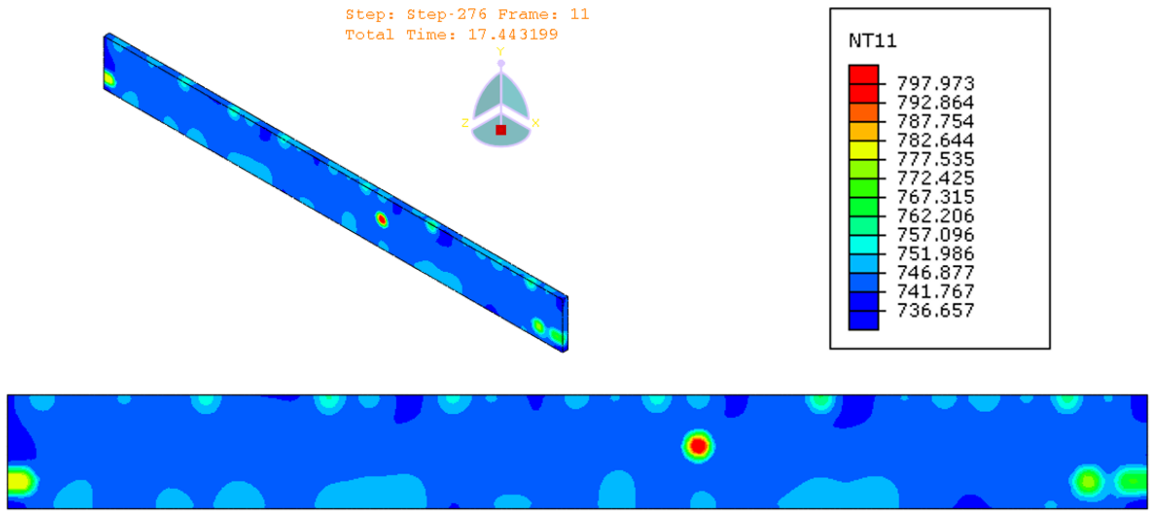

Figure 4.36. Temperature distribution and temperature indicator in ASTM D3039 specimen after printing by tessellation pattern

4.3.5 Comparison of different printing strategies by the developed thermography methodology

The profiles show that the ultimate temperature of the island after the jump (printing the island) is higher compared to the temperature before the jump in all printing patterns; however, this temperature varies for different islands in different patterns. The pick temperature of the same printing island, namely, the first, middle, and last one is very close to each other for all three patterns; however, tessellation pattern possesses the minimum one for the first and middle island and the maximum one for the last printing island. Fig. 4.38 shows the selected threshold temperature to depict HAZ. ABAQUS uses this temperature to generate the bicolor thermal image from different printing strategies. The selected value for threshold temperature depends upon the material and obtaining a precise one needs some practical experiments. As it was already mentioned, the thermography methodology creates this bicolor image by the employment of a palette in IR Max software. The thermography methodology reveals the other specifications for the printing patterns. As it is already

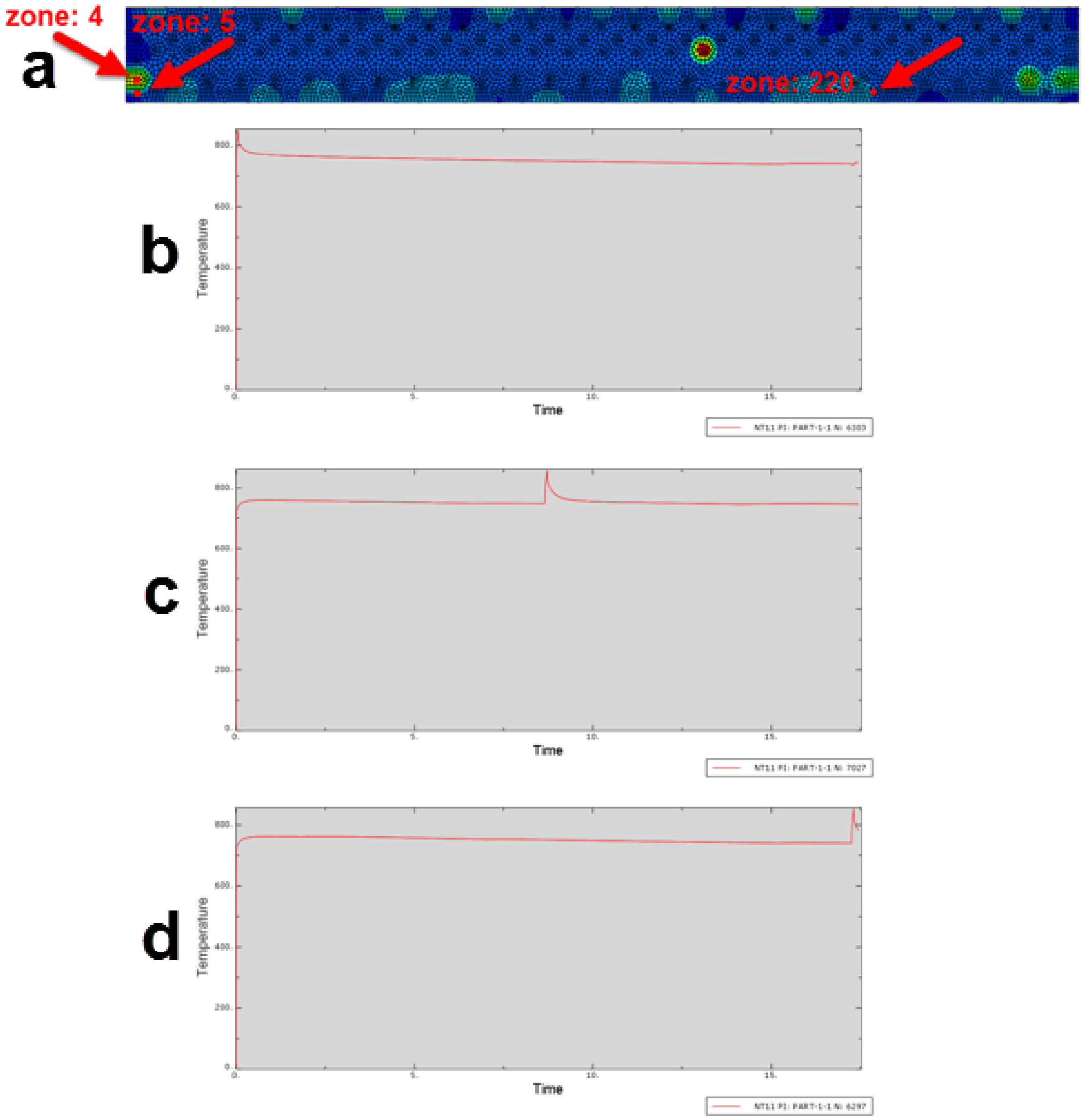

Figure 4.37. a. printing islands in ASTM specimen. Temperature variation in b. the first printing zone (zone 5) c. the middle printing zone (zone 220), and d. the last printing zone (zone 4)

explained in chapter 4, the thermography methodology receives the bicolor thermal image, converts it to a black and white image, and finally extracts all the necessary information. Fig. 4.39.b shows the detected HAZ in rastering pattern and Fig. 4.40

shows the variation in average temperature during the printing process with this pattern. Fig. 4.41 shows the information extracted by the thermography methodology for this pattern.

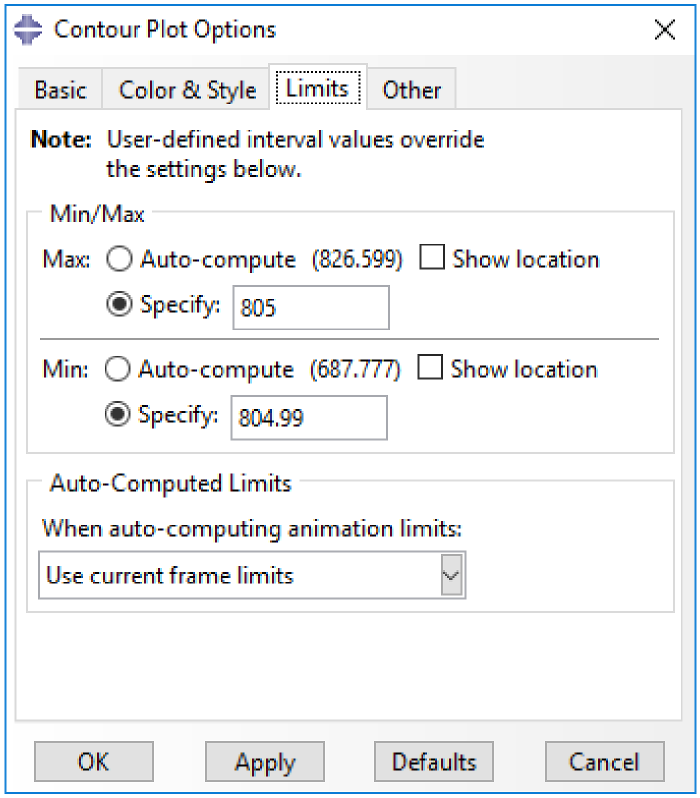

Figure 4.38. Defining the threshold temperature in ABAQUS to depict HAZ in a bicolor thermal image

Fig. 4.42.b shows the detected HAZ in helical pattern and Fig. 4.43 shows the variation in average temperature during the printing process with this pattern. Fig. 4.44 shows the information extracted by the thermography methodology for this pattern.

Fig. 4.45.b shows the detected HAZ in helical pattern and Fig. 4.46 shows the variation in average temperature during the printing process with this pattern. Fig. 4.47 shows the information extracted by the thermography methodology for this pattern.

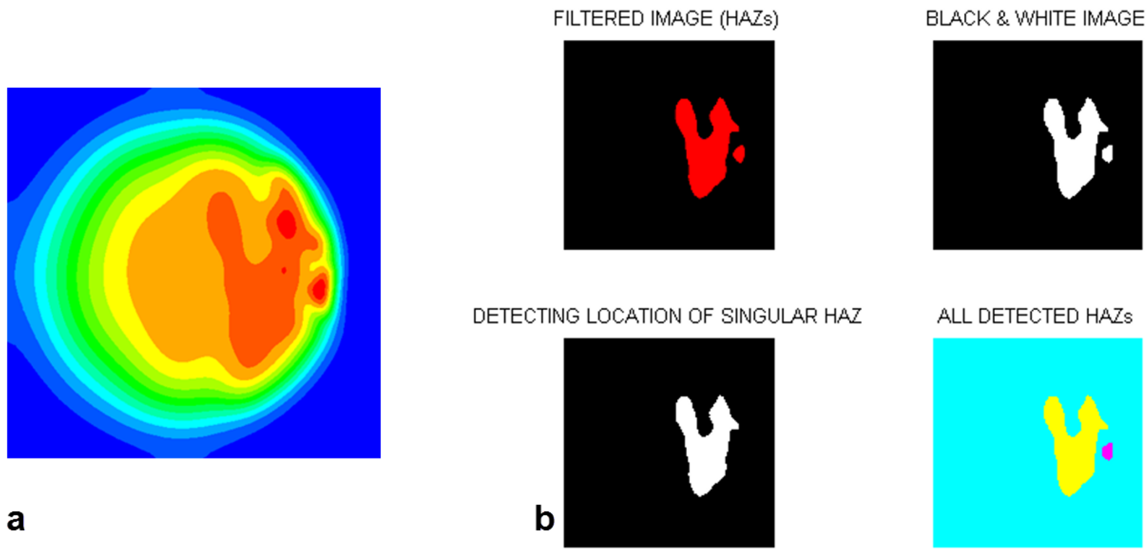

Figure 4.39. a. Temperature distribution, b. detected HAZ in the rastering pattern

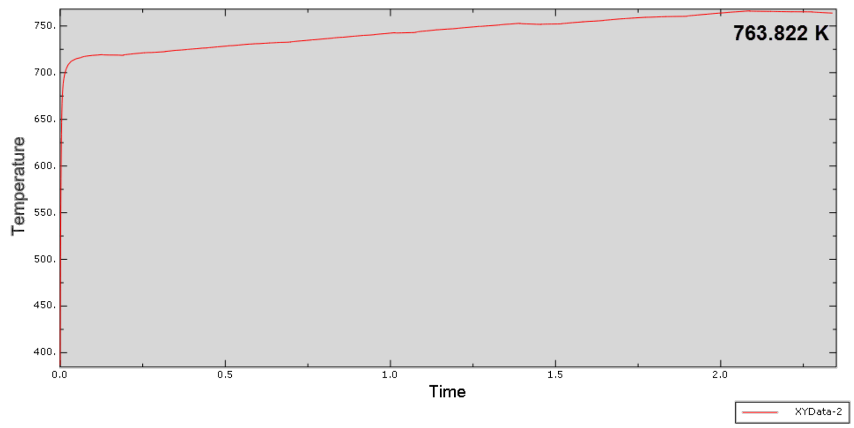

Figure 4.40. The average temperature profile of the entire layer printed by rastering pattern

The results show that the average temperature of printing layers increases gradually in all the printing patterns with almost a same trend and rate. The final average temperature is almost the same in all printing patterns; however, each printing pattern causes HAZs with different size and circumference. Rastering pattern generates just two HAZs, a very big and a small one, with a total area of 1836.94 mm^2 and total circumference of 111.44 mm; helical pattern generates 4 different HAZs; however, the total area is significantly smaller than rastering pattern and it equals to 771.23 mm^2, which is more than twice as small. The total circumference of these zones is 199.83 mm, which is bigger than the previous pattern. Tessellation pattern also generates four HAZs with a total area of 2023.41 mm^2 and total circumference of 314.84 mm. The ratio of area to circumference for these three patterns is 16.48, 3.85, and 6.42. This information shows that rastering pattern is not a good choice to print this geometry because it not only generates a large HAZ with a big ratio of area to circumference but it also generates a non-uniform temperature distribution with a significant temperature gradient between left and right-hand side of the printing layer. The helical pattern shows some very good results; it generates the smallest

```
    ------------------------------------------------------------
B. SPECIFICATIONS OF CURRENT LAYER:

    Connectivity    ImageSize     NumObjects              PixelIdxList
    ____________    __________    __________
_________________________________

    4               319    320    2              [7991x1 double]
[343x1 double]


    ------------------------------------------------------------
C. CENTER OF HAZs:

x1 =     101.30 (mm)
y1 =     75.78 (mm)

x2 =     125.16 (mm)
y2 =     81.43 (mm)


    ------------------------------------------------------------
D. DISTANCE BETWEEN HAZs:

DISTANCE BETWEEN     1 & 2    =    24.51 (mm)

    ------------------------------------------------------------
E. HAZs CIRCUMFERENCE:

Circum.1 =   51.72 (mm)
Circum.2 =   59.72 (mm)

    ------------------------------------------------------------
F. HAZs AREA:

Area.1 =     1761.34 (mm^2)
Area.2 =     75.60 (mm^2)
Total HAZ Area =     1836.94 (mm^2)

    ------------------------------------------------------------
```

Figure 4.41. The specifications for the detected HAZ in the rastering pattern

total area of HAZs with the smallest ratio of area to circumference, which facilitates heat dissipation from HAZs. Tessellation pattern generates the largest HAZ; however, the ratio of area to circumference is small. A comparison of the temperature

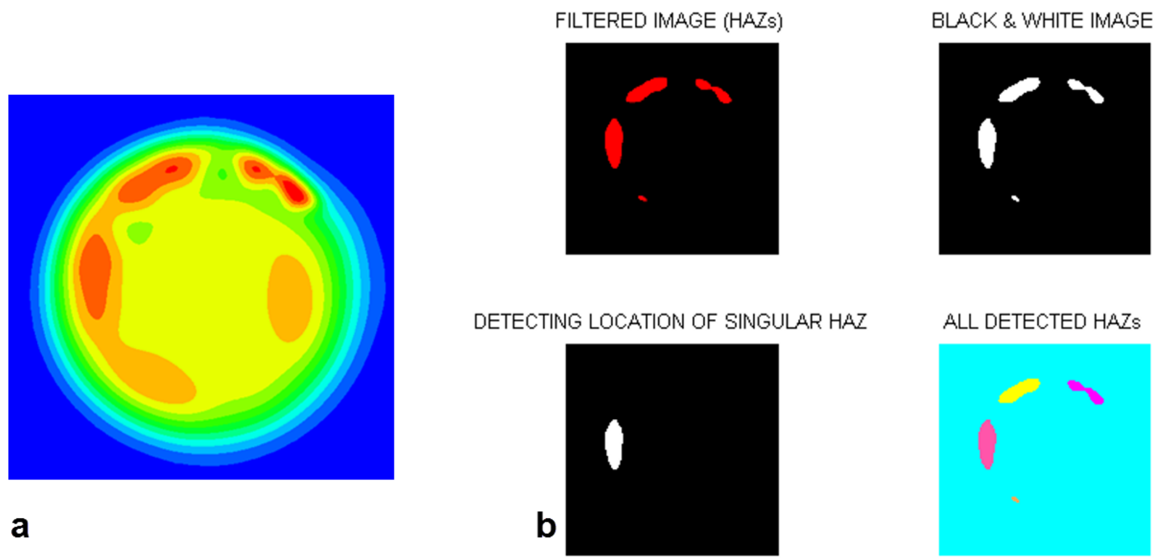

Figure 4.42. a. Temperature distribution, b. detected HAZ in the helical pattern

distribution in Fig. 4.42 and Fig. 4.45 indicates the different ways in which the helical pattern and tessellation pattern affect the printing layer. These figures show that the temperature uniformity throughout the layer printed by tessellation pattern is higher than the helical pattern; hence, we expect better mechanical properties and less thermal defects such as balling phenomena for the layer printed by helical pattern; while, we expect more accurate geometry and smaller warping for the layer printed by tessellation pattern.

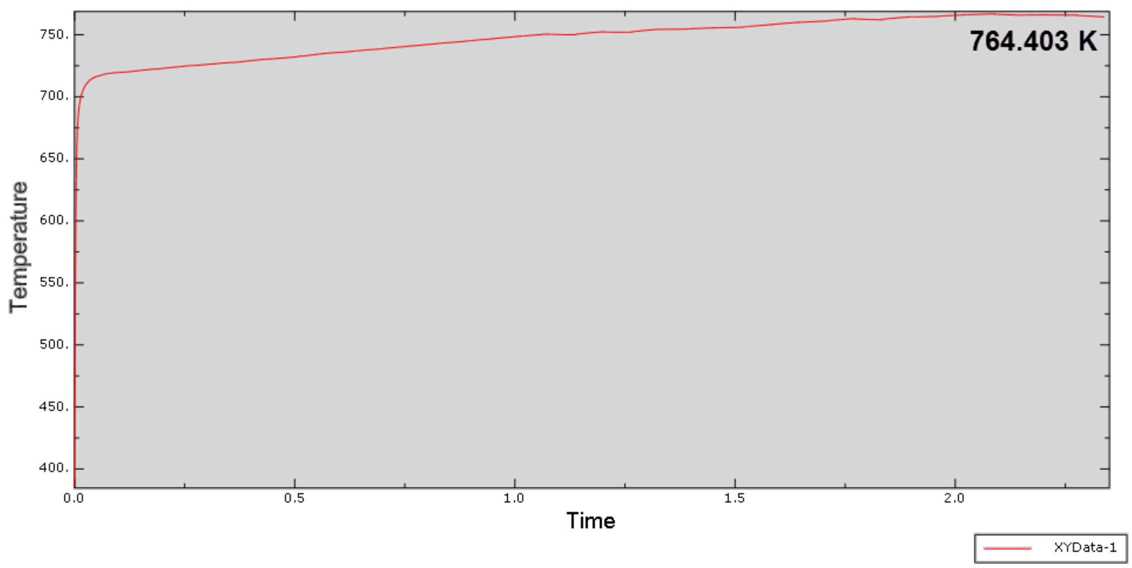

Figure 4.43. The average temperature profile of the entire layer printed by helical pattern

```
    ============================================================
B. SPECIFICATIONS OF CURRENT LAYER:

    Connectivity     ImageSize      NumObjects     PixelIdxList
    ____________     __________     __________     ____________

    4                319    320     4              [1x4 cell]


    ============================================================
C. CENTER OF HAZs:

x1 =      34.30  (mm)
y1 =      70.99  (mm)

x2 =      57.13  (mm)
y2 =      33.44  (mm)

x3 =      54.62  (mm)
y3 =      110.68  (mm)

x4 =      104.75  (mm)
y4 =      34.26  (mm)


    ============================================================
D. DISTANCE BETWEEN HAZs:

DISTANCE BETWEEN     1 & 2    =    43.95  (mm)
DISTANCE BETWEEN     1 & 3    =    44.58  (mm)
DISTANCE BETWEEN     1 & 4    =    79.45  (mm)
DISTANCE BETWEEN     2 & 3    =    77.28  (mm)
DISTANCE BETWEEN     2 & 4    =    47.63  (mm)
DISTANCE BETWEEN     3 & 4    =    91.40  (mm)

    ============================================================
E. HAZs CIRCUMFERENCE:

Circum.1 =    17.40  (mm)
Circum.2 =    47.96  (mm)
Circum.3 =    54.54  (mm)
Circum.4 =    79.93  (mm)

    ============================================================
F. HAZs AREA:

Area.1 =      333.93  (mm^2)
Area.2 =      270.23  (mm^2)
Area.3 =      14.77  (mm^2)
Area.4 =      152.31  (mm^2)
Total HAZ Area =     771.23  (mm^2)
```

Figure 4.44. The specifications for the detected HAZ in the helical pattern

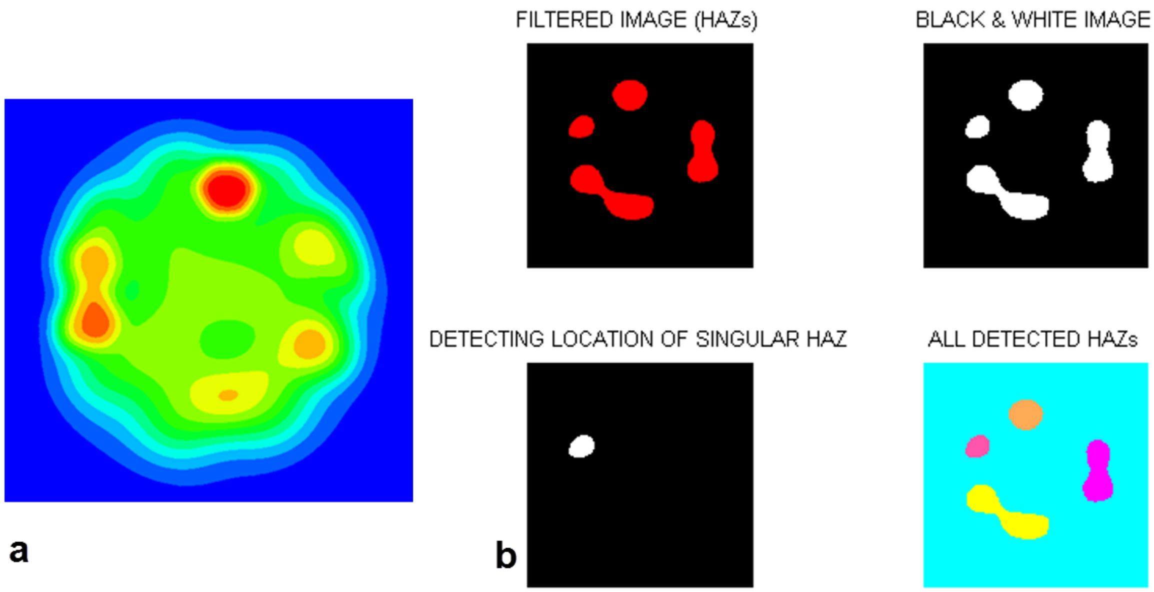

Figure 4.45. Temperature distribution, b. detected HAZ in the tessellation pattern

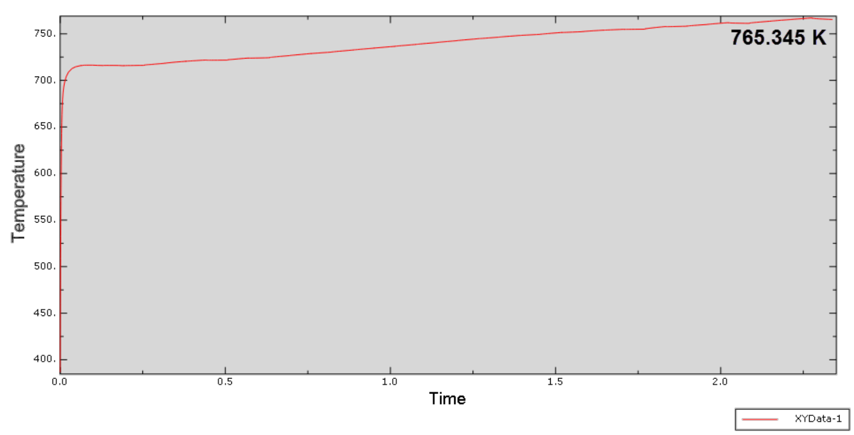

Figure 4.46. The average temperature profile of the entire layer printed by tessellation pattern

```
    ================================================================
B. SPECIFICATIONS OF CURRENT LAYER:

    Connectivity     ImageSize       NumObjects       PixelIdxList
    ____________     __________      __________       ____________

    4                319     320     4                [1x4 cell]


    ================================================================
C. CENTER OF HAZs:

x1 =      36.53 (mm)
y1 =      56.30 (mm)

x2 =      56.10 (mm)
y2 =      101.44 (mm)

x3 =      68.56 (mm)
y3 =      34.83 (mm)

x4 =      116.68 (mm)
y4 =      73.72 (mm)


    ================================================================
D. DISTANCE BETWEEN HAZs:

DISTANCE BETWEEN     1 & 2    =    49.21 (mm)
DISTANCE BETWEEN     1 & 3    =    38.56 (mm)
DISTANCE BETWEEN     1 & 4    =    82.02 (mm)
DISTANCE BETWEEN     2 & 3    =    67.77 (mm)
DISTANCE BETWEEN     2 & 4    =    66.62 (mm)
DISTANCE BETWEEN     3 & 4    =    61.87 (mm)

    ================================================================
E. HAZs CIRCUMFERENCE:

Circum.1 =    18.34 (mm)
Circum.2 =    73.82 (mm)
Circum.3 =    97.33 (mm)
Circum.4 =    125.55 (mm)

    ================================================================
F. HAZs AREA:

Area.1 =      198.15 (mm^2)
Area.2 =      849.70 (mm^2)
Area.3 =      368.53 (mm^2)
Area.4 =      607.02 (mm^2)
Total HAZ Area =      2023.41 (mm^2)
```

Figure 4.47. The specifications for the detected HAZ in the tessellation pattern

5. ONGOING RESEARCH AND CONCLUSIONS

5.1 Employment of IR thermography to validate the simulation technique

However, the developed technique shows the expected temperature value and depth of melt pool precisely, it needs to validate experimentally. To validate the technique, the thermography methodology will monitor a printed sample identical to a simulated specimen with rectangular islands; the previous chapter simulates the designed specimen with the hexagonal island because the previous investigations show the positive influence of hexagonal islands on the microstructure and bonding between layers. However, the current chessboard strategy employs rectangular islands. The simulation technique can leverage a simulation with rectangular islands to investigate the effects of the shape of an island on the temperature distribution of the printed layer. The comparison of temperature distribution generated by the monitoring methodology and simulation will depict the precision of the simulation technique.

5.2 Introduction

The future objective is to develop a practical hybrid closed-loop feedback control algorithm to generate the most possible uniform temperature distribution layer by layer within a specific temperature range. This control algorithm aims to first, employ the acquired monitoring information to adjust the objective process parameters real-time in the powder-bed fusion process. Second, certify the quality of the fabricated part layer by layer. Third, combine offline algorithms such as the designed tessellation algorithm and real-time smart decision-making algorithms such as ANN to modify the process parameters. Forth, modify the scan strategy real-time to generate the most possible uniform temperature distribution and remove thermal abnormalities as the ultimate objective of the project. Fig. 5.1 shows how these steps correlate with each other. We also need to validate the control strategy with completing our open-source open-structure 3D printer. Previous chapters show the results for testing the online monitoring algorithm in the FDM process. It detects the HAZs and reveals their specifications. Powder-bed fusion process employs the exact same algorithm to evaluate the temperature distribution and the thermal characteristic of printed layers. Completing the second objective needs preparation of some benchmarks to evaluate the quality of fabricated layers. For instance, it can use temperature distribution and HAZs specifications throughout each layer to evaluate the thermal evolution of the process. Following sections explain how we can achieve the reminded objectives.

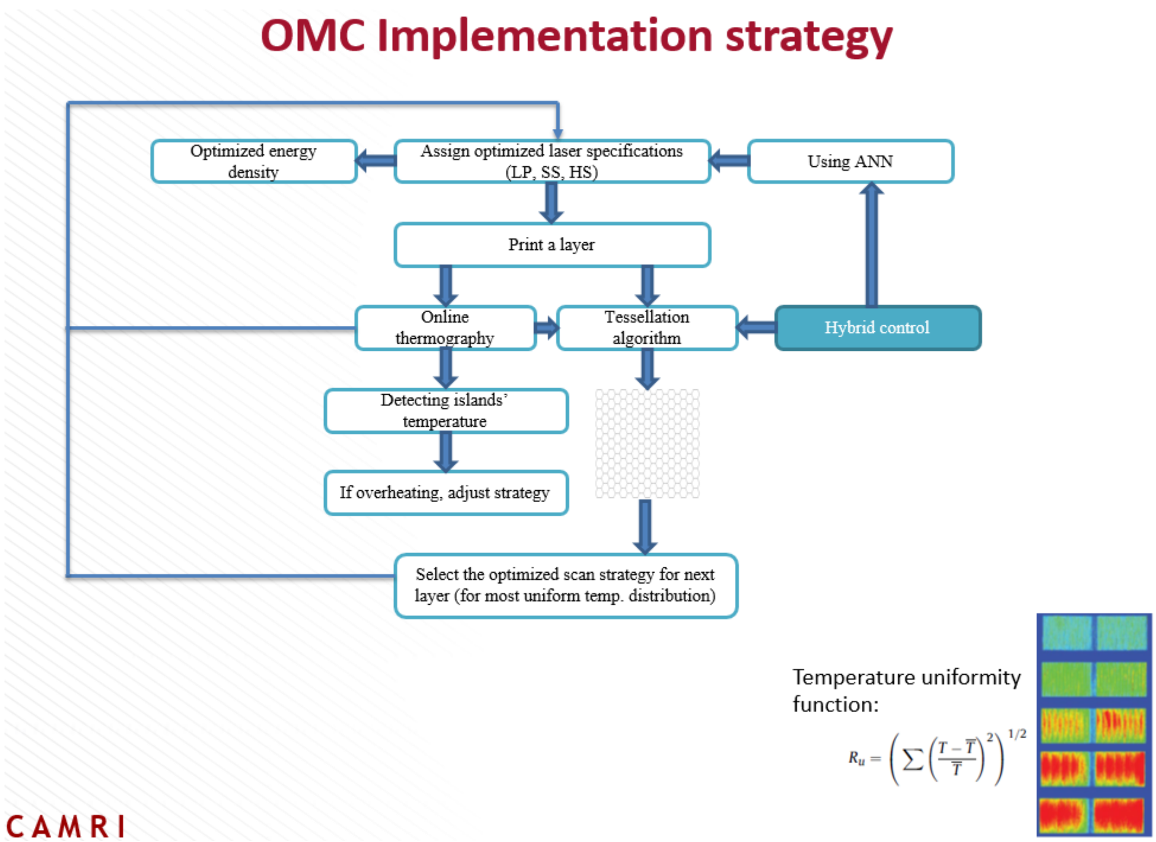

Figure 5.1. Online monitoring and control strategy

5.3 Modification of scan strategy by a hybrid closed-loop feedback control algorithm

The recommended control strategy combines the introduced online monitoring algorithm, the tessellation algorithm, and ANN to achieve the aforementioned objectives. Tessellation scanning strategy is an approach to specify the printing order of different thermal zones in a layer with a complex geometry or long dimensions as well as the printing order of the islands inside the thermal zones. Previous chapters explained these steps thoroughly. Employment of online monitoring helps in three ways. First, it detects the thermal zones and their specifications and sends to the tessellation algorithm. Second, it measures the average temperature of each thermal zone to the ANN function to modify the scan speed and third, it derives the ration of temperature uniformity, which can certify the efficiency of employed scan strategy for each layer.

5.4 Modification of scan speed by Artificial Neural Network

A significant number of industries have been employed ANN successfully in different cases. ANN techniques are especially efficient for non-linear and time-dependent cases with complex nature and without a robust and accurate model. ANN techniques are widely used for system modeling, function optimizing, image processing, and intelligent control. ANNs correlates the input(s) and output(s) implicitly by learning from a data set that represents the behavior of a system [205]. The processing time, mechanical properties, microstructure, geometric accuracy, and surface roughness are five important fields of interest in powder-bed fusion process to the manufacturers. Controlling of thermal aspects of the process helps to improve all these aspects except the fabrication time, which is not a concern in this project. Controlling the energy density helps to avoid overheat zones and balling phenomena. Moreover, it helps to stabilize microstructure and generate isotropic grain size [206]. Adjusting the scan speed is the easiest, fastest, and the most efficient way to control the energy density. Thus, ANN trains a function to optimize the scan speed for each thermal zone according to its temperature. As Fig. 5.2 shows, the algorithm uses scan speed and temperature distribution of the previous layer as inputs and temperature uniformity of the current layer, microstructure, and mechanical properties of the fabricated sample as the outputs to train the function. Training the function needs different experiments with various boundary conditions to cover the thermal zones with all the possible boundary conditions.

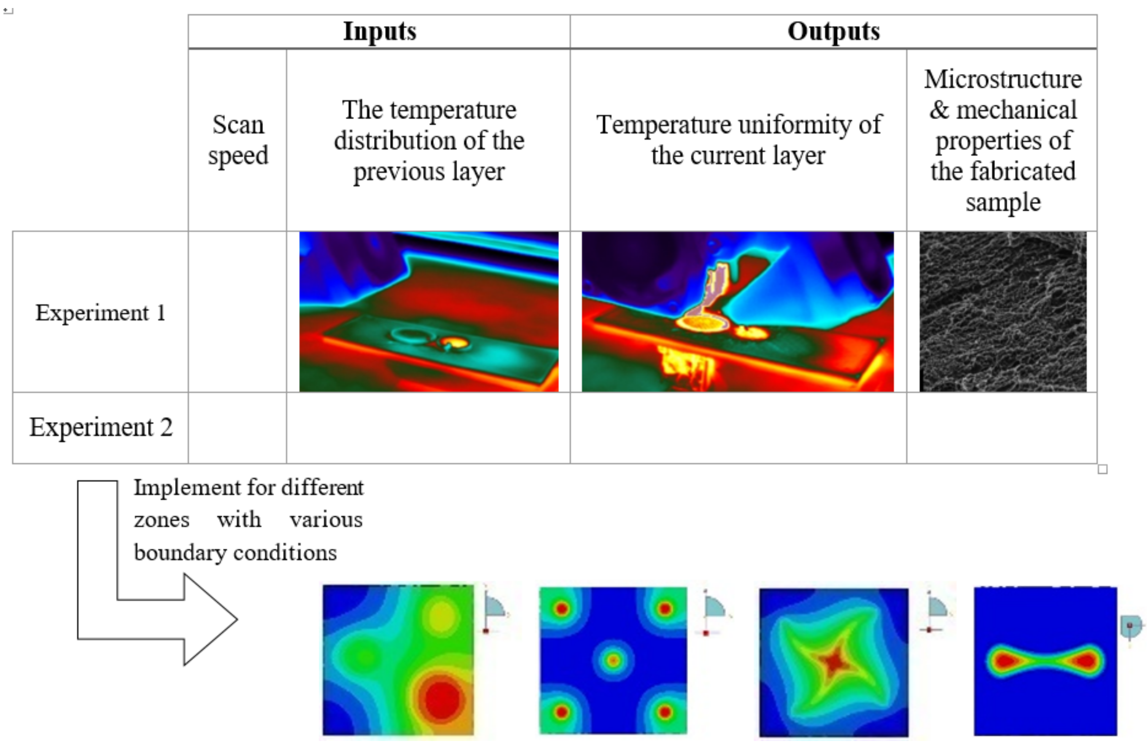

Figure 5.2. Printed specimens with different geometrical features

5.4.1 Design of experiments

Data acquisition is a necessary step to train the ANN algorithm. Our primary simulations show that boundary conditions affect significantly the temperature distribution of a printing area. The algorithm needs the temperature distribution and resulting microstructure of a limited number of printing islands with different boundary conditions and nine different scan speeds (80%, 85%, 90%, 95%, 100%, 105%, 110%, 115%, and 120% of the standard scan speed for a chosen material) to train the algorithm. Fig. 5.3 shows the different statuses and boundary conditions for printing islands/zones that need to train the ANN algorithm. First, we print each sample individually and then, we print the samples all together for each scan speed. The height of each sample equals to 2 mm and the layer thickness equals to 30 um. Thus, the total number of experiments will be [(10x9x66) + (9x66)], which is equal to 6534 experiments. Table 5.1 shows the request summary for this phase. Our primary simulations in Fig. 3.4 show that the size, number, the ratio of the area of a zone to its circumference, distance from the edges of the layer under fabrication, the distance between zones, and the existence of support structures significantly affect resulted temperature value and temperature distribution of a printing zone.

No.	Name	Sample	No.	Name	Sample
1	Big_ convex		6	A bigger ratio of area to circumference	
2	Big_ concave		7	A smaller ratio of area to circumference (same area size)	
3	Medium_ close		8	Different distance form edge	
4	Medium_ far	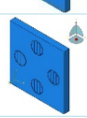	9	Irregular shape_ mix convex and concave	
5	Narrow	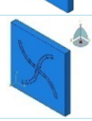	10	Existence of support structure	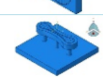

Figure 5.3. Recommended different boundary conditions to print zones for training ANN

Table 5.1.
Summary of requests for ANN phase

No.	Explanation	No. of parts	No. of runs
1	Print each sample with 9 different scan speed	90	90
2	Print all samples together with 9 different scan speed	90	9

5.4.2 Introducing different prospective algorithms

Feed Forward, Back-propagation (BP) Neural Networking

This network is the most widely used optimization procedure based on gradient descent that adjusts the weights to reduce the system error or cost function which is estimated by the total error for all patterns. It uses sigmoid nonlinear transformation functions. BPNN can employ logsigmoid transfer functions in hidden layers and linear transfer function in the output layer [207] especially for online modeling. Fig. 5.4 shows the structures of BPNN include an input layer, hidden layer(s) and an output layer. The weight lines connect each layer to the other layers. The network operation consists of two major phases: The feed-forward phase and the back-propagation phase. A feed forward neural network includes one to two hidden layers and sigmoid activation functions. Twelve popular training algorithms in MATLAB toolbox for feed-forward networks are traingd (Gradient descent), traingdm (Gradient descent with momentum), traingdx (Gradient descent momentum with an adaptive learning rate), trainrp (Resilient BP algorithm), traincgf (Conjugate gradient BP with Fletcher-Reeves updates), traincgp (Conjugate gradient BP with Polak-Ribiere updates), traincgb (Conjugate gradient BP with Powell-Beale restarts), trainscg (Scaled conjugate gradient method), trainbfg (BFGS quasi-Newton method), trainoss (One step secant method), trainlm (Levenberg-Marquardt optimization), and trainbr (Levenberg-Marquardt optimization with Bayesian regularization) [208].

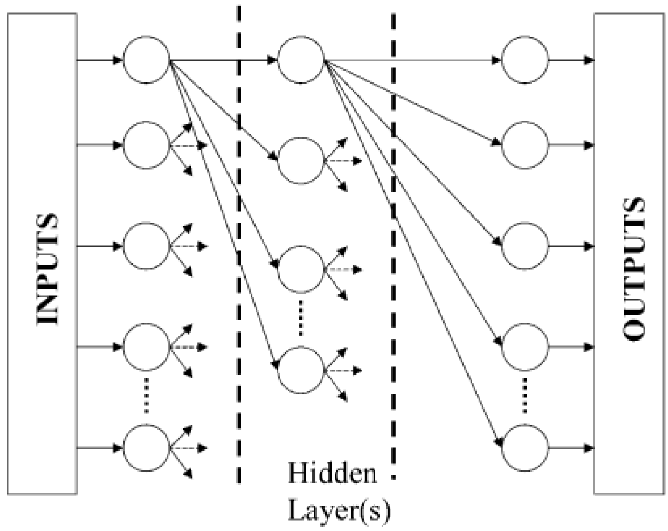

Figure 5.4. Back propagation network topology

Radial basis network (RBN)

This network is a special type of artificial neural networks (ANN), which work well in the field of machining process modeling and simulation. RBN poses a neural network architecture with a feed-forward three-layer fully interconnected neural network (Fig. 5.5) [207, 209]. This network mainly employs Gaussian activation functions for pattern recognition [207] as well as function modeler and representing nonlinear models. One of the most widely used algorithms in BP is the Levenberg-Marquardt technique that has a fast convergence.

Counter Propagation Neural Network (CPNN)

The CPNN is a hybrid network, consisting of an outstar network and competitive filter network. The hidden layer is a Kohonen network, which categorizes the pattern that was input. The output layer is an outstar array, which reproduces the correct output pattern for the category.

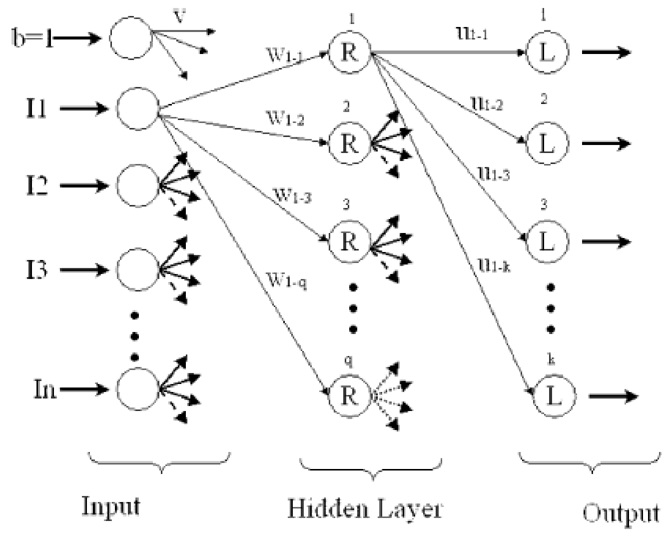

Figure 5.5. Radial basis network architecture

Recurrent Neural Network (RNN)

A recurrent neural network (RNN) is a class of artificial neural network where connections between units form a directed cycle. This creates an internal state of the network, which allows it to exhibit dynamic temporal behavior. Gao et al. [210] employed recurrent neural networks as an error estimator, an approach based on the Elman network. They showed that the SageHusa AKF algorithm makes a real-time estimation of the noise statistical characteristics. Elman neural network is a typical type of dynamic recurrent neural network proposed by Elman in 1990 [211]. Its memory and feedback characteristics make it applicable to time-varying adaptive control systems [212-215]. As shown in Fig. 5.6, the Elman neural network consists of the context layer, the input layer, hidden layer, and output layer.

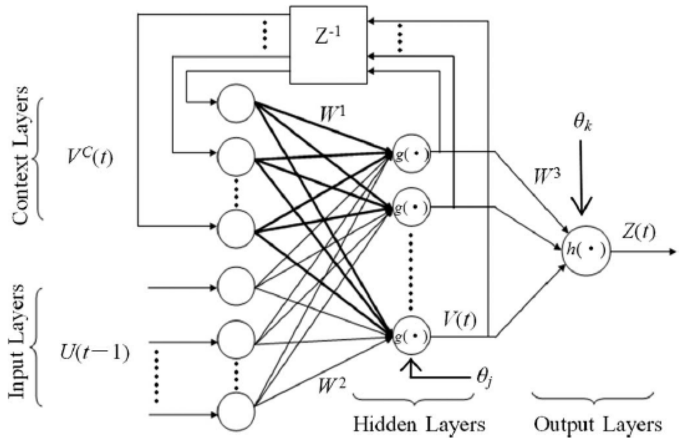

Figure 5.6. Schematic of the Elman recurrent neural network

Different criteria to select a suitable ANN strategy for our control system

RBN works considerably well in function approximation. This network converges very fast compared with back propagation, it has the capability to represent non-linear functions, it does not experience local minima problems of back propagation, and finally, it can be designed in a fraction of the time that it takes to train the BP network [207]. However, it may require more neurons than the standard feed-forward BP networks [207]. Most commonly used RBNs involve fixed basis functions with linearly appearing unknown parameters in the output layer. In contrast, multi-layer BP ANNs involve adjustable basis functions. That result in nonlinearly appearing unknown parameters. It is commonly known that linearity in parameters in RBN allows the use of least squares error based updating schemes that have faster convergence than the gradient-descent methods used to update the nonlinear parameters of multi-layer BP-ANN. On the other hand, it is also known that the use of fixed basis functions in RBN results in exponential complexity in terms of the number of parameters, while adjustable basis functions of BP-ANN can lead to much less complexity in terms of the number of parameters or network size [216]. However, in practice, the number of parameters in RBN starts becoming unmanageably large only when the number of input features increases beyond about 10 or 20. Literature shows that the BPNN took much longer to converge to the specified MGE compared with CPNN (The training time for CPNN was much less than that for BPNN) [208]. Our designed control system has only two inputs however one of them is the temperature distribution of the previously fabricated layer. The control strategy is going to employ all the four aforementioned networks and compare the convergence time and precisions together to choose the most suitable one.

5.5 Experimental validation

5.5.1 Completing the open-structure homemade test-bed

A homemade test-bed designed in CAMRI, modified and optimized as my part of the project, and manufactured in Drinan Racing, Inc (Fig. 5.7). This testbed makes possible to carry out adequate low-cost experiments. These experiments are necessary to optimize the tessellation algorithm and collect adequate data for training the ANN algorithm. The test-bed needs an open source software to control galvanometer by the newly designed control strategies. No company suggests such an open-source software, therefore, a new software is under preparation. This test-bed is open-structure and will let to mount IR camera and other sensors in the desired location for the future research. A high-power laser is in demand to launch the test-bed.

5.5.2 Collaboration with local industries

We communicate with local industries such as third Dimension and 3D parts, military labs, and national labs such as Quad-City Manufacturing Lab in order to carry out the primary experiments, evaluate the introduced online thermography methodology, evaluate the developed simulation technique, and finally train our ANN

Figure 5.7. The homemade test-bed carrying out our experiments

function. It also possible to evaluate the effect of fabrication of topology optimized support structure on temperature distribution and final distortion of fabricated parts.

5.5.3 Print artifact to identify/measure defects and process limitations in current industrial machines

Achieving desired mechanical properties, repeatability, and zero post processing are the three most important challenges in SLS and SLM process especially in mass production. An efficient monitoring and control strategy facilitate reaching these demands. National Institute of Standards and Technology (NIST) and TUSAS Engine Industries, Inc. [217] introduces some standard artifacts with special features to measure the defects and process limitations (Fig. 5.8) [21, 217, 218]. These artifacts may help to measure the capabilities and limitations of the developed control strategy such as executive time, precision, efficiency for different geometries, etc. Furthermore, we can compare the accuracy of geometrical features, dimensional accuracy, surface condition, improvement in mechanical properties, and microstructure of the fabricated part [59], with and without the control strategy.

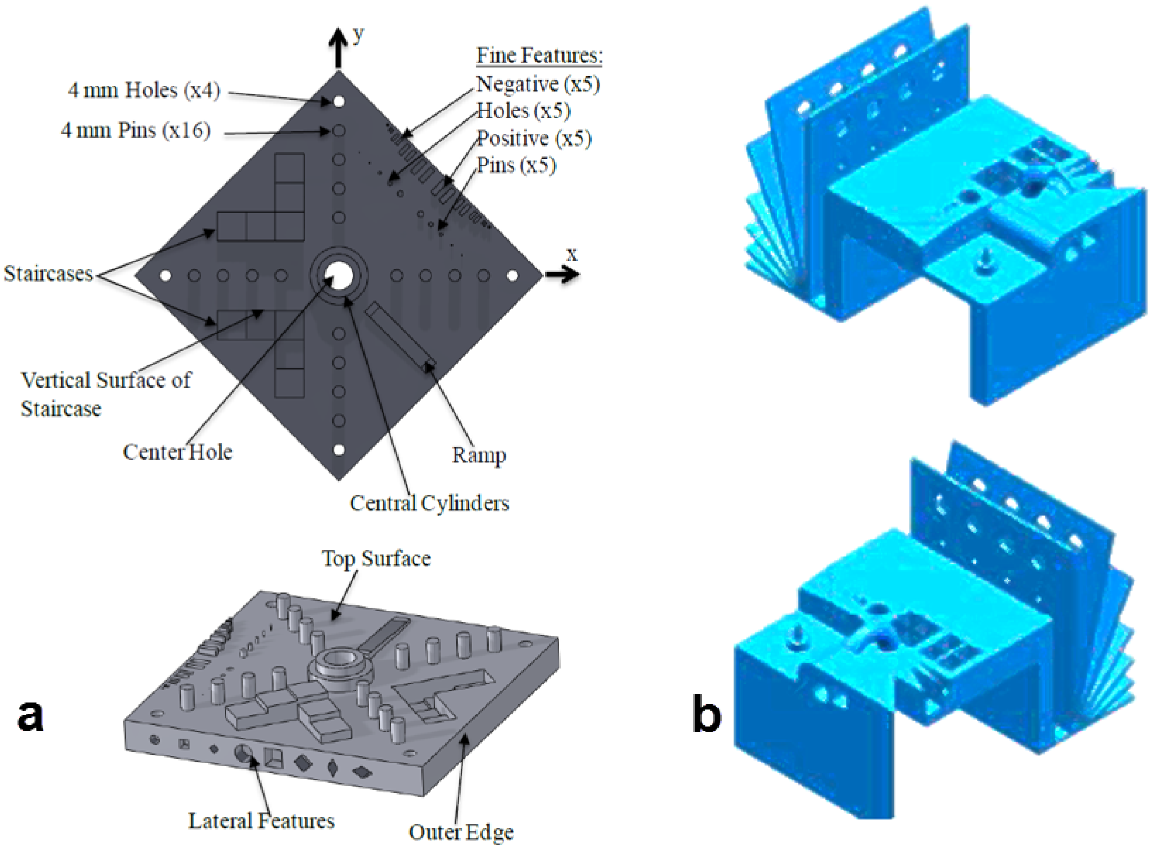

Figure 5.8. a. The artifact designed by NIST and b. The artifact designed by TUSAS engine industries

5.6 Conclusions

This work describes the most common defects and their contributing parameters in powder-bed fusion AM process. It classifies the defects for online process monitoring as well as the development of control and error handling strategies. Furthermore, it classifies process parameters into pre-defined, controllable and post-process ones, and recommends the main parameters for control strategies. Our study shows that thermal defects represent the main portion of the manufacturing abnormalities, which significantly reduces repeatability, precision, and ultimate mechanical and surface quality of fabricated parts. The temperature distribution is a significant proxy to optimize process parameters and elevate the ultimate quality of the fabricated part. This work introduces a novel online thermography approach based on an image segmentation algorithm in MATLAB to detect the HAZs and present their specifications. It also evaluates the thermal evolution and behavior of any thermal inherent AM fabrication process. Moreover, this work develops a new technique in ABAQUS to simulate temperature distribution in the powder-bed fusion process in a fraction of the time taken by current methods in the literature. This technique simulates different printing patterns including a novel layer-based methodology, called tessellation algorithm/pattern to elevate temperature uniformity in a layer with complex geometry or long dimensions. Ongoing research will complete a hybrid closed-loop online monitoring and control methodology to modify scan strategy real-time with a combination of the tessellation algorithm, online thermography, and Artificial Neural Networking (ANN). This methodology aims to generate the most uniform temperature distribution within a safe temperature range layer-by-layer according to the geometry and thermal history of each layer. The ANN algorithm will adjust scan speed according to the resulted process signature, namely, temperature distribution and energy density to avoid some prevalent thermal abnormalities such as balling phenomena. This strategy will improve the current 3D printers to minimize the current major process defects, elevate repeatability, mechanical properties, and ultimate part quality.

REFERENCES

REFERENCES

[1] D. Gu, W. Meiners, K. Wissenbach, and R. Poprawe, "Laser additive manufacturing of metallic components: materials, processes and mechanisms," *International Materials Reviews*, vol. 57, pp. 133-164, 2012.

[2] V. Bhavar, P. Kattire, V. Patil, S. Khot, K. Gujar, and R. Singh, "A Review on Powder Bed Fusion Technology of Metal Additive Manufacturing," *in International Conference & Exhibition on Additive Manufacturing Technologies Bangalore*, India, 2015.

[3] W. E. Frazier, "Metal additive manufacturing: a review," *Journal of Materials Engineering and Performance*, vol. 23, pp. 1917-1928, 2014.

[4] J. Ruan, T. E. Sparks, Z. Fan, J. K. Stroble, A. Panackal, and F. Liou, "A review of layer based manufacturing processes for metals," *in 17th Solid Freeform Fabrication Symposium*, Austin (USA), 2006, pp. 233-245.

[5] K. V. Wong and A. Hernandez, "A review of additive manufacturing," *ISRN Mechanical Engineering*, vol. 2012, 2012.

[6] P. Kulkarni, A. Marsan, and D. Dutta, "A review of process planning techniques in layered manufacturing," *Rapid Prototyping Journal*, vol. 6, pp. 18-35, 2000.

[7] X. Gong, T. Anderson, and K. Chou, "Review on powder-based electron beam additive manufacturing technology," *in ASME/ISCIE 2012 International Symposium on Flexible Automation*, 2012, pp. 507-515.

[8] V. Despa and I. Gheorghe, "Study of selective laser sintering: a qualitative and objective approach," *Scientific Bulletin of Valahia University Materials and Mechanics*, vol. 6, pp. 150-155, 2011.

[9] H. Meier and C. Haberland, "Experimental studies on selective laser melting of metallic parts," *Materialwissenschaft und Werkstofftechnik*, vol. 39, pp. 665-670, 2008.

[10] K. Abd-Elghany and D. Bourell, "Property evaluation of 304L stainless steel fabricated by selective laser melting," *Rapid Prototyping Journal*, vol. 18, pp. 420-428, 2012.

[11] S. Storch, D. Nellessen, G. Schaefer, and R. Reiter, "Selective laser sintering: qualifying analysis of metal based powder systems for automotive applications," *Rapid Prototyping Journal*, vol. 9, pp. 240-251, 2003.

[12] G. Tapia and A. Elwany, "A review on process monitoring and control in metal-based additive manufacturing," *Journal of Manufacturing Science and Engineering*, vol. 136, p. 060801, 2014.

[13] Wohlers Associates, Wohlers Report 2017, 2017, Retrieved from *https://wohlersassociates.com*

[14] E. Malekipour and H. El-Mounayri, "Common Defects and Contributing Parameters in Powder-based AM Process and Their Classification for Online Monitoring: A Review," *The International Journal of Advanced Manufacturing Technology*, pp. 1-42, 2016.

[15] T. Craeghs, S. Clijsters, J.-P. Kruth, F. Bechmann, and M.-C. Ebert, "Detection of process failures in layerwise laser melting with optical process monitoring," *Physics Procedia*, vol. 39, pp. 753-759, 2012.

[16] K. Zeng, D. Pal, and B. Stucker, "A review of thermal analysis methods in laser sintering and selective laser melting," *in Proceedings of Solid Freeform Fabrication Symposium Austin*, TX, 2012.

[17] S. K. Tiwari, S. Pande, S. Agrawal, and S. M. Bobade, "Selection of selective laser sintering materials for different applications," *Rapid Prototyping Journal*, vol. 21, pp. 630-648, 2015.

[18] H. Wenbin, L. Yong Tsui, and G. Haiqing, "A study of the staircase effect induced by material shrinkage in rapid prototyping," *Rapid Prototyping Journal*, vol. 11, pp. 82-89, 2005.

[19] S. Bhatia, "Effect of Machine Positional Errors on Geometric Tolerances in Additive Manufacturing," *M.Sc. Thesis, University of Cincinnati*, 2014.

[20] A. Barari, "Effect of Direct Slicing on Geometric Tolerances in Additive Manufacturing Process." *Proceedings - ASPE Spring Topical Meeting*, Ontario, Canada, pp. 145-146, 2014.

[21] S. Moylan, J. Slotwinski, A. Cooke, K. Jurrens, and M. A. Donmez, "Proposal for a standardized test artifact for additive manufacturing machines and processes," *in 23rd Annual International Solid Freeform Fabrication Symposium*, Austin, TX, 2012, pp. 902-920.

[22] C. Hauser, "Selective laser sintering of a stainless steel powder," *Ph.D. Thesis, University of Leeds*, 2003.

[23] H. Zhu, L. Lu, and J. Fuh, "Study on shrinkage behaviour of direct laser sintering metallic powder," *Proceedings of the Institution of Mechanical Engineers, Part B: Journal of Engineering Manufacture*, vol. 220, pp. 183-190, 2006.

[24] Y. Ning, Y. Wong, J. Y. Fuh, and H. T. Loh, "An approach to minimize build errors in direct metal laser sintering," *IEEE Transactions on Automation Science and Engineering*, vol. 3, pp. 73-80, 2006.

[25] R. Paul, "Modeling and optimization of powder based additive manufacturing (AM) processes," *Ph.D. Thesis, University of Cincinnati*, 2013.

[26] P. K. Venuvinod and W. Ma, Rapid prototyping: laser-based and other technologies: *Springer Science & Business Media*, 2013.

[27] X. Wang, "Calibration of shrinkage and beam offset in SLS process," *Rapid Prototyping Journal*, vol. 5, pp. 129-133, 1999.

[28] Y. Shi, Z. Li, H. Sun, S. Huang, and F. Zeng, "Effect of the properties of the polymer materials on the quality of selective laser sintering parts," *Proceedings of the Institution of Mechanical Engineers, Part L: Journal of Materials Design and Applications*, vol. 218, pp. 247-252, 2004.

[29] R.-J. Wang, L. Wang, L. Zhao, and Z. Liu, "Influence of process parameters on part shrinkage in SLS," *The International Journal of Advanced Manufacturing Technology*, vol. 33, pp. 498-504, 2007.

[30] S. Kumar, "Selective laser sintering: a qualitative and objective approach," *Jom*, vol. 55, pp. 43-47, 2003.

[31] N. Hopkinson and T. B. Sercombe, "Process repeatability and sources of error in indirect SLS of aluminium," *Rapid Prototyping Journal*, vol. 14, pp. 108-113, 2008.

[32] N. Raghunath and P. M. Pandey, "Improving accuracy through shrinkage modelling by using Taguchi method in selective laser sintering," *International Journal of Machine Tools and Manufacture*, vol. 47, pp. 985-995, 2007.

[33] Y. Ning, Y. Wong, and J. Fuh, "Effect and control of hatch length on material properties in the direct metal laser sintering process," *Proceedings of the Institution of Mechanical Engineers, Part B: Journal of Engineering Manufacture*, vol. 219, pp. 15-25, 2005.

[34] K. Senthilkumaran, P. M. Pandey, and P. Rao, "Influence of building strategies on the accuracy of parts in selective laser sintering," *Materials & Design*, vol. 30, pp. 2946-2954, 2009.

[35] A. Simchi, F. Petzoldt, and H. Pohl, "On the development of direct metal laser sintering for rapid tooling," *Journal of Materials Processing Technology*, vol. 141, pp. 319-328, 2003.

[36] Y. Wang, J. Bergstrm, and C. Burman, "Characterization of an iron-based laser sintered material," *Journal of Materials Processing Technology*, vol. 172, pp. 77-87, 2006.

[37] J. Delgado, J. Ciurana, and C. A. Rodrguez, "Influence of process parameters on part quality and mechanical properties for DMLS and SLM with iron-based materials," *The International Journal of Advanced Manufacturing Technology*, vol. 60, pp. 601-610, 2012.

[38] P. Das, R. Chandran, R. Samant, and S. Anand, "Optimum Part Build Orientation in Additive Manufacturing for Minimizing Part Errors and Support Structures," *Procedia Manufacturing*, vol. 1, pp. 343-354, 2015.

[39] M. Badrossamay and T. Childs, "Layer formation studies in selective laser melting of steel powders," *in Proc. SFF Symp.*, Austin, Texas, USA, 2006, pp. 268-279.

[40] R. Morgan, C. Sutcliffe, and W. O'Neill, "Experimental investigation of nanosecond pulsed Nd: YAG laser re-melted pre-placed powder beds," *Rapid Prototyping Journal*, vol. 7, pp. 159-172, 2001.

[41] B. Xiao and Y. Zhang, "Laser sintering of metal powders on top of sintered layers under multiple-line laser scanning," *Journal of Physics D: Applied Physics*, vol. 40, p. 6725, 2007.

[42] M. GC and P. Krishna, "Effect of Process Parameters on Surface Roughness of Laser Processed Inconel Superalloy," *International Journal of Scientific & Engineering Research*, Vol. 5, Issue 8, pp. 232-236, 2014.

[43] F. Calignano, D. Manfredi, E. Ambrosio, L. Iuliano, and P. Fino, "Influence of process parameters on surface roughness of aluminum parts produced by DMLS," *The International Journal of Advanced Manufacturing Technology*, vol. 67, pp. 2743-2751, 2013.

[44] J.-P. Kruth, E. Yasa, and J. Deckers, "Roughness improvement in selective laser melting," *in Proceedings of the 3rd International Conference on Polymers and Moulds Innovations*, 2008, pp. 170-183.

[45] E. Yasa and J.-P. Kruth, "Microstructural investigation of Selective Laser Melting 316L stainless steel parts exposed to laser re-melting," *Procedia Engineering*, vol. 19, pp. 389-395, 2011.

[46] W. Aiyiti, W. Zhao, B. Lu, and Y. Tang, "Investigation of the overlapping parameters of MPAW-based rapid prototyping," *Rapid Prototyping Journal*, vol. 12, pp. 165-172, 2006.

[47] D. Gu and Y. Shen, "Effects of processing parameters on consolidation and microstructure of WCu components by DMLS," *Journal of Alloys and Compounds*, vol. 473, pp. 107-115, 2009.

[48] M. Krishnan, E. Atzeni, R. Canali, F. Calignano, D. Manfredi, E. P. Ambrosio, et al., "On the effect of process parameters on properties of AlSi10Mg parts produced by DMLS," *Rapid Prototyping Journal*, vol. 20, pp. 449-458, 2014.

[49] S. Kleszczynski, J. Zur Jacobsmhlen, J. Sehrt, and G. Witt, "Error detection in laser beam melting systems by high resolution imaging," *in Proceedings of the Solid Freeform Fabrication Symposium*, 2012.

[50] E. Yasa, J. Deckers, T. Craeghs, M. Badrossamay, and J.-P. Kruth, "Investigation on occurrence of elevated edges in selective laser melting," *in International Solid Freeform Fabrication Symposium*, Austin, TX, USA, 2009, pp. 673-85.

[51] A. J. Pinkerton and L. Li, "The effect of laser pulse width on multiple-layer 316L steel clad microstructure and surface finish," *Applied Surface Science*, vol. 208, pp. 411-416, 2003.

[52] R. Li, J. Liu, Y. Shi, L. Wang, and W. Jiang, "Balling behavior of stainless steel and nickel powder during selective laser melting process," *The International Journal of Advanced Manufacturing Technology*, vol. 59, pp. 1025-1035, 2012.

[53] A. Spierings, N. Herres, and G. Levy, "Influence of the particle size distribution on surface quality and mechanical properties in AM steel parts," *Rapid Prototyping Journal*, vol. 17, pp. 195-202, 2011.

[54] A. Cooke and J. Slotwinski, Properties of metal powders for additive manufacturing: a review of the state of the art of metal powder property testing: US Department of Commerce, *National Institute of Standards and Technology*, 2012.

[55] A. Amado, M. Schmid, G. Levy, and K. Wegener, “Advances in SLS powder characterization,” *Group*, vol. 7, pp. 438-452, 2011.

[56] A. Simchi, “The role of particle size on the laser sintering of iron powder,” *Metallurgical and Materials Transactions B*, vol. 35, pp. 937-948, 2004.

[57] H. Gong, K. Rafi, H. Gu, T. Starr, and B. Stucker, “Analysis of defect generation in Ti6Al4V parts made using powder bed fusion additive manufacturing processes,” *Additive Manufacturing*, vol. 1, pp. 87-98, 2014.

[58] D. Gu and Y. Shen, “Balling phenomena in direct laser sintering of stainless steel powder: metallurgical mechanisms and control methods,” *Materials & Design*, vol. 30, pp. 2903-2910, 2009.

[59] S. L. Campanelli, A. Angelastro, A. D. Ludovico, and N. Contuzzi, Capabilities and performances of the selective laser melting process: *INTECH Open Access Publisher*, 2010.

[60] M. Islam, T. Purtonen, H. Piili, A. Salminen, and O. Nyrhil, “Temperature profile and imaging analysis of laser additive manufacturing of stainless steel,” *Physics Procedia*, vol. 41, pp. 835-842, 2013.

[61] K. Mumtaz and N. Hopkinson, “Selective laser melting of thin wall parts using pulse shaping,” *Journal of Materials Processing Technology*, vol. 210, pp. 279-287, 2010.

[62] J. Cherry, H. Davies, S. Mehmood, N. Lavery, S. Brown, and J. Sienz, “Investigation into the effect of process parameters on microstructural and physical properties of 316L stainless steel parts by selective laser melting,” *The International Journal of Advanced Manufacturing Technology*, vol. 76, pp. 869-879, 2015.

[63] S. Das, “Physical aspects of process control in selective laser sintering of metals,” *Advanced Engineering Materials*, vol. 5, pp. 701-711, 2003.

[64] Y. Li and D. Gu, “Thermal behavior during selective laser melting of commercially pure titanium powder: Numerical simulation and experimental study,” *Additive Manufacturing*, vol. 1, pp. 99-109, 2014.

[65] N. T. Aboulkhair, N. M. Everitt, I. Ashcroft, and C. Tuck, "Reducing porosity in AlSi10Mg parts processed by selective laser melting," *Additive Manufacturing*, vol. 1, pp. 77-86, 2014.

[66] R. Paul, S. Anand, and F. Gerner, "Effect of thermal deformation on part errors in metal powder based additive manufacturing processes," *Journal of Manufacturing Science and Engineering*, vol. 136, p. 031009, 2014.

[67] M. F. Zaeh and G. Branner, "Investigations on residual stresses and deformations in selective laser melting," *Production Engineering*, vol. 4, pp. 35-45, 2010.

[68] E. R. Denlinger, J. C. Heigel, P. Michaleris, and T. Palmer, "Effect of inter-layer dwell time on distortion and residual stress in additive manufacturing of titanium and nickel alloys," *Journal of Materials Processing Technology*, vol. 215, pp. 123-131, 2015.

[69] I. A. Roberts, "Investigation of residual stresses in the laser melting of metal powders in additive layer manufacturing," *Ph.D. Thesis, University of Wolverhampton*, 2012.

[70] B. Cheng and K. Chou, "Thermal Stresses Associated with Part Overhang Geometry in Electron Beam Additive Manufacturing: Process Parameter Effects," *in 25th Annual International Solid Freeform Fabrication Symposium-An Additive Manufacturing Conference*, Austin, TX, USA, 2014.

[71] B. Cheng and K. Chou, "Thermal stresses associated with part overhang geometry in electron beam additive manufacturing: process parameter effects," *in Proc. Annu. Int. Solid Freeform Fabr. Symp*, 2014, p. 1076.

[72] J.-P. Kruth, G. Levy, F. Klocke, and T. Childs, "Consolidation phenomena in laser and powder-bed based layered manufacturing," *CIRP Annals-Manufacturing Technology*, vol. 56, pp. 730-759, 2007.

[73] K. Zeng, N. Patil, H. Gu, H. Gong, D. Pal, T. Starr, et al., "Layer by layer validation of geometrical accuracy in additive manufacturing processes," *in Proceedings of the Solid Freeform Fabrication Symposium, Austin*, TX, Aug, 2013, pp. 12-14.

[74] N. N'Dri, H. W. Mindt, B. Shula, M. Megahed, A. Peralta, P. Kantzos, et al., "DMLS process modelling & validation," *TMS2015 Supplemental Proceedings*, pp. 389-396, 2015.

[75] H. Asgharzadeh and A. Simchi, "Effect of sintering atmosphere and carbon content on the densification and microstructure of laser-sintered M2 high-speed steel powder," *Materials Science and Engineering: A*, vol. 403, pp. 290-298, 2005.

[76] N. Hrabe and T. Quinn, "Effects of processing on microstructure and mechanical properties of a titanium alloy (Ti6Al4V) fabricated using electron beam melting (EBM), Part 2: Energy input, orientation, and location," *Materials Science and Engineering: A*, vol. 573, pp. 271-277, 2013.

[77] D. Buchbinder, H. Schleifenbaum, S. Heidrich, W. Meiners, and J. Bltmann, "High power selective laser melting (HP SLM) of aluminum parts," *Physics Procedia*, vol. 12, pp. 271-278, 2011.

[78] J. Nelson, G. Galloway, A. Rennie, T. Abram, and G. Bennett, "Effects of scan direction and orientation on mechanical properties of laser sintered polyamide-12," *International Journal of Advanced Design & Manufacturing Technology*, vol. 7, 2014.

[79] M. Vlasea, R. Pilliar, and E. Toyserkani, "Control of structural and mechanical properties in bioceramic bone substitutes via additive manufacturing layer stacking orientation," *Additive Manufacturing*, vol. 6, pp. 30-38, 2015.

[80] A. Ellis, R. Brown, and N. Hopkinson, "The effect of build orientation and surface modification on mechanical properties of high speed sintered parts," *Surface Topography: Metrology and Properties, vol. 3*, p. 034005, 2015.

[81] P. B. Prangnell and J. D. Robson. Predicting Heterogeneity and Defects in Additive Manufacturing, 2011, Retrieved from *//www.latest2.manchester.ac.uk/documents.*

[82] H. D. Carlton, A. Haboub, G. F. Gallegos, D. Y. Parkinson, and A. A. MacDowell, "Damage evolution and failure mechanisms in additively manufactured stainless steel," *Materials Science and Engineering: A*, vol. 651, pp. 406-414, 2016.

[83] H. Gu, H. Gong, D. Pal, K. Rafi, T. Starr, and B. Stucker, "Influences of energy density on porosity and microstructure of selective laser melted 17-4PH stainless steel," *in Proceedings of Solid Freeform Fabrication Symposium*, 2013, pp. 474-479.

[84] D. Gu and Y. Shen, "Processing conditions and microstructural features of porous 316L stainless steel components by DMLS," *Applied Surface Science*, vol. 255, pp. 1880-1887, 2008.

[85] A. Simchi and H. Pohl, "Effects of laser sintering processing parameters on the microstructure and densification of iron powder," *Materials Science and Engineering: A*, vol. 359, pp. 119-128, 2003.

[86] B. Zhang, H. Liao, and C. Coddet, "Effects of processing parameters on properties of selective laser melting Mg9 Al powder mixture," *Materials & Design*, vol. 34, pp. 753-758, 2012.

[87] R. Li, J. Liu, Y. Shi, M. Du, and Z. Xie, "316L stainless steel with gradient porosity fabricated by selective laser melting," *Journal of Materials Engineering and Performance*, vol. 19, pp. 666-671, 2010.

[88] R. Morgan, C. Sutcliffe, and W. O'neill, "Density analysis of direct metal laser re-melted 316L stainless steel cubic primitives," *Journal of Materials Science*, vol. 39, pp. 1195-1205, 2004.

[89] E. Yasa, J. Deckers, and J.-P. Kruth, "The investigation of the influence of laser re-melting on density, surface quality and microstructure of selective laser melting parts," *Rapid Prototyping Journal*, vol. 17, pp. 312-327, 2011.

[90] C. Hauser, T. Childs, C. Taylor, M. Badrossamay, S. Akhtar, C. Wright, et al., "Direct selective laser sintering of tool steel powders to high density, Part A: Effects of laser beam width and scan strategy," *in Proceedings of the 2003 Solid Freeform Fabrication Symposium*, 2003.

[91] V. Beal, P. Erasenthiran, N. Hopkinson, P. Dickens, and C. H. Ahrens, "Scanning strategies and spacing effect on laser fusion of H13 tool steel powder using high power Nd: YAG pulsed laser," *International Journal of Production Research*, vol. 46, pp. 217-232, 2008.

[92] V. Beal, P. Erasenthiran, N. Hopkinson, P. Dickens, and C. Ahrens, "The effect of scanning strategy on laser fusion of functionally graded H13/Cu materials," *The International Journal of Advanced Manufacturing Technology*, vol. 30, pp. 844-852, 2006.

[93] S. Bland and N. T. Aboulkhair, "Reducing porosity in additive manufacturing," Metal Powder Report, vol. 70, pp. 79-81, 2015.

[94] A. Chatterjee, S. Kumar, P. Saha, P. Mishra, and A. R. Choudhury, "An experimental design approach to selective laser sintering of low carbon steel," *Journal of Materials Processing Technology*, vol. 136, pp. 151-157, 2003.

[95] R. Li, Y. Shi, Z. Wang, L. Wang, J. Liu, and W. Jiang, "Densification behavior of gas and water atomized 316L stainless steel powder during selective laser melting," *Applied Surface Science*, vol. 256, pp. 4350-4356, 2010.

[96] K. Murali, A. Chatterjee, P. Saha, R. Palai, S. Kumar, S. Roy, et al., "Direct selective laser sintering of irongraphite powder mixture," *Journal of Materials Processing Technology*, vol. 136, pp. 179-185, 2003.

[97] A. Spierings and G. Levy, “Comparison of density of stainless steel 316L parts produced with selective laser melting using different powder grades,” *in Proceedings of the Annual International Solid Freeform Fabrication Symposium*, 2009, pp. 342-353.

[98] J. Parthasarathy, B. Starly, S. Raman, and A. Christensen, “Mechanical evaluation of porous titanium (Ti6Al4V) structures with electron beam melting (EBM),” *Journal of the Mechanical Behavior of Biomedical Materials*, vol. 3, pp. 249-259, 2010.

[99] A. E. Hawkins, The shape of powder-particle outlines vol. 1: *Taunton: Research Studies Press*, 1993.

[100] M. Yan and P. Yu, “An Overview of Densification, Microstructure and Mechanical Property of Additively Manufactured Ti-6Al-4VComparison among Selective Laser Melting, Electron Beam Melting, Laser Metal Deposition and Selective Laser Sintering, and with Conventional Powder,” *Sintering Techniques of Materials*, 2015.

[101] J. Els, M. Truscott, J. Van Der Walt, and G. Booysen, “Preliminary findings on an investigation into the three most important process parameters that influence laser sintering of Ti64 and validation of a melt pool simulation model,” *Interim: Interdisciplinary Journal*, vol. 12, pp. 195-209, 2013.

[102] A. Bauerei, T. Scharowsky, and C. Krner, “Defect generation and propagation mechanism during additive manufacturing by selective beam melting,” *Journal of Materials Processing Technology*, vol. 214, pp. 2522-2528, 2014.

[103] B. Liu, R. Wildman, C. Tuck, I. Ashcroft, and R. Hague, “Investigation the effect of particle size distribution on processing parameters optimisation in selective laser melting process,” *in International solid freeform fabrication symposium: an additive manufacturing conference.* University of Texas at Austin, Austin, 2011, pp. 227-238.

[104] H. Zhu, J. Fuh, and L. Lu, “The influence of powder apparent density on the density in direct laser-sintered metallic parts,” *International Journal of Machine Tools and Manufacture*, vol. 47, pp. 294-298, 2007.

[105] X. L. Deng and R. N. Dav, “Dynamic simulation of particle packing influenced by size, aspect ratio and surface energy,” *Granular Matter*, vol. 15, pp. 401-415, 2013.

[106] J. A. Slotwinski, E. J. Garboczi, P. E. Stutzman, C. F. Ferraris, S. S. Watson, and M. A. Peltz, “Characterization of metal powders used for additive manufacturing,” *Journal of Research of the National Institute of Standards and Technology*, vol. 119, p. 460, 2014.

[107] A. Simchi, "Direct laser sintering of metal powders: Mechanism, kinetics and microstructural features," *Materials Science and Engineering: A*, vol. 428, pp. 148-158, 2006.

[108] B. Ferrar, L. Mullen, E. Jones, R. Stamp, and C. Sutcliffe, "Gas flow effects on selective laser melting (SLM) manufacturing performance," *Journal of Materials Processing Technology*, vol. 212, pp. 355-364, 2012.

[109] A. Jillavenkatesa, S. J. Dapkunas, and L.-S. H. Lum, "Particle size characterization," *NIST Special Publication*, 2001.

[110] J.-P. Kruth, X. Wang, T. Laoui, and L. Froyen, "Lasers and materials in selective laser sintering," *Assembly Automation*, vol. 23, pp. 357-371, 2003.

[111] S. Dadbakhsh, L. Hao, and N. Sewell, "Effect of selective laser melting layout on the quality of stainless steel parts," *Rapid Prototyping Journal*, vol. 18, pp. 241-249, 2012.

[112] J.-P. Kruth, M. Badrossamay, E. Yasa, J. Deckers, L. Thijs, and J. Van Humbeeck, "Part and material properties in selective laser melting of metals," *in Proceedings of the 16th International Symposium on Electromachining*, 2010.

[113] A. Wegner and G. Witt, "Correlation of process parameters and part properties in laser sintering using response surface modeling," *Physics Procedia*, vol. 39, pp. 480-490, 2012.

[114] C. Naiju, K. Annamalai, P. Manoj, and K. Ayaz, "Investigation on the Effect of Process Parameters on Hardness of Components Produced by Direct Metal Laser Sintering (DMLS)," *in Advanced Materials Research*, 2012, pp. 1414-1418.

[115] S. Pityana, R. M. Mahamood, E. T. Akinlabi, and M. Shukla, "Gas flow rate and powder flow rate effect on properties of laser metal deposited Ti6Al4V," 2013.

[116] I. Robertson and G. Schaffer, "Some effects of particle size on the sintering of titanium and a master sintering curve model," *Metallurgical and Materials Transactions A*, vol. 40, pp. 1968-1979, 2009.

[117] I. Gibson and D. Shi, "Material properties and fabrication parameters in selective laser sintering process," *Rapid Prototyping Journal*, vol. 3, pp. 129-136, 1997.

[118] A. Flood and F. Liou, “Modeling of Powder Bed ProcessingA Review,” *in International Solid Freeform Fabrication Symposium*, 2015.

[119] R. Ganeriwala and T. I. Zohdi, “Multiphysics modeling and simulation of selective laser sintering manufacturing processes,” *Procedia CIRP*, vol. 14, pp. 299-304, 2014.

[120] T. I. Zohdi, “Rapid simulation of laser processing of discrete particulate materials,” *Archives of Computational Methods in Engineering*, vol. 20, pp. 309-325, 2013.

[121] B. Xiao and Y. Zhang, “Marangoni and buoyancy effects on direct metal laser sintering with a moving laser beam,” Numerical Heat Transfer, Part A: *Applications*, vol. 51, pp. 715-733, 2007.

[122] E. Attar, “Simulation of selective electron beam melting processes,” Dr.-Ing., *University of Erlangen*, Nuremberg, Germany, 2011.

[123] C. Li, C. Fu, Y. Guo, and F. Fang, “A multiscale modeling approach for fast prediction of part distortion in selective laser melting,” *Journal of Materials Processing Technology*, vol. 229, pp. 703-712, 2016.

[124] N. Shen and Y. Chou, “Numerical thermal analysis in electron beam additive manufacturing with preheating effects,” *in Proceedings of the 23rd Solid Freeform Fabrication Symposium*, Austin, TX, 2012, pp. 774-784.

[125] K. Zeng, D. Pal, H. Gong, N. Patil, and B. Stucker, “Comparison of 3DSIM thermal modelling of selective laser melting using new dynamic meshing method to ANSYS,” *Materials Science and Technology*, vol. 31, pp. 945-956, 2015.

[126] W. King, A. Anderson, R. Ferencz, N. Hodge, C. Kamath, and S. Khairallah, “Overview of modelling and simulation of metal powder bed fusion process at Lawrence Livermore National Laboratory,” *Materials Science and Technology*, vol. 31, pp. 957-968, 2015.

[127] X. Ji, J. Z. Zhou, H. F. Guo, and S. Q. Jiang, “3D Finite Element Simulation for the Temperature Field of Direct Metal Laser Sintering Process,” *Journal of Computational and Theoretical Nanoscience*, vol. 5, pp. 1578-1582, 2008.

[128] J. Smith, W. Xiong, J. Cao, and W. K. Liu, “Thermodynamically consistent microstructure prediction of additively manufactured materials,” *Computational Mechanics*, vol. 57, pp. 359-370, 2016.

[129] J. Romano, L. Ladani, and M. Sadowski, "Thermal Modeling of Laser Based Additive Manufacturing Processes within Common Materials," *Procedia Manufacturing*, vol. 1, pp. 238-250, 2015.

[130] L. Costa, R. Vilar, T. Reti, and A. Deus, "Rapid tooling by laser powder deposition: Process simulation using finite element analysis," *Acta Materialia*, vol. 53, pp. 3987-3999, 2005.

[131] K. Dai and L. Shaw, "Thermal and mechanical finite element modeling of laser forming from metal and ceramic powders," *Acta Materialia*, vol. 52, pp. 69-80, 2004.

[132] T. Fang, M. A. Jafari, S. C. Danforth, and A. Safari, "Signature analysis and defect detection in layered manufacturing of ceramic sensors and actuators," *Machine Vision and Applications*, vol. 15, pp. 63-75, 2003.

[133] S. Berumen, F. Bechmann, S. Lindner, J.-P. Kruth, and T. Craeghs, "Quality control of laser-and powder bed-based Additive Manufacturing (AM) technologies," *Physics procedia*, vol. 5, pp. 617-622, 2010.

[134] G. Bi, C. Sun, and A. Gasser, "Study on influential factors for process monitoring and control in laser aided additive manufacturing," *Journal of Materials Processing Technology*, vol. 213, pp. 463-468, 2013.

[135] D. Salehi and M. Brandt, "Melt pool temperature control using LabVIEW in Nd: YAG laser blown powder cladding process," *The International Journal of Advanced Manufacturing Technology*, vol. 29, pp. 273-278, 2006.

[136] J. Mireles, S. Ridwan, P. A. Morton, A. Hinojos, and R. B. Wicker, "Analysis and correction of defects within parts fabricated using powder bed fusion technology," *Surface Topography: Metrology and Properties*, vol. 3, p. 034002, 2015.

[137] J. Mazumder, "Design for Metallic Additive Manufacturing Machine with Capability for Certify as You Build," Procedia CIRP, vol. 36, pp. 187-192, 2015.

[138] Vlasea, M.L., Lane, B., Lopez, F., Mekhontsev, S. and Donmez, A. "Development of powder bed fusion additive manufacturing test bed for enhanced real-time process control." *In Proceedings of the International Solid Freeform Fabrication Symposium*, pp. 527-539, 2015.

[139] M. Mani, B. Lane, A. Donmez, S. Feng, S. Moylan, and R. Fesperman, "Measurement science needs for real-time control of additive manufacturing powder bed fusion processes," *National Institute of Standards and Technology*, Gaithersburg, MD, NIST Interagency/Internal Report (NISTIR), vol. 8036, 2015.

[140] M. R. Boddu, R. G. Landers, S. Musti, S. Agarwal, J. Ruan, and F. W. Liou, "System Integration and Real-Time Control Architecture of a Laser Aided Manufacturing Process," Austin, TX, 2003.

[141] T. Craeghs, S. Clijsters, E. Yasa, and J.-P. Kruth, "Online quality control of selective laser melting," *in Proceedings of the Solid Freeform Fabrication Symposium*, Austin, TX, 2011, pp. 212-226.

[142] D. Hu and R. Kovacevic, "Sensing, modeling and control for laser-based additive manufacturing," *International Journal of Machine Tools and Manufacture*, vol. 43, pp. 51-60, 2003.

[143] I. Llanos, A. Agirre, I. Quintana, and H. Urreta, "Defect elimination on laser milled geometries by means of error detection and correction," *The International Journal of Advanced Manufacturing Technology*, pp. 1-8, 2015.

[144] P. K. Rao, J. P. Liu, D. Roberson, and Z. J. Kong, "Sensor-Based Online Process Fault Detection in Additive Manufacturing," *in ASME 2015 International Manufacturing Science and Engineering Conference*, 2015, pp. V002T04A010-V002T04A010.

[145] T. Purtonen, A. Kalliosaari, and A. Salminen, "Monitoring and adaptive control of laser processes," *Physics Procedia*, vol. 56, pp. 1218-1231, 2014.

[146] R. Landers, "Process control of laser metal deposition manufacturingA simulation study," *in Solid Freeform Fabrication Symposium Proceedings*, 2003, pp. 246-253.

[147] S. K. Everton, M. Hirsch, P. Stravroulakis, R. K. Leach, and A. T. Clare, "Review of in-situ process monitoring and in-situ metrology for metal additive manufacturing," *Materials & Design*, vol. 95, pp. 431-445, 2016.

[148] B. K. Foster, E. W. Reutzel, A. R. Nassar, C. J. Dickman, and B. T. Hall, "A brief survey of sensing for metal-based powder bed fusion additive manufacturing," *in SPIE Sensing Technology+ Applications*, 2015, pp. 94890B-94890B-9.

[149] I. V. Zhirnov, P. A. Podrabinnik, A. A. Okunkova, and A. V. Gusarov, "Laser beam profiling: experimental study of its influence on single-track formation by selective laser melting," *Mechanics & Industry*, vol. 16, p. 709, 2015.

[150] H. Gong, K. Rafi, N. Karthik, T. Starr, and B. Stucker, "Defect morphology in Ti6Al4V parts fabricated by selective laser melting and electron beam melting," *in 24rd Annual International Solid Freeform Fabrication SymposiumAn Additive Manufacturing Conference*, Austin, TX, Aug, 2013, pp. 12-14.

[151] T. Fang, M. A. Jafari, I. Bakhadyrov, A. Safari, S. Danforth, and N. Langrana, “Online defect detection in layered manufacturing using process signature,” *in Systems, Man, and Cybernetics*, 1998. 1998 IEEE International Conference on, 1998, pp. 4373-4378.

[152] N. YU, “Process parameter optimization for direct metal laser sintering (DMLS),” *Ph.D. Thesis, University of Singapore*, 2005.

[153] E. Klar and P. K. Samal, Powder metallurgy stainless steels: processing, microstructures, and properties: *ASM International*, 2007.

[154] T. Craeghs, F. Bechmann, S. Berumen, and J.-P. Kruth, “Feedback control of Layerwise Laser Melting using optical sensors,” *Physics Procedia*, vol. 5, pp. 505-514, 2010.

[155] D. Hu, H. Mei, and R. Kovacevic, “Improving solid freeform fabrication by laser-based additive manufacturing,” *Proceedings of the Institution of Mechanical Engineers, Part B: Journal of Engineering Manufacture*, vol. 216, pp. 1253-1264, 2002.

[156] M. Mahesh, Y. Wong, J. Fuh, and H. Loh, “A six-sigma approach for benchmarking of RP&M processes,” *The International Journal of Advanced Manufacturing Technology*, vol. 31, pp. 374-387, 2006.

[157] R. Paul and S. Anand, “Process energy analysis and optimization in selective laser sintering,” *Journal of Manufacturing Systems*, vol. 31, pp. 429-437, 2012.

[158] M. Khaing, J. Fuh, and L. Lu, “Direct metal laser sintering for rapid tooling: processing and characterisation of EOS parts,” *Journal of Materials Processing Technology*, vol. 113, pp. 269-272, 2001.

[159] C. Dunsky, “Process monitoring in laser additive manufacturing,” *Ind Laser Solut Manuf*, pp. 14-20, 2014.

[160] A. Verma, S. Tyagi, and K. Yang, “Modeling and optimization of direct metal laser sintering process,” *The International Journal of Advanced Manufacturing Technology*, vol. 77, pp. 847-860, 2015.

[161] Y. Chivel and I. Smurov, “On-line temperature monitoring in selective laser sintering/melting,” *Physics Procedia*, vol. 5, pp. 515-521, 2010.

[162] P. Lott, H. Schleifenbaum, W. Meiners, K. Wissenbach, C. Hinke, and J. Bltmann, “Design of an optical system for the in situ process monitoring of selective laser melting (SLM),” *Physics Procedia*, vol. 12, pp. 683-690, 2011.

[163] I. Yadroitsev, P. Krakhmalev, and I. Yadroitsava, "Selective laser melting of Ti6Al4V alloy for biomedical applications: Temperature monitoring and microstructural evolution," *Journal of Alloys and Compounds*, vol. 583, pp. 404-409, 2014.

[164] R. B. Dinwiddie, R. R. Dehoff, P. D. Lloyd, L. E. Lowe, and J. B. Ulrich, "Thermographic in-situ process monitoring of the electron-beam melting technology used in additive manufacturing," *in SPIE Defense, Security, and Sensing*, 2013, pp. 87050K-87050K-9.

[165] S. Price, J. Lydon, K. Cooper, and K. Chou, "Experimental temperature analysis of powder-based electron beam additive manufacturing," *in Proceedings of the Solid Freeform Fabrication Symposium*, 2013, pp. 162-173.

[166] E. Rodriguez, F. Medina, D. Espalin, C. Terrazas, D. Muse, C. Henry, et al., "Integration of a thermal imaging feedback control system in electron beam melting," *in Proceedings of the Solid Freeform Fabrication Symposium*, 2012.

[167] A. Wegner and G. Witt, "Process monitoring in laser sintering using thermal imaging," *in SFF Symposium*, Austin, Texas, USA, 2011, pp. 8-10.

[168] H. Krauss, C. Eschey, and M. Zaeh, "Thermography for monitoring the selective laser melting process," *in Proceedings of the Solid Freeform Fabrication Symposium*, 2012.

[169] S. Santospirito, K. Syk, B. Luo, R. opatka, O. Gilmour, and J. Rudlin, "Detection of defects in laser powder deposition (LPD) components by pulsed laser transient thermography," *in SPIE Defense, Security, and Sensing*, 2013, pp. 87050X-87050X-11.

[170] S. Price, K. Cooper, and K. Chou, "Evaluations of temperature measurements by near-infrared thermography in powder-based electron-beam additive manufacturing," *in Proceedings of the Solid Freeform Fabrication Symposium*, 2012, pp. 761-773.

[171] S. Kerwien, S. Collings, F. Liou, and M. Bytnar, "Measurement Science Roadmap for Metal-based Additive Manufacturing," *ed: NIST*, 2013.

[172] D. Seltzer, X. Wang, A. Nassar, J.L. Schiano, and E.W. Reutzel, "System identification and feedback control for directed-energy, metal-based additive manufacturing." *In Solid Freeform Fabrication Proceedings*, 2014, pp. 592-601.

[173] F. Ellyin, Fatigue damage, crack growth and life prediction: *Springer Science & Business Media*, 2012.

[174] P. Aggarangsi, J. L. Beuth, and M. Griffith, "Melt pool size and stress control for laser-based deposition near a free edge," *in Solid Freeform Fabrication Proceedings*, 2003, pp. 196-207.

[175] P. Aggarangsi, J. L. Beuth, and D. D. Gill, "Transient changes in melt pool size in laser additive manufacturing processes," *in Solid Freeform Fabrication Proceedings*, University of Texas, Solid Freeform Fabrication Symposium, Austin, TX, Aug, 2004, pp. 2-4.

[176] A. Birnbaum, P. Aggarangsi, and J. Beuth, "Process scaling and transient melt pool size control in laser-based additive manufacturing processes," *in Solid Freeform Fabrication Proceedings*, 2003, pp. 328-339.

[177] M. R. Boddu, R. G. Landers, and F. W. Liou, "Control of laser cladding for rapid prototypingA review," *in Proceedings of the Solid Freeform Fabrication Symposium*, 2001, pp. 6-8.

[178] G. Bi, A. Gasser, K. Wissenbach, A. Drenker, and R. Poprawe, "Characterization of the process control for the direct laser metallic powder deposition," *Surface and Coatings Technology*, vol. 201, pp. 2676-2683, 2006.

[179] H. Gong, H. Gu, K. Zeng, J. Dilip, D. Pal, B. Stucker, et al., "Melt pool characterization for selective laser melting of Ti-6Al-4V pre-alloyed powder," *in Solid Freeform Fabrication Proceedings*, 2014.

[180] T. Scharowsky, F. Osmanlic, R. Singer, and C. Krner, "Melt pool dynamics during selective electron beam melting," *Applied Physics A*, vol. 114, pp. 1303-1307, 2014.

[181] B. Cheng and K. Chou, "Melt pool geometry simulations for powder-based electron beam additive manufacturing," *in 24th Annual International Solid Freeform Fabrication Symposium-An Additive Manufacturing Conference*, TX, USA, 2013.

[182] J. Gockel, J. Beuth, and K. Taminger, "Integrated control of solidification microstructure and melt pool dimensions in electron beam wire feed additive manufacturing of Ti-6Al-4V," *Additive Manufacturing*, vol. 1, pp. 119-126, 2014.

[183] D. Cormier, O. Harrysson, and H. West, "Characterization of H13 steel produced via electron beam melting," *Rapid Prototyping Journal*, vol. 10, pp. 35-41, 2004.

[184] G. Marshall, W. Young II, N. Shamsaei, J. Craig, T. Wakeman, and S. Thompson, "Dual Thermographic Monitoring of Ti-6Al-4V Cylinders During Direct Laser Deposition," *in Proc. Intl. Solid Freeform Fabrication Symposium*, 2015, pp. 259-272.

[185] H. Carslaw and J. Jaeger, Conduction of heat in solids: *Oxford Science Publications*: Oxford, England, 1959.

[186] C. Chan, J. Mazumder, and M. Chen, "A two-dimensional transient model for convection in laser melted pool," *Metallurgical Transactions A*, vol. 15, pp. 2175-2184, 1984.

[187] T. Eagar and N. Tsai, "Temperature fields produced by traveling distributed heat sources," *Welding Journal*, vol. 62, pp. 346-355, 1983.

[188] B. Mueller, "Additive manufacturing technologiesRapid prototyping to direct digital manufacturing," *Assembly Automation*, vol. 32, 2012.

[189] F. Herzog, F. Bechmann, S. Berumen, J. P. Kruth, and T. Craeghs, "Method for producing a three-dimensional component," *ed: Google Patents*, 2013.

[190] A. Fathi, A. Khajepour, M. Durali, and E. Toyserkani, "Geometry control of the deposited layer in a nonplanar laser cladding process using a variable structure controller," *Journal of Manufacturing Science and Engineering*, vol. 130, p. 031003, 2008.

[191] M. Zeinali and A. Khajepour, "Height control in laser cladding using adaptive sliding mode technique: theory and experiment," *Journal of Manufacturing Science and Engineering*, vol. 132, p. 041016, 2010.

[192] T. A. Davis and Y. C. Shin, "Vision-based clad height measurement," *Machine Vision and Applications*, vol. 22, pp. 129-136, 2011.

[193] J. Schwerdtfeger, R. F. Singer, and C. Krner, "In situ flaw detection by IR-imaging during electron beam melting," *Rapid Prototyping Journal*, vol. 18, pp. 259-263, 2012.

[194] J. Mireles, C. Terrazas, F. Medina, R. Wicker, and E. Paso, "Automatic feedback control in electron beam melting using infrared thermography," *in Proceedings of the Solid Freeform Fabrication Symposium*, 2013.

[195] FLIR, The Ultimate Infrared Handbook for R & D Professionals: A Resource Guide for Using Infrared in the Research and Development Industry, 2013, Retrieved from *http://www. globalspec. com/FeaturedProducts/Detail/FLIR/The Ultimate Infrared Handbook for RD/112511*

[196] N. K. Spinnie, "Large scale fused deposition modeling: the effect of process parameters on bead geometry," *M.Sc. Thesis, Baylor University*, 2016.

[197] S. Clijsters, T. Craeghs, S. Buls, K. Kempen, and J.-P. Kruth, "In situ quality control of the selective laser melting process using a high-speed, real-time melt pool monitoring system," The International *Journal of Advanced Manufacturing Technology*, vol. 75, pp. 1089-1101, 2014.

[198] E. M. Samuel Attoye, Hazim El-Mounayri, "Correlation between process parameters and mechanical properties in parts printed by the Fused Deposition Modeling process," *Mechanics of Additive and Advanced Manufacturing*, vol. 10, 2018.

[199] W. Yang and W. Blasiak, "CFD as applied to high temperature air combustion in industries furnaces," *IRFR Combustion Journal*, 2006.

[200] F. Trevisan, F. Calignano, M. Lorusso, J. Pakkanen, A. Aversa, E. P. Ambrosio, et al., "On the selective laser melting (SLM) of the AlSi10Mg alloy: process, microstructure, and mechanical properties," Materials, vol. 10, p. 76, 2017.

[201] EOS, Technical description EOSINT M280, 2010, Retrieved from *https://www.eos.info/*

[202] A. Hussein, L. Hao, C. Yan, and R. Everson, "Finite element simulation of the temperature and stress fields in single layers built without-support in selective laser melting," *Materials & Design (1980-2015)*, vol. 52, pp. 638-647, 2013.

[203] C. Fu and Y. Guo, "3-Dimensional finite element modeling of selective laser melting Ti-6Al-4V alloy," *in 25th Annual International Solid Freeform Fabrication Symposium*, 2014.

[204] Engineers Edge LLC., Heat Transfer directory, 2018, Retrieved from *https://www.engineersedge.com*

[205] Y. Ning, J. Fuh, Y. Wong, and H. Loh, "An intelligent parameter selection system for the direct metal laser sintering process," *International Journal of Production Research*, vol. 42, pp. 183-199, 2004.

[206] J. Mireles, C. Terrazas, S. M. Gaytan, D. A. Roberson, and R. B. Wicker, "Closed-loop automatic feedback control in electron beam melting," *The International Journal of Advanced Manufacturing Technology*, vol. 78, pp. 1193-1199, 2015.

[207] J. F. Briceno, H. El-Mounayri, and S. Mukhopadhyay, "Selecting an artificial neural network for efficient modeling and accurate simulation of the milling process," *International Journal of Machine Tools and Manufacture*, vol. 42, pp. 663-674, 2002.

[208] D. E. C. A. Singh, N.J. Blundell, G.J. Gibbons, D.K. Pratihar, "Modelling of Direct Metal Laser Sintering of EOS DM20 Bronze Using Neural Networks and Genetic Algorithms," *in 37th MATADOR Conference*, 2012.

[209] H. El-Mounayri, J. F. Briceno, and M. Gadallah, "A new artificial neural network approach to modeling ball-end milling," *The International Journal of Advanced Manufacturing Technology*, vol. 47, pp. 527-534, 2010.

[210] X. Gao, D. You, and S. Katayama, "Seam tracking monitoring based on adaptive Kalman filter embedded Elman neural network during high-power fiber laser welding," *IEEE Transactions on Industrial Electronics*, vol. 59, pp. 4315-4325, 2012.

[211] J. L. Elman, "Finding structure in time," *Cognitive science*, vol. 14, pp. 179-211, 1990.

[212] F.-J. Lin, Y.-C. Hung, and S.-Y. Chen, "FPGA-based computed force control system using Elman neural network for linear ultrasonic motor," *IEEE Transactions on Industrial Electronics*, vol. 56, pp. 1238-1253, 2009.

[213] T. Sawaragi and T. Kudoh, "Self-reflective segmentation of human bodily motions using recurrent neural networks," *IEEE Transactions on Industrial Electronics*, vol. 50, pp. 903-911, 2003.

[214] C.-H. Lu and C.-C. Tsai, "Adaptive predictive control with recurrent neural network for industrial processes: An application to temperature control of a variable-frequency oil-cooling machine," *IEEE Transactions on Industrial Electronics*, vol. 55, pp. 1366-1375, 2008.

[215] C.-H. Lu, "Design and application of stable predictive controller using recurrent wavelet neural networks," *IEEE Trans. Industrial Electronics*, vol. 56, pp. 3733-3742, 2009.

[216] A. Barron, "Neural net approximation, in"Yale Workshop on Adaptive and Learning Systems," *Yale University*, 1992.

[217] E. Yasa, F. Demir, G. Akbulut, N. Cizioglu, and S. Pilatin, “Benchmarking of different powder-bed metal fusion processes for machine selection in additive manufacturing,” *in Proceedings of International Solid Freeform Fabrication Symposium*, 2014, pp. 390-403.

[218] J.-P. Kruth, B. Vandenbroucke, v. J. Vaerenbergh, and P. Mercelis, “Benchmarking of different SLS/SLM processes as rapid manufacturing techniques,” 2005.